

Uniwersytet Jagielloński
Instytut Fizyki im. Mariana Smoluchowskiego



**Badanie czynnika modyfikacji jądrowej w
zderzeniach Au + Au przy $\sqrt{s_{NN}} = 200\text{GeV}$**

mgr Radosław Karabowicz

Praca doktorska złożona na
Wydziale Fizyki, Astronomii i Informatyki Stosowanej
Uniwersytetu Jagiellońskiego

Promotor:
Prof. dr hab. Zbigniew Majka

Kraków, sierpień 2006

Jagiellonian University
Marian Smoluchowski Institute of Physics



**Study of Nuclear Modification Factors in
Au + Au collisions at $\sqrt{s_{NN}} = 200\text{GeV}$**

Radosław Karabowicz M.Sc.

Dissertation presented to the
Faculty of Physics, Astronomy and Applied Computer Science
of the Jagiellonian University
for the degree of Doctor of Physics

Dissertation supervisor:
Professor Zbigniew Majka

Kraków, August 2006

Acknowledgements

This work would not be possible without work of many people. I am particularly grateful to my supervisor Prof. Zbigniew Majka many helpful advices and discussions during these several years of my work in the Hot Matter Physics Division. Special thanks goes to Pawel Staszal, whose experience, knowledge and warmth were a great support for me in these demanding times. I would also like to thank all the members of the Division for their helpful hand, especially Jerzy Cibor, Roman Płaneta, Tomasz Kozik, Marcin Misiaszek, Natalia Katryńska and Elżbieta Kotula.

I am grateful to the Providence for allowing me to gather experience and knowledge in the BRAHMS Collaboration. I sincerely believe this small group of people (see Appendix A for the full list) made one of the nicest environments to work in the high energy heavy ion physics. It was pleasure to collaborate with people like Flemming Videbæk, Chellis Chasman, Ramiro Debbe, JH Lee, Michael Murray, Steve Sanders, Ian Bearden, Peter Christiansen, Christian Holm, Catalin Ristea, Dieter Roehrich, Yang Hongyan, Bjørn H. Samset, Ionut Arsene and many others.

This work was supported by the Polish State Committee for Scientific Research, grant number 0383/P03/2005/29.

Finally, I express the warmest thanks to my parents and girlfriend for their love, support and patience.

Dziękuję Wam, Rodzice!

Radosław Karabowicz, Kraków, August 2006

Contents

1	Introduction	1
1.1	Onset of nuclear physics	1
1.2	Going smaller - description of nucleus	2
1.3	Accelerator era begins	4
1.4	Black clouds - new particles	5
1.5	Quarks and QCD	6
1.6	QGP	7
1.7	Future	9
1.8	Implications. Far away in space and time	10
1.9	Outline of the work	11
2	RHIC and BRAHMS	12
2.1	Introduction	12
2.2	RHIC	12
2.3	Experiments	13
2.3.1	STAR	13
2.3.2	PHENIX	14
2.3.3	PHOBOS	15
2.4	BRAHMS	15
2.5	Relativistic heavy ion collision	20
2.5.1	Introduction	20
2.5.2	Initial state	21
2.5.3	Collision	24
2.6	Review of the BRAHMS experimental results	24
2.6.1	Energy density	25
2.6.2	Net-proton distribution	26
2.6.3	Chemical freeze-out	27
2.6.4	Thermal freeze-out	30

2.6.5	Elliptic flow	33
2.6.6	Baryon enhancement	35
2.6.7	Jet suppression	36
3	Nuclear modification factor	41
3.1	Definition	41
3.2	Nuclear modification factor at SPS	43
3.3	Nuclear modification factor at RHIC	43
3.3.1	Energy dependence	44
3.3.2	Fireball size dependence	45
3.3.3	Rapidity dependence	47
3.3.4	Identified particles	47
3.3.5	d + Au collisions	49
3.4	Theoretical interpretation	51
3.4.1	Multiple parton scattering	51
3.4.2	Twist expansion	53
3.4.3	Surface emission	54
3.4.4	Hydrodynamic model	54
3.4.5	Recombination	54
3.4.6	CGC	55
3.4.7	Summary	55
4	Data analysis chain	56
4.1	Introduction	56
4.2	Event characteristics	56
4.2.1	Vertex position	56
4.2.2	Centrality determination	57
4.3	Particle Tracking	57
4.3.1	Local tracking	58
4.3.2	Global tracking	62
4.4	Particle identification	64
4.5	Corrections	67

4.5.1	Acceptance	67
4.5.2	Efficiency	68
4.5.3	In-flight decay, scattering and absorption	70
4.6	Triggers and yield normalization	71
4.7	Construction of particle spectra	75
4.8	Glauber Model	75
5	Results	80
5.1	Introduction	80
5.2	Identified particle spectra	81
5.3	Nuclear modification factor	84
5.3.1	Numbers of binary collisions and participants	84
5.3.2	R_{AA} for unidentified hadrons	84
5.3.3	R_{AA} for identified hadrons	87
5.3.4	Centrality Dependence	88
5.3.5	Higher rapidities	93
5.4	Discussion of the results	93
5.4.1	Slope influence	93
5.4.2	CGC effect	93
5.4.3	Scaling with energy density	95
6	Conclusions	97
A	The BRAHMS Collaboration	99
	References	101

1 Introduction

1.1. Onset of nuclear physics

Year 1897 marks an opening of a new era in physics. Up to that date physicists widely believed that atoms are the basic elements forming matter that could not be broken or divided. This idea, developed in ancient India [1] and Greece [2] more than two thousand years ago, shattered when, in 1897, sir Joseph John Thomson [3] discovered an electron¹ and proved it was emitted from atom. The following years brought discoveries of radiation emitted from atom, and various types were named using first Greek letters: alpha², beta³ and gamma⁴. At that time the Thomson's model [4] of atom was in use. It assumed that the negatively charged electrons are randomly located in a large positively charged ball just like plums in a pudding, hence afterwards it was called a "plum pudding model".

The model was generally accepted until 1911, when Ernest Rutherford [5] carried out his famous "gold foil" experiment, which is worthwhile to dwell upon here, as it for the first time showed the existence of the heavy nucleus inside atom. Rutherford with his students Hans Geiger and Ernest Marsden bombarded a thin gold foil with alpha particles. Existing atom theory predicted the alphas to leave the foil having only slightly changed momenta due to interaction with atoms. However they observed a few particles scattered at large angles - sometimes the outgoing alphas were moving back towards the source itself. This contradicted their expectations and abolished the atom model of Thomson. Rutherford created his own model, where a small, heavy, positively charged nucleus occupies the center of atom, while a cloud of negatively charged electrons surrounds it. This idea also included first

¹electron - Greek for amber. Amber has been used by ancient Greeks to create static electricity, and thus the first discovered electrically charged particle was named electron.

²a nucleus of helium ${}^4\text{He}$.

³electron and its positively charged antiparticle.

⁴electromagnetic radiation.

explanation of the structure of nucleus. Rutherford calculated that the nucleus' size is of the order of 10^{-12} cm, which was four orders of magnitude smaller than the size of atom. The simple calculations basing on available data lead to estimation of the electrical charge of the gold nuclei to be +100e. Knowing furthermore the atomic mass of various elements, and the fact that alpha particles are simply helium atoms (stripped of electrons) he concluded that the calculations agree if *the atom of gold consisted of 49 atoms of helium, each carrying a charge $2e$* [5]. The idea of heavy nucleus surrounded by electrons was heavily attacked by adherents of the Thompson's idea criticizing mainly the instability of such a system. Two years later a student of Rutherford, Niels Bohr [6], proposed quantum-mechanical description of atom where electrons can only emit finite portions of energy. He used the idea of finite quanta of light proposed by Max Planck [7] in 1900 and applied it in the description of atom as proposed by Albert Einstein [8].

Bohr's model of atom eventually lead Heisenberg [9] and Schrödinger [10] in mid-20s' to development of a completely novel and unintuitive mechanics, called quantum mechanics. In the following years the new theory proved correct in solving many physical problems at small scale.

1.2. Going smaller - description of nucleus

Simultaneously with the effort to understand the physics of atom, scientists delved into the composition of the nucleus. Protons were discovered in 1918 by Rutherford [11] who identified positive particles emitted when bombarding nitrogen with alpha particles. In the paper he describes nitrogen nuclei (^{14}N) as consisting of 3 alpha particles and 2 hydrogen nuclei.

In 1920 Rutherford [12], analyzed the structure of the nucleus and concluded that the mass of the nuclei comes mainly from the heavy hydrogen nuclei, and, to account for charge, there is admixture of electrons bound inside the nuclei - so that in case of ^{14}N there are 14 protons and 7 electrons in its nucleus. The total number of electrons in atoms (the ones inside the nucleus and the ones orbiting the heavy core) is exactly equal to the number of protons to make the atom electrically neutral. In the same paper he ponders on a concept of neutral particle having mass close to

proton mass, being rather a bound state of proton and electron.

Almost ten years later Franco Rasetti [13] measured the spin of the nitrogen nucleus ^{14}N and it became apparent that neutral particle inside the nuclei have to exist. It was known that the electrons have spin $1/2$, so whatever spin protons would have the overall spin of ^{14}N should be $1/2$. Rasetti however shown that the spin of ^{14}N is 1. In 1930 Wolfgang Pauli proposed in his letter titled: "Liebe Radioaktive Damen und Herren" [14] possibility of existence of very light and electrically neutral particle, which he called neutron, that would explain the problems with nucleus spin seen by Rasetti.

In 1930 Bothe and Becker while bombarding beryllium with alpha particles observed neutral radiation with a large distance of penetration. The observation was later-on confirmed by Curie and Joliot (1931) and was classified as high-energy gamma radiation. In 1932 James Chadwick J. Chadwick, [15] however suggested that the observed particles are the neutral particles proposed by Rutherford [12] and called them neutrons.

Meanwhile physicists struggled with the beta decay, which has been a puzzle since its discovery. Observation of other decays (alpha and gamma) showed that the emitted particles had well defined energy, while the energy of electrons from beta decay varied over a considerable range. It had been even proposed by Bohr in 1924 that the process breaks the energy conservation principle. In his letter from 1930 Pauli [14] suggested that the neutral particle could be emitted in beta decay, which would explain the continuous spectra of electrons' energies. Later similar hypothesis was presented by Enrico Fermi, who named the particle a neutrino due to very small mass of the particle.

Explanation of beta decay process and later discoveries lead physicists to introduction of a new type of interaction called weak force. It should be mentioned here that although the energy conservation was saved other conservation rules are actually broken in weak processes.

At this point the mystery of atom seemed to be solved. Physicists now believed it consists of a heavy core called nucleus that contained protons and neutrons surrounded by electrons filling strict orbits. The nucleus could emit several kind of radiation: protons, neutrons, electrons (when neutron decays to proton it emits elec-

tron and neutrino which was yet to discover), alpha particles and gamma rays. Only the nature of forces bounding protons and neutrons inside the nucleus was to be found, but after the Hideki Yukawa's [16] concept of strong forces was introduced in 1935 even this problem was solved.

1.3. Accelerator era begins

Meanwhile this simple model had been impaired by various observations. In as early as 1931 Paul Adrien Maurice Dirac [17] was considering existence of complementary states of electrons and protons and called them anti-electron and anti-proton. These anti-particles were to have same mass and spin as particles, but opposite charge. Only two years later Carl D. Anderson [18] reported observation of anti-electrons (which were called by him positrons) in the cosmic radiation. Few years later, again in cosmic radiation another particle was found by Anderson [19] having a mass somewhere between electron and proton, and thus called *mesotron*. Initially it was believed that the particle is the one predicted by Yukawa and is the carrier of the strong force. The studies of the particle that followed showed that the particles do not participate in strong interactions and thus cannot be associated with particles proposed by Yukawa. They have been therefore named muons (from Greek letter μ).

Most of the nuclear experiments conducted until mid 30ths used natural sources of radiation like radioactive elements or cosmic radiations. The initial conditions in such experiments were unsatisfactory - the energy of radiation from natural sources is usually small, and cosmic radiation was not easily observed due to protective influence of atmosphere. The importance of knowledge of binding forces keeping the nuclei together lead to designing and construction of particle accelerators. First designs and prototypes appeared simultaneously at few universities around 1929:

1. John Douglas Cockcroft and Ernest Thomas Sinton Walton from Rutherford's Lab in Cambridge used voltage multipliers to convert low-voltage AC or DC into higher DC voltage and created a Cockcroft-Walton generator (from 280 kV in 1928 up to 0.75 MV in 1932).
2. Robert J. Van De Graaff [20] in Princeton used an idea of moving belt carry-

ing electric charges to obtain high voltage and built Van De Graaff generator (80kV in 1929, 7MV in 1933).

3. Wideröe [21] designs and builds a prototype of a multi-gap drift linear accelerator in 1929; later the idea was used by David Sloan [22] in Ernest Lawrence group at UC-Berkeley to built LINAC capable of accelerating particles to 1.25 MeV in 1931.
4. In 1930 Ernest O. Lawrence [23] at UC-Berkeley invents a cyclotron, where magnetic and electric fields are used in combination to accelerate and bend particles, first prototype accelerates up to 80keV in 1931 and reaches 16MeV in 1936.

Second World War significantly slowed down progress on fundamental nuclear science gathering most of the efforts in the famous Manhattan Project.

1.4. Black clouds - new particles

The last great discovery using cosmic rays was that of Cecill Frank Powell [24] and his collaborators, who measured and identified charged pions, mesons predicted by Yukawa and searched for more than 20 years. Next year charged pions have been observed in processes induced by particles accelerated in cyclotron in Berkeley by Lattes [25]. The following year at the same facility K^+ particles were observed by their decay. 1953 brings another particles (lambda and other kaons), in 1956 mysterious neutrino was finally detected, and shortly a whole “particle zoo” of heavier particles followed.

Soon it became urgent to find some underlying explanations of the ever-growing immensity of observed particles. In 1961 Murray Gell-Mann together with Kazuhiko Nishijima [26] (and independently Yuval Ne’eman [27]) introduced a classification of hadrons basing on their charge and strangeness (a property of particles introduced by Gell-Mann to explain strange decays of kaons [28]) which he named the eightfold way, due to particles’ arrangements in octets. Analyzing available experimental data Gell-Mann realized that one of the pseudo-scalar particles that exists in his model has not yet been discovered. In his paper [29] he predicted existence of

an isotopic singlet particle with spin = $3/2$, positive parity, mass of roughly 1,680 MeV, negative charge, baryon number +1, strangeness = -3, and stable to strong decay. The particle was discovered in late 1963 in the Brookhaven National Laboratory by Barnes [30].

1.5. Quarks and QCD

In 1964 Murray Gell-Mann [31] and Zweig [32] independently introduced to the world the idea of quarks. Initially only mathematical concept (SU(3)) proved successful in explaining the systematics of observed hadrons and predicting new particles. Original concept consisted of various combinations of the three quarks, but soon Bjorken and Glashow [33] added fourth quark. To explain existence of Δ^{++} particle, which consists of three up quarks a new degree of freedom (color) in SU(3) gauge theory was introduced by Greenberg [34] and independently by Han and Nambu [35]. Eventually the idea evolved into a complex theory with 6 elementary quarks and a group of 8 gluons [35] responsible for interactions. The table of known elementary particles presented in Table 1.1 contains also the group of 6 leptons and 4 bosons responsible for the electroweak interactions.

In spite of many efforts quarks has not been seen separately, outside of hadrons which they form. It had been suggested that they are rather mathematical objects. In 1969, thanks to theoretical effort by Feynman [36] and Bjorken [37] the quark-like structure of proton has been confirmed in experiments on deep inelastic scattering (DIS) of electrons on proton performed by Friedman, Kendall and Taylor [38].

Meanwhile, a theory of strong interactions, called Quantum Chromo Dynamics (QCD), has been developing basing on a gauge field theory introduced by Yang and Mills [39]. The work was finalized soon after the discovery of asymptotic freedom by Gross and Wilczek [40] and Politzer [41]. They propose that quarks move almost freely inside the hadrons, because at small distances the QCD interactions become weak. One could imagine strong force is something like a spring that binds the partons. As they are close the spring is loose and the particles are free. If, however, the particles are pulled apart, the spring tightens and the force increases with distance. As any analogy, it must differ at some point, and it differs in the moment when the

	1 st	2 nd	3 rd
quarks	u	c	t
	d	s	b
leptons	ν_e	ν_μ	ν_τ
	e	μ	τ

interaction	bosons
strong	8 gluons
electro-magnetic	photon (γ)
weak	W^+, W^-, Z^0

Table 1.1

Elementary particles. Left table shows constituents of matter (fermions) grouped into three generations. Right table shows particles responsible for interactions (bosons).

spring breaks. As the two particles are further pulled apart they interact stronger and stronger, the energy used for pulling them apart concentrate in a strong color field flux between them until finally, when there is enough energy, the color field breaks. The difference is that the accumulated energy is used for creation of quark-antiquark pair. Thus never any free quark can be observed. Each time a quark have enough energy to leave the hadron, the $q\bar{q}$ pair is created, and again bound quarks object is created. The question arises why the strong bounds do not exists between all the particles in the world, since the distances are even bigger. The answer is that the observed particles are color neutral. All baryons are bound states of three quarks/antiquarks, each having different color/anticolor charge, which, for convenience, are called red, green and blue. Mesons consist of one quark of some color and one antiquark with a respective anticolor. This effect of strong interactions is usually referred to as “color confinement” as no color particles are observed separately.

1.6. QGP

In 1975 Collins and Perry [42] proposed the existence of a new phase of nuclear matter, which was later called the Quark-Gluon Plasma (QGP). Just as quarks are bound inside the hadrons it is natural to conceive an idea of a dense state of a bulk of

matter, larger than a hadron, where the density of quarks and gluons is large enough to treat the constituents as quasi-free objects.

It is common to use the phase-space diagram when talking about different states of matter. Such diagram for nuclear matter is seen in Figure 1.1, where different states are shown as a function of baryon density and temperature. The chart is in general unknown, it's all *terra incognita*, except of a small point - the nuclear matter in its ground state, as it exists in the atomic nuclei. Nuclear physics can probe the diagram by nuclear collisions, in which matter is heated and squeezed. After a short time of few fm/c it comes back to its normal state by emission of energetic particles. Trajectories of nuclear matter evolutions in this simple picture are shown in Figure 1.1 for nucleus-nucleus collisions at different energies.

From the QCD calculations the transition of normal nuclear matter into the QGP phase is expected at high temperatures and/or high densities. To achieve these condition, and more important to be able to detect the transition, dedicated facilities and experiments have been constructed.

Alternate Gradient Synchrotron (AGS) at BNL was the first accelerator where scientists hoped to see the quark-gluon plasma. The facility could accelerate heavy ions up to gold (Au) to energy as high as $10.7 A \cdot GeV$. Collisions took place at stationary targets with center-of-mass energy $\sqrt{s_{NN}} \approx 4 GeV$ ⁵. Modern calculations show however that QGP was not created in experiments at that small energy.

Super Proton Synchrotron (SPS) at CERN was accelerating ions of lead (Pb) up to energy of $158 A \cdot GeV$ which corresponds to $\sqrt{s_{NN}} \approx 17.3 GeV$. Recent results obtained by the WA98 experiment [43], although inconclusive, might indicate transition to QGP in most central events at this energy. Theoretical predictions opt for the transition, although it is pointed out that the duration of the phase is not long enough to be experimentally detectable.

Current efforts and results of the Relativistic Heavy Ion Collider (RHIC) at the Brookhaven National Laboratory (BNL) suggesting exploration of the QGP phase are presented in Chapter 2 of this work.

⁵ $\sqrt{s_{NN}}$ is the center-of-mass energy per nucleon pair, $\sqrt{s_{NN}} = 2E_{CM}$, where E_{CM} is the nucleon energy in center-of-mass frame. In case of experiments at stationary targets $E_{CM} = \sqrt{m_N(E_{lab} + m_N)}/2$, where E_{lab} is the energy on projectile nucleon and m_N is mass of the nucleon.

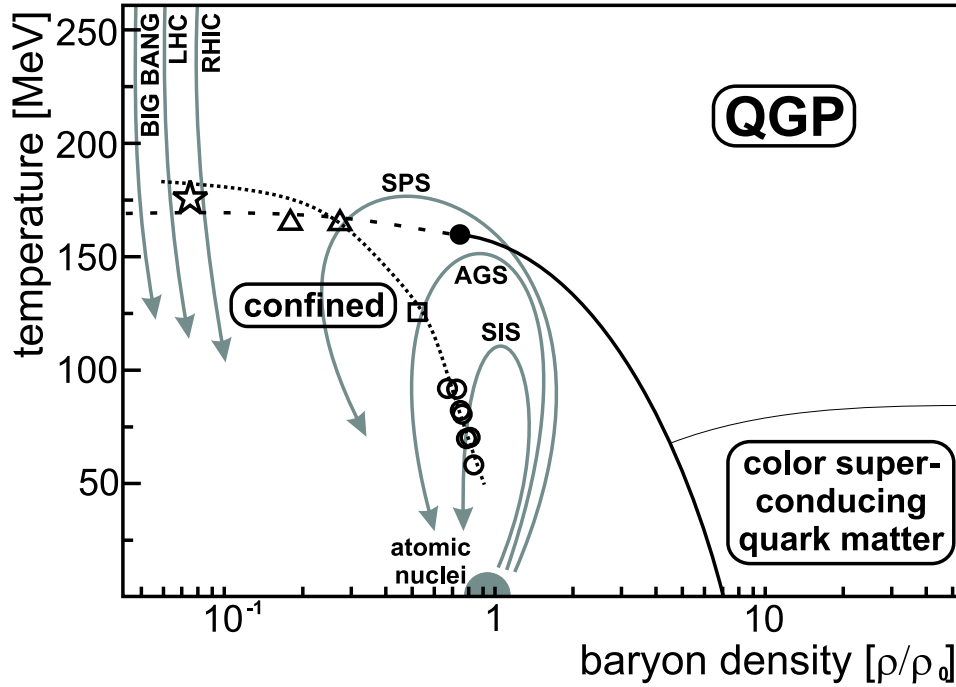


Figure 1.1. Phase diagram of the nuclear matter. Gray lines show trajectories of nuclear matter evolutions in collisions at various energies (SIS, AGS, SPS, RHIC, LHC) and the one from the Big Bang. Expected transition between hadronic matter and QGP state is presented as solid (1st order phase transition) and dashed (higher order phase transition). The full circle shows critical point. Dotted line represents the freeze-out conditions, deduced from experiments at SIS (circles), AGS (square), SPS (triangles) and RHIC (star).

1.7. Future

It is proper to mention in this place what are the plans of the high energy physics community. Needless to say, the most interests and efforts are put into going to higher energies. A new accelerator in CERN at LHC could be called a lighthouse that will shed light into the phase space diagram with its top energy of $\sqrt{s_{NN}} = 5.5$ TeV in Pb + Pb collisions. ALICE [44] is the major heavy ion experiment at LHC, but another experiments ATLAS [45] and CMS [46], which focus mainly on

elementary $p + p$ collisions are also planning to measure heavy ion reactions.

There is also a strong group expecting great experimental results of utmost importance in lower energy regime. RHIC (and also LHC) probe the phase-space diagram in the limit of high temperatures and low baryonic density. Lattice QCD (for recent developments see Ref. [47] and references within) calculations triggered by the RHIC experimental results show that the transition from QGP to the hadronic matter is a second order phase transition. Transitions at lower temperatures and larger densities are expected to be first order phase transitions, and the point when the character of transition changes is called a critical point (compare Figure 1.1). The new experiments at lower energies of about 30 – 40 GeV focus on searching of this critical point. They would also like to study the QGP or hadronic matter in the higher density regime. Those measurements which are major goals for the future CBM experiment [48] at GSI, that will begin operation in 2012 collect growing interest of physicist. Currently RHIC Management is considering possibility to run collider at smaller energies, or even to make experiments at stationary targets, while NA49 [49] Collaboration at SPS is planning to take larger statistics data at various energies and system sizes.

1.8. Implications. Far away in space and time

One of the main interests for ordinary people when listening about high energy heavy ion physics is “why?”, “what for?”. In this section in few sentences I would like to answer this question.

The most important answer is to study nuclear matter and strong interactions. Little is actually known about the smallest parts of matter (quarks and gluons) although they are the main constituents of the matter that we observe. Let me name only the most controversial problem - physics still cannot give definite answer to the question of mass generation. QCD is unable to answer most of the questions as there are no good computational methods in the energy/density region of the ground state of the nuclear matter. Study of high energy heavy ion collisions will help to constrain the available models.

The research can also bring a lot of impact on the theory of the Big Bang, the most

popular theory explaining the beginning of the Universe. The lack of thorough understanding of the strong forces makes scientists walking in fog when talking about the earliest phases of the Universe. Study of strong interactions makes an important, though not the most important, step towards understanding the various phenomena of the Big Bang, especially the observed lack of antimatter in the Universe.

The QGP, that is being currently studied at RHIC, may also exist in the innermost cores of the neutron stars. It has been proposed that the neutron stars may be something more complicated than objects made of neutrons. The sheer gravitational force would cause the neutrons lose their integrity and become a medium of basically free quarks - the quark-gluon plasma. Studying of the unknown phase can thus be helpful in creating theory of the neutron stars.

1.9. Outline of the work

This work will present the data obtained by the BRAHMS experiment in Au + Au and p + p collisions at $\sqrt{s_{NN}} = 200 \text{ GeV}$ at the Relativistic Heavy Ion Collider (RHIC). Obtained data will be used to construct the nuclear modification factors to study the properties of the nuclear matter produced in the heavy ion collision. In the second chapter the collider and experiment will be introduced, and the most important results summarizing several years of data taking presented. Third chapter will bring a definition of nuclear modification factor, results from SPS and RHIC, and major theoretical developments on interpretation of the factor. Analysis chain will be briefly introduced in the fourth chapter. Results of analysis on rapidity evolution of the nuclear modification factor will be presented in chapter five together with possible interpretations. Last, sixth chapter will summarize the work.

2 RHIC and BRAHMS

2.1. Introduction

Relativistic Heavy Ion Collider in BNL began operation in 2000 after 15 years of design and construction works. Heavy ions collisions at center-of-mass energy of 200 GeV are currently being investigated by a multitude of physicists around the globe. The observation of QGP was announced by all four experiments and was announced “The Top Physics Stories for 2005” by American Institute of Physics [50]. In this chapter major RHIC experiments will be presented with a special focus on the BRAHMS experiment and its results.

2.2. RHIC

Relativistic Heavy Ion Collider (RHIC) [51] is currently (as of mid-2006) the largest operating collider in the world. It is located in the Brookhaven National Laboratory (BNL), USA. The whole complex, schematically plotted in Figure 2.1, consists of several stages of particle accelerators, beginning with Tandem Van De Graaff [52], Linear Accelerator (LINAC) [53], Booster [54] and Alternate Gradient Synchrotron (AGS) [55]. Tandem uses static electricity to accelerate ionized atoms. LINAC is used for proton acceleration. Booster accelerates ions using radio frequency electromagnetic waves and is used as a pre-accelerator for AGS to increase the intensity of beams. AGS hosted many experiments since 1960s’ - three Nobel Prizes were won using data taken at AGS. Since 2000 it is accelerating ions and injecting them into RHIC at energy of about 10 GeV per nucleon.

RHIC is located in a circular tunnel with a circumference of almost 4 kilometers. Ions are bent to move around by a set of super-conducting magnets and accelerated by a radio frequency (RF) system up to energy of 100 GeV per nucleon. The two beam pipes intersect in six places to collide the ions traveling in opposite directions. Four of them host experiments, as depicted in Figure 2.1. They are: STAR [56],

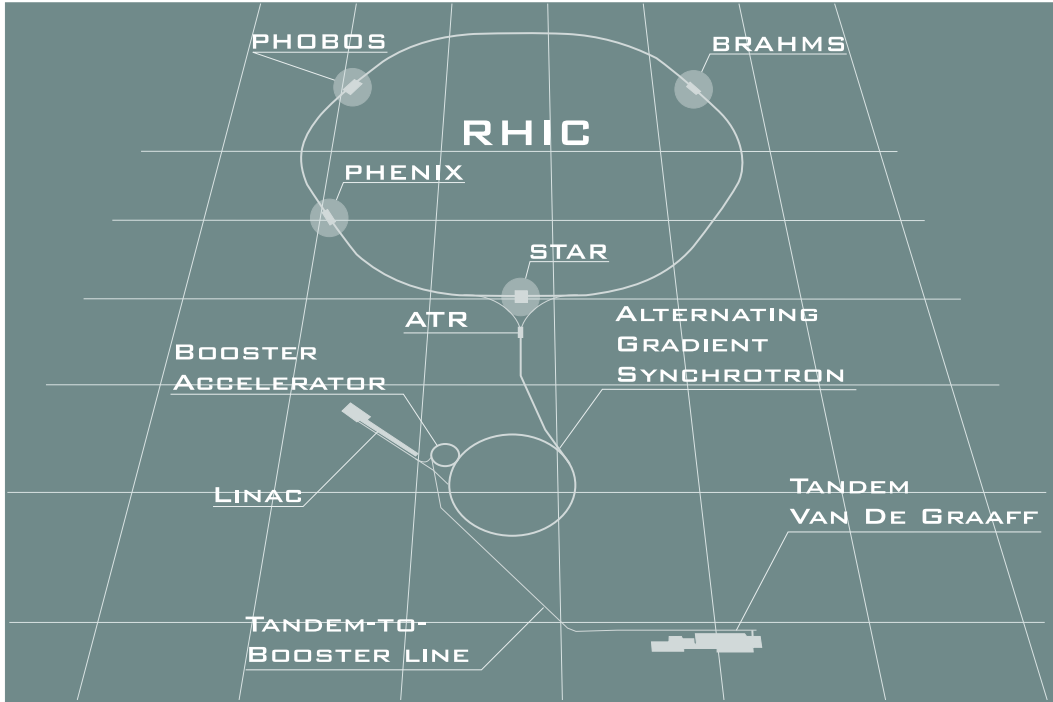


Figure 2.1. Schematic view of RHIC facility and experiment locations.

PHENIX [57], PHOBOS [58] and BRAHMS [59]. Up to now, there were four different systems at several energies colliding at RHIC, as listed in the Table 2.1, where beam luminosities (Ldt) for each system are also given.

2.3. Experiments

2.3.1. STAR

The Solenoidal Tracker At RHIC (STAR) is one of two largest RHIC experiments. It was design to detect hadrons emitted in the collision with use of the Time Projection Chamber (TPC) located inside huge magnet that bends the particles, thus making possible momentum measurements. For better vertex determination a Silicon Vertex Tracker is placed near the collision region. Particle identification (PID) is done using Electro-Magnetic Calorimeter and Time-of-Flight detectors placed between TPC and magnet. STAR is the only one RHIC detector with full azimuthal coverage in particle detection and identification. It is well suited for otherwise dif-

Run	Year	Species	$\sqrt{s_{NN}}$ [GeV]	Ldt
01	2000	Au + Au	130	$1\mu b^{-1}$
02	2001/2	Au + Au	200	$24\mu b^{-1}$
		p + p	200	$0.15pb^{-1}$
03	2002/3	d + Au	200	$2.74nb^{-1}$
		p + p	200	$0.35pb^{-1}$
04	2003/4	Au + Au	200	$241\mu b^{-1}$
		Au + Au	62.4	$9\mu b^{-1}$
05	2004/5	Cu + Cu	200	$3nb^{-1}$
		Cu + Cu	62.4	$0.19nb^{-1}$
		Cu + Cu	22.5	$2.7\mu b^{-1}$
		p + p	200	$3.8pb^{-1}$

Table 2.1

Table of RHIC species and energies.

difficult measurements like non-statistical fluctuations of event multiplicity, particle interferometry and tomography of high- p_T jets. Its experimental setup has also been adapted for strangeness measurements by detection of particle decays.

2.3.2. PHENIX

PHENIX (Pioneering High Energy Nuclear Interaction eXperiment) has been designed for good identification of direct probes, that is particles which, after being produced in heavy ion collisions, do not interact with the created medium (leptons and photons). Main parts of the two central arms are the Drift Chambers (DC) for charged particles momentum reconstruction and for particle identification. Electrons are identified mainly by use of the Ring Imaging Cherenkov and Aerogel Cherenkov Counter, while photons by measurements in the Electromagnetic Calorimeter. Forward muon arms serve for muon detection. The whole setup is complemented by the vertex detectors and three large magnets for bending charged

particles. Detector system in mid-rapidity covers about half of the azimuthal space in two opposite arms, which allows for study of high- p_T jets and other particle correlations measurements.

2.3.3. PHOBOS

PHOBOS is a much smaller experiment than the two presented above and its exceptionality lies in detection of low momentum hadrons. It measures momenta of only a small fraction of hadrons produced in a collision, by use of the two spectrometers built of silicon detectors. Particle identification is done by $\Delta E/\Delta x$ measurements and are supplemented by the Time-of-Flight and Calorimeter detectors. The most unique part of PHOBOS is however the finely partitioned Octagon barrel that is used for precise measurement of charged particle multiplicity in a wide range of rapidity together with their azimuthal distribution.

2.4. BRAHMS

Broad RAnge Hadron Magnetic Spectrometers (BRAHMS) ¹ experimental setup has been presented in details in [61]. The name comes from the two spectrometer arms, called Mid-Rapidity Spectrometer (MRS) and Forward Spectrometer (FS). Schematic view of the experimental setup is shown in Figure 2.2.

Detectors designed to measure event characteristics like vertex position, multiplicity and reaction plane are called global detectors. Zero Degree Calorimeters (ZDC), shown in bottom-right panel of Figure 2.3, are placed on each side of the nominal interaction point along the beam axis at a distance of 18 meters. These lead-tungsten calorimeters are the same for all four RHIC experiments and serve for comparing beam luminosities delivered to different experiments. Placed behind the RHIC bending magnets (DX) they measure spectator neutrons. Time information provided by ZDCs are used for determination of collision vertex position.

Two Beam-Beam Counters (BB) (top panel in Figure 2.3) are located 2.2 meters away from the nominal vertex and consist of a set of Cherenkov detectors with Photo Multiplier Tubes (PMT) mounted at the back to detect Cherenkov light created by charged particles. Left array consists of 8 large (51 mm diameter, 3 cm radiator)

¹For the full BRAHMS Collaboration author list see Appendix A.

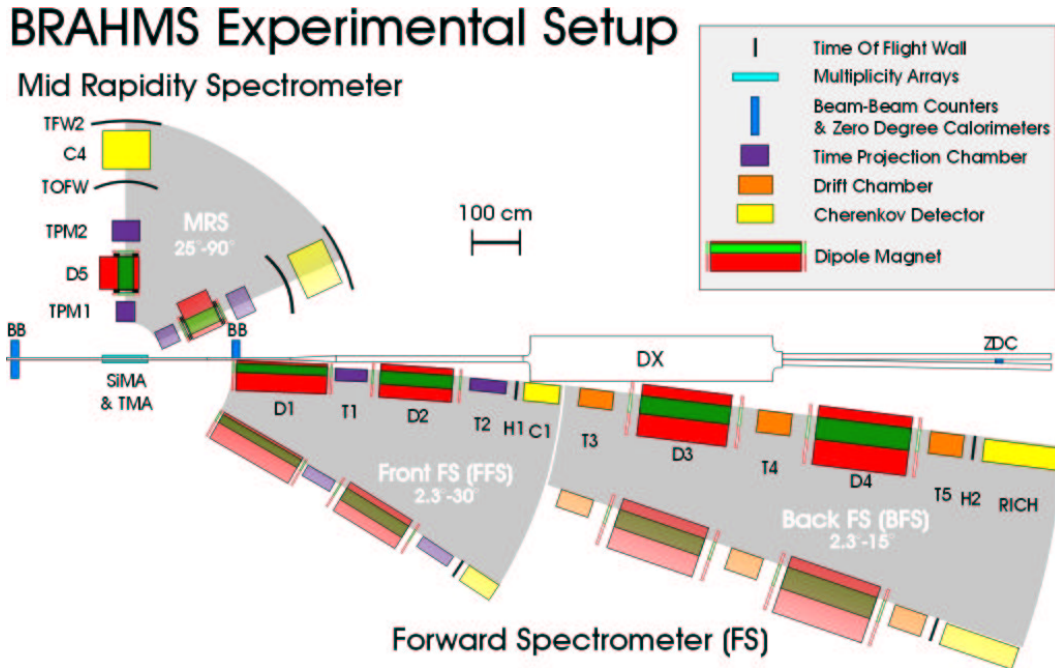


Figure 2.2. Schematic view of the BRAHMS experimental setup.

and 36 small (19 mm diameter, 4 cm radiator) Cherenkov detectors. Right array is smaller and asymmetric, to give way for the FS arm, there are 5 large and 30 small tubes here. Time difference lets measurement of the collision vertex. Energy deposited in the BB is used to estimate the number of charged particles, assuming average energy loss as for Minimum Ionizing Particles (MIPs).

There are two barrels of Multiplicity Arrays placed around the nominal interaction region, shown in bottom-left panel of Figure 2.3. With a good coverage in rapidity $|\eta| < 2.2$ and azimuthal angle (about $2/3$) these detectors are well suited for charged particle multiplicity measurements. They are also used for detection of a reaction plane and flow analysis. Both barrels are hexagonal in shape, inner one consists of silicon stripe (SiMA) detectors, while the outer one of scintillator tiles (TMA). In the acceptance regions of the two spectrometers the Multiplicity Arrays are lacking slats to minimize scattering and absorption of the particles.

Two spectrometer arms are the most unique parts of the BRAHMS experiment designed for detection of charged hadrons (pions, kaons, protons and their antiparti-

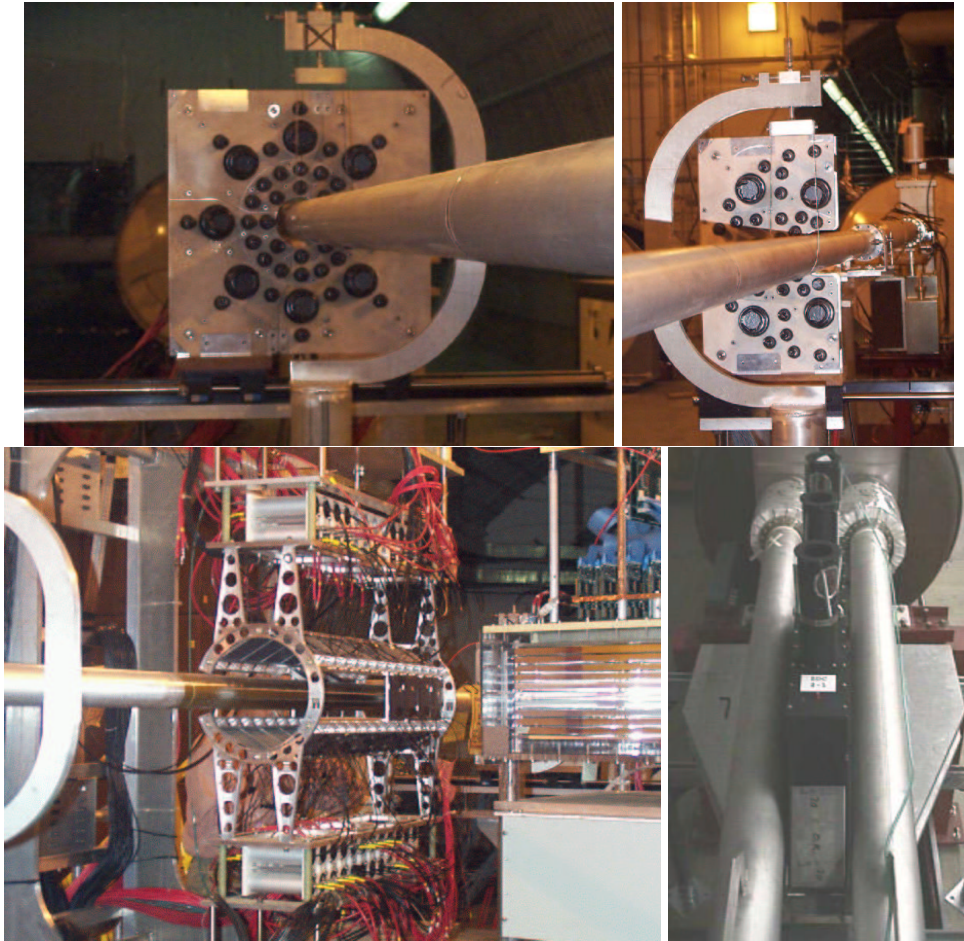


Figure 2.3. Photographs of the global detectors. In the top pictures the BB detectors are shown. Bottom pictures show the MA (left) and the ZDC (right).

cles) in the largest rapidity range as compared to other three experiments described above. They have excellent momentum resolution and identification capabilities up to very high transverse momenta. They both are movable and rotate around the nominal interaction point in the azimuthal plane. MRS can rotate from 90° to 30° which translates to rapidity coverage of $|y| < 2$. FS contains of two parts, Front (FFS) which rotates from 2.3° to 30° ($2.2 < y < 3.5$) and Back (BFS) with angular span of 2.3° to 15° degrees ($2.5 < y < 3.5$). The arms have conceptually very similar design: a magnet to bend charged particles, two tracking chambers before and after the magnet to detect the particle track, hodoscope detector and Cherenkov detector

at the end that serve for particle identification. This standard setup is slightly modified in case of each part. Figure 2.4 summarizes acceptance of the spectrometer arms for identified hadrons.

The MRS (see Figure 2.2) consists of two time projection chambers (TPC) TPM1 and TPM2, a dipole magnet D5, time-of-flight walls TOFW and TOFW2 and a Cherenkov threshold detector C4. FFS is built of two TPCs: T1 and T2, a dipole magnet D2, a hodoscope detector H1 and Cherenkov threshold detector C1. Additional magnet D1 in front of the arm bends the incoming particles extending BRAHMS acceptance in the forward region to rapidity 3.9. BFS (see Figure 2.2), which role is to improve BRAHMS particle identification for high momentum particles and extend the rapidity coverage, consists of three drift chambers (DC), marked in Figure 2.2 as T3, T4 and T5, two magnets D3 and D4, a hodoscope detector H2 and a ring imaging Cherenkov detector (RICH). The drift chambers [62] together with the Front End Electronics (FEE) were designed and constructed by members of the Polish group in the Hot Matter Physics Division of the Marian Smoluchowski Institute of Physics at Jagiellonian University in Kraków.

Photos of various parts of the BRAHMS experimental setup are seen in Figure 2.5. In table 2.2 particle identification limits in momentum for various parts are presented.

	$0 < \eta < 1.0$			$1.5 < \eta < 4.0$		
	TOFW	TOFW2	C4	TOF1	TOF2	RICH
K/π	2.0	2.5	-	3.0	4.5	25.0
K/p	3.5	4.0	9.0	5.5	7.5	35.0

Table 2.2

Upper range of the momentum for 2σ separation (in GeV/c)

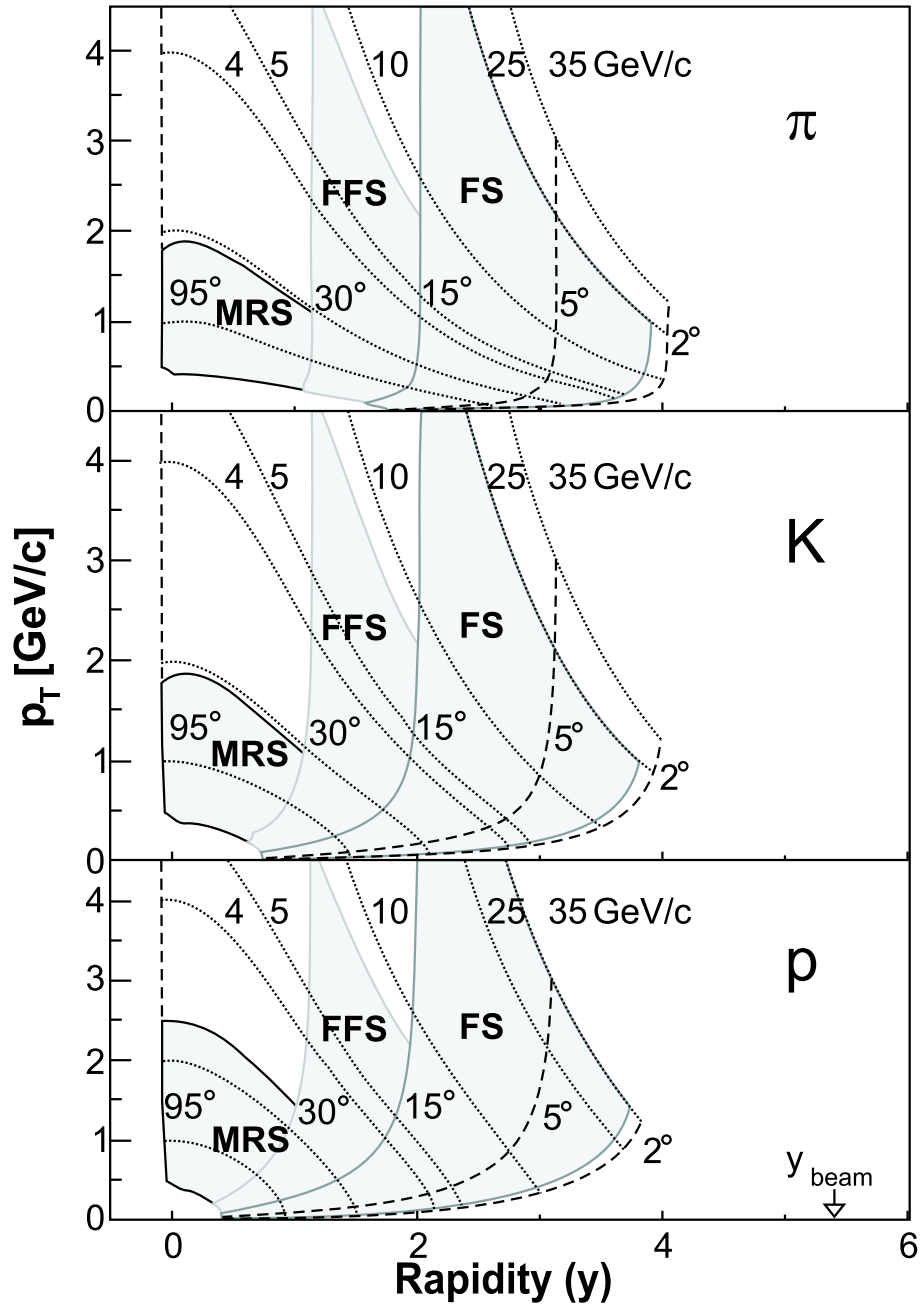


Figure 2.4. BRAHMS detectors acceptances for pions, kaons and protons in the MRS, FFS and full FS spectrometer arms. The dotted curves marked 4, 5, 10, 25 and 35 GeV/c are curves of constant momentum, while the set marked 95°, 30°, 15°, 5°, 2° indicate curves at a constant polar angle. The fully drawn curves mark the acceptance borders.

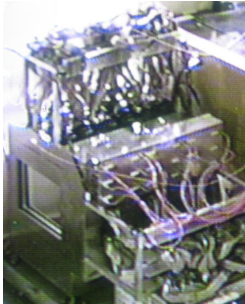
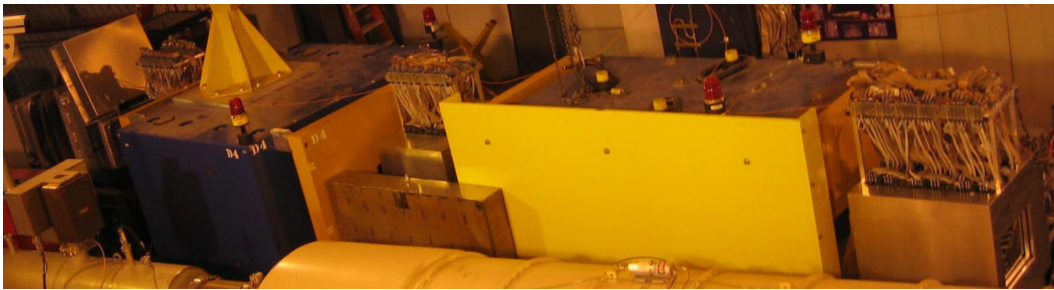


Figure 2.5. BRAHMS spectrometer arms. Top panel shows FFS and MRS, middle one BFS. Bottom panel shows T3 detector (left) and T4, D4, RICH (right).

2.5. Relativistic heavy ion collision

2.5.1. Introduction

The ions that are accelerated in RHIC are moving with ultrarelativistic velocities of about 99.995% c . This value is however barely used in physics, it is more

common to talk about the energy and rapidity. The energy of the moving ions can reach 100 GeV per nucleon, that is about 100 times greater than the rest mass of the nucleon (if we take $c = 1$). The rapidity (y) is defined as:

$$y = \frac{1}{2} \log \frac{E + p}{E - p} = \tanh^{-1} \frac{p}{E}, \quad (2.1)$$

where E is the energy of the particle, and p its momentum. The quantity is also used for describing the longitudinal momentum of the particles created in the reaction, and then p is exchanged by the particle longitudinal momentum (p_L) along the beam direction. For unidentified high energy particles ($E \rightarrow \infty$) it is common to use simpler quantity, called pseudo-rapidity η defined as:

$$\eta = -\log \tan\left(\frac{\theta}{2}\right), \quad (2.2)$$

where θ is the angle between the particle and the direction of the beam. The rapidity and pseudo-rapidity are essentially the same for particles with transverse momenta larger than the mass of measured particles, that is above $p_T \approx 1.5 \text{ GeV}/c$.

2.5.2. Initial state

The moving ions appear to be disk-like objects in the lab frame, because the length in the direction of the movement is contracted by a Lorentz γ factor, which is about 100 in case of ions at the top RHIC energy. This influences the density of partons inside the nuclei, and the time that takes for the two ions to pass each other.

From Deep Inelastic Scattering (DIS) experiments it is known that nucleons are not simply composed of three quarks. As the energy transfer grows one observe increasing content admixture of sea quarks and strong enhancement of gluon density. Sea quark distribution increases with decreasing Bjorken ² x . Gluon composition dominates below $x = 0.02$ and steeply increases with decreasing x [66], as seen in Figure 2.6.

Therefore low x part of the rapidly moving heavy ion can be treated as a condensed wall of color gluons. Due to the time dilation connected with the relativity

²The scaling variable introduced by Bjorken [63], $x = Q^2/2P \cdot q$, where P is the four-momentum of the proton, q is the four-momentum transfer in DIS, and $Q^2 \equiv -q^2$. Feynman [64] defined x as the fraction of the longitudinal particle's momentum p carried by the parton, $x = k_{||}/p$. It was later shown [65] that for large x the two are equivalent.

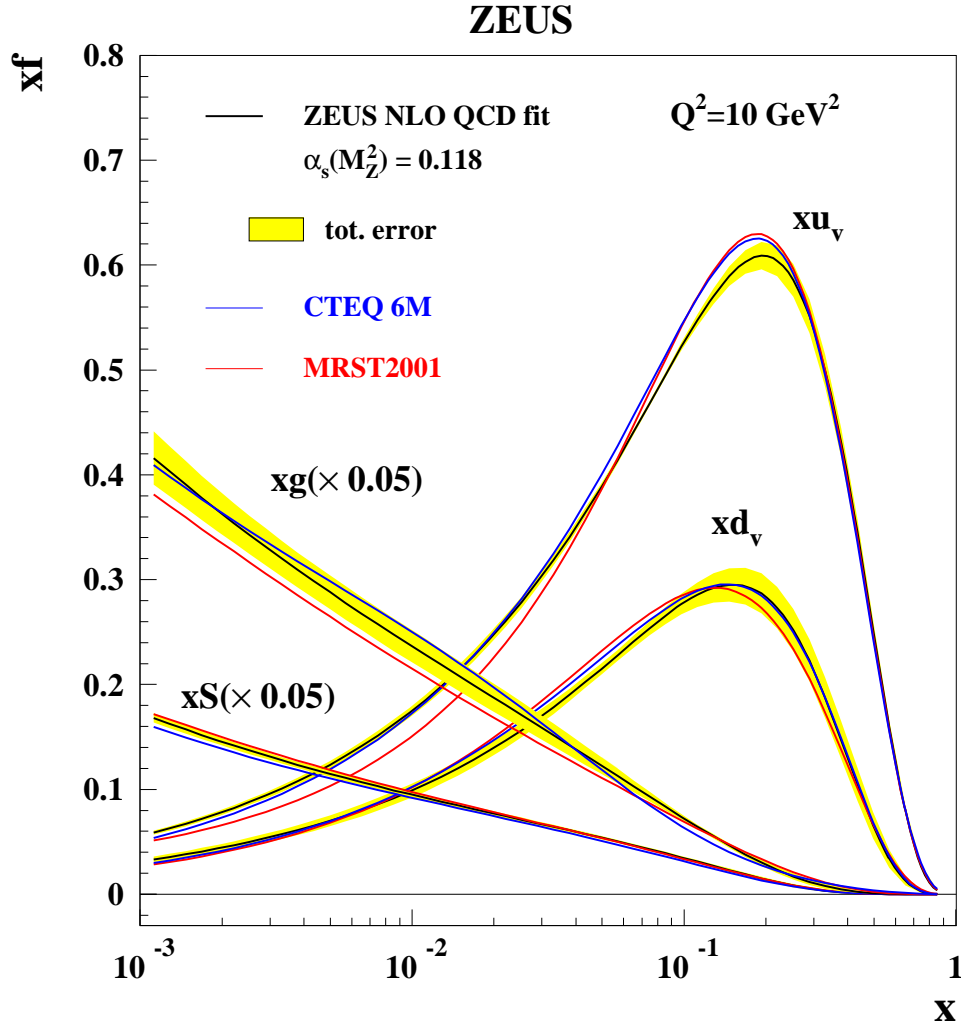


Figure 2.6. The gluon (xg), sea quark (xS), u (xu_v) and d (xd_v) valence quarks distributions extracted from the standard ZEUS-NLO QCD fit at $Q^2 = 10 \text{ GeV}^2$. Figure taken from Ref. [66].

transformation, inner time of the nuclei goes slower by a factor of about 100 in respect to the laboratory time. The physical processes in the moving nucleus as observed in the rest frame appear to be slowed down, and quickly moving gluons in the rest frame appeared to be frozen, as in glass. Therefore this feature is often referred to as the Color Glass Condensate (CGC) [67].

Extremely important parameters describing collision are the impact parameter

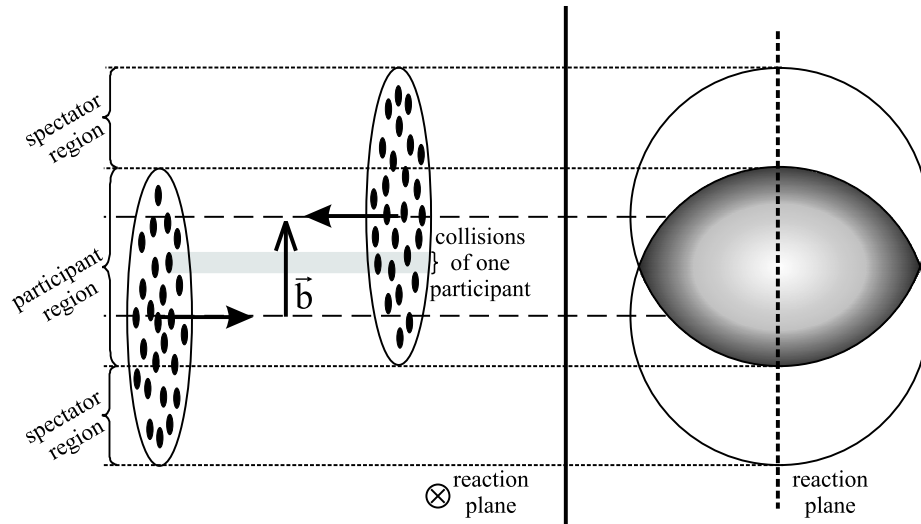


Figure 2.7. Participant and spectator picture of the nucleus-nucleus collision. Left part shows view perpendicular to particle trajectories, right one is view from behind one of the projectiles.

and reaction plane, see Figure 2.7. The reaction plane is the plane that contains the trajectories of both colliding nuclei, and the impact parameter is the distance between the two trajectories. The impact parameter (\vec{b}) is responsible for centrality of the collisions - central collisions are those with small impact parameters and large impact parameters are for peripheral events. For semi-central and peripheral collisions most of particle production is located in the reaction plane. These nucleons of the colliding nuclei that take part in the collision are often referred to as participants, while all the rest are spectator nucleons (see Figure 2.7). Another important quantity is the number of binary collisions, which is a count of elementary nucleon-nucleon collisions. For $p + p$ reaction, there are two participants and one collision, however in nucleus-nucleus collisions one participant can interact with several nucleons from the other nucleus (see Figure 2.7) and thus number of collisions rises fast with the size of the reacting system.

2.5.3. Collision

In the following paragraphs various stages of ultra-relativistic heavy ion collision will be reviewed. Surprisingly, heavy ion collision at that high energies characterizes with a high degree of transparency. It means that particles observed in the mid-rapidity region are almost all produced in the collision, while the particles that before the collision were constituents of the nuclei are peaked at large rapidities. The idea of transparency may be imagined if it is remembered that the nuclei are Lorentz contracted and the time dilation causes that the nucleons simply do not have time to react to the quickly changing conditions in the reaction. However because of the actual contact between nuclei the strong color field will extend between various partons (quarks and gluons) from the opposite nuclei. After time of about $\tau_0 = 1 \text{ fm}/c$ the system equilibrates and reaches QGP state, as shown in Figure 2.8. The matter expands and gradually cools down. At later time temperature drops to a value T_c , when quarks and gluons cannot any longer be treated as free - they hadronize. Created particles can still change their quark content until their energies are large enough. The moment when the particles in the medium can no longer mix is called the chemical freeze-out and is achieved when system cools down to temperature T_{ch} . Hadrons continue to interact with each other until temperature is larger than T_{fo} , referred to as thermal freeze-out.

2.6. Review of the BRAHMS experimental results

The whole experimental information on state of matter produced in ion collision is carried by emitted particles and electromagnetic radiation. Unfortunately detection of particles emitted from the QGP phase is difficult, because they can interact many times before leaving the interaction region. Luckily photons and electrons that do not interact strongly, leave the zone almost undisturbed. Therefore photons and leptons are called direct probes. In the following sections I will review the experimental results obtained by the BRAHMS Collaboration. Author of this work contributed do these results from year 2001.

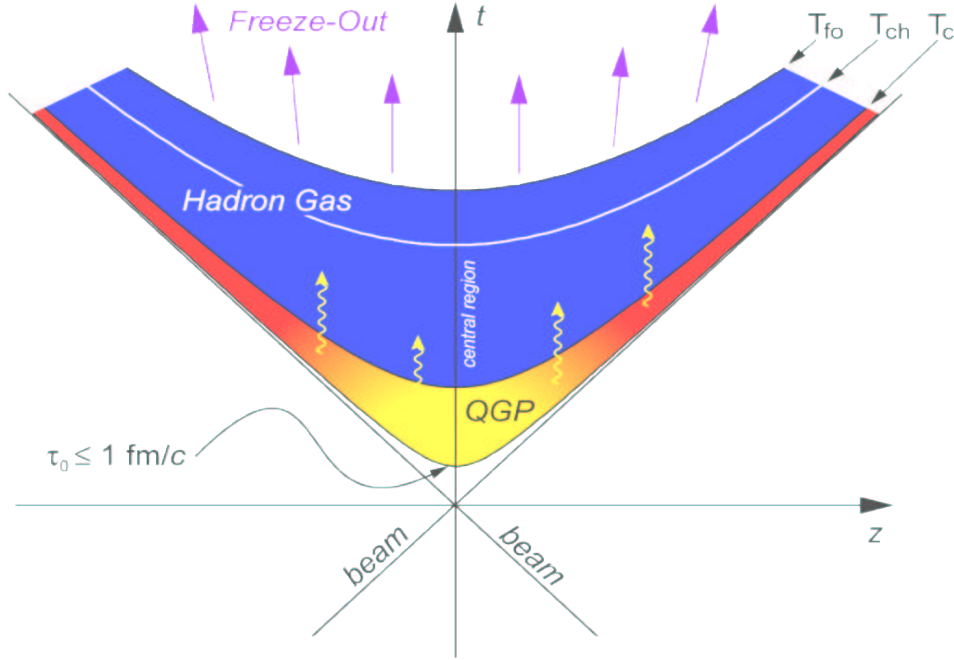


Figure 2.8. Schematic view of the time evolution of the collision.

2.6.1. Energy density

The most important indicator of whether or not medium is in the QGP state are its energy density ε and temperature. In 1983 Bjorken [68] already proposed a simple formula to estimate the energy density:

$$\varepsilon = \frac{3 \langle E_t \rangle}{2 \pi R^2 \cdot \tau_0} \frac{dN_{ch}}{d\eta}, \quad (2.3)$$

where τ_0 is the time required for the system to achieve equilibrium state, usually taken to be 1 fm/c, R is the radius of the nucleus, for Au + Au collision it is about 6 fm. Factor of 3/2 in the formula scale the number of charged particles ($\frac{dN_{ch}}{d\eta}$) to estimate total particle multiplicity. $\langle E_t \rangle$ is the particle average transverse energy, which has been measured by BRAHMS to be about 0.5 GeV.

BRAHMS experiment has measured particle multiplicity [69] in Au + Au collisions at $\sqrt{s_{NN}} = 200$ GeV in the wide range of pseudo-rapidity from -4.5 to 4.5, as a function of centrality. Results are seen in Figure 2.9. For the most central collisions

(0 – 5%) about 4500 charged particles were detected in the whole rapidity range, of which 625 were observed in the mid-rapidity region ($\frac{dN_{ch}}{d\eta}|_{|\eta|<0.5} = 625 \pm 56$). This measurement sets the estimation of energy density at about $\varepsilon \approx 5 \text{ GeV}/\text{fm}^3$, which is about 30 times higher than the energy density of nuclear matter³ and about 10 times the hadron density⁴. This value greatly exceeds the predicted boundary between hadron and QGP regions by lattice QCD calculations [47].

It is remarkable to notice the surprising flatness of multiplicity in the mid-rapidity region. The fact was already predicted by Bjorken in 1983 and was called boost invariance.

2.6.2. Net-proton distribution

The boost invariance of the charged particle multiplicity distribution at mid-rapidity unseen at lower energies is much more distinct when looking at the net-proton distribution. As particles are indistinguishable and they do not have special marker of having been produced in collision or being the primary ones, a special method has to be applied. It is argued that the proton and antiproton production in the collisions is identical. Thus comparing the observed yields of that particles one can deduce the distribution of the original protons called the net-proton distribution [71]. The resulting points are seen in Figure 2.10. In the same figure similar distributions obtained in collisions at AGS [72] and SPS [73] has been presented. It shows that the transparency of the collision grows with the colliding energy, so that at RHIC considerable transparency is observed.

Another observable directly connected to the net proton distribution is the average rapidity loss experienced by the participant nucleons. It is calculated from the rapidity net proton distribution. BRAHMS limited coverage does not allow for measurements at rapidities close to the beam rapidities, but results obtained so far (see Figure 2.11) indicate that the rapidity loss is smaller than the value suggest by extrapolations from lower energies. Nevertheless the total energy loss accumulates

³Energy density of nuclear matter may be estimated with $\rho_{n.m.} = \frac{A \cdot m_n}{\frac{4}{3}\pi(R_0 A^{\frac{1}{3}})^3} \approx 0.13 \text{ GeV}/\text{fm}^3$, where

A is the atomic number, $R_0 = 1.2 \text{ fm}$ and nucleon's mass $m_n = 0.938 \text{ GeV}/c^2$.

⁴Energy density of hadron may be estimated with $\rho_h = \frac{m_h}{\frac{4}{3}\pi r_h^3} \approx 0.44 \text{ GeV}/\text{fm}^3$, where radius of nucleon is between $r_n \approx 0.805 \pm 0.011$ and $0.862 \pm 0.012 \text{ fm}$ [70].

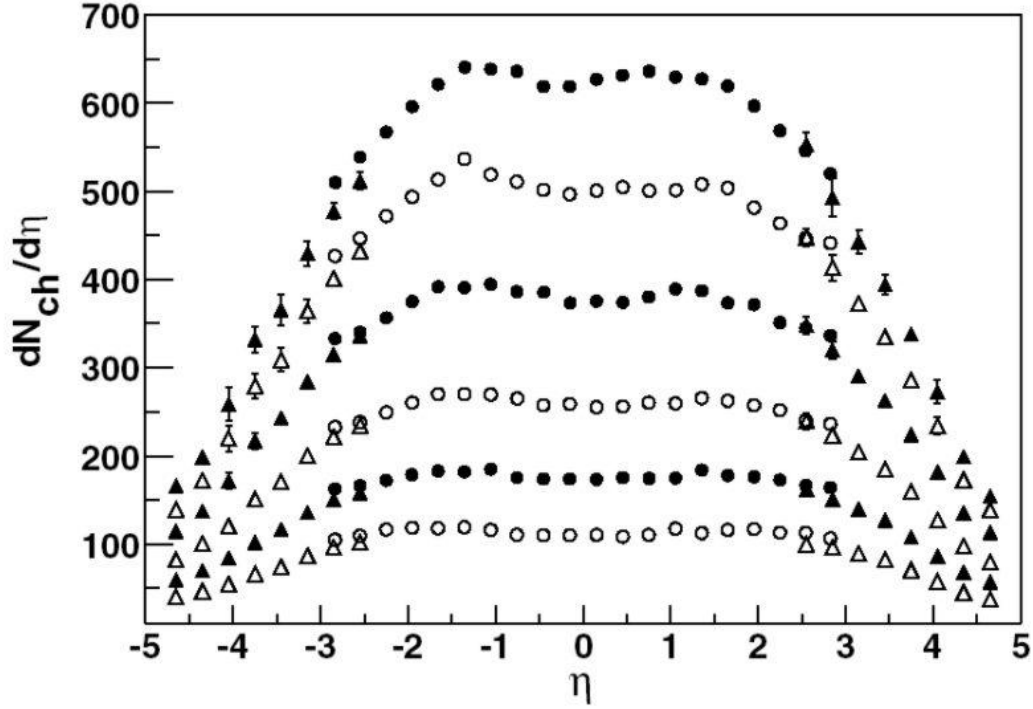


Figure 2.9. Distribution of $dN_{ch}/d\eta$ for centrality ranges of, top to bottom, (0 – 5)%, (5 – 10)%, (10 – 20)%, (20 – 30)%, (30 – 40)% and (40 – 50)%. The SiMA and BB results are indicated by circles and triangles, respectively. Statistical errors are shown for all points where they are larger than the symbol size. Figure taken from [69].

to about 26 TeV per central Au + Au collision, which accounts to almost 75% of the initial energy available for excitation.

2.6.3. Chemical freeze-out

BRAHMS results on particle ratios [74] are seen in Figure 2.12. The figure shows the rapidity dependent ratios of yields of antihadrons to hadrons for the three particle species detected by the BRAHMS experiment, that is pions, kaons and protons, and their antiparticles. We observe the ratios practically flat in the rapidity range below one, and very close to unity. The fact indicates that the particle production in this region is dominated by pair creation. The apparent symmetry in particle/anti-

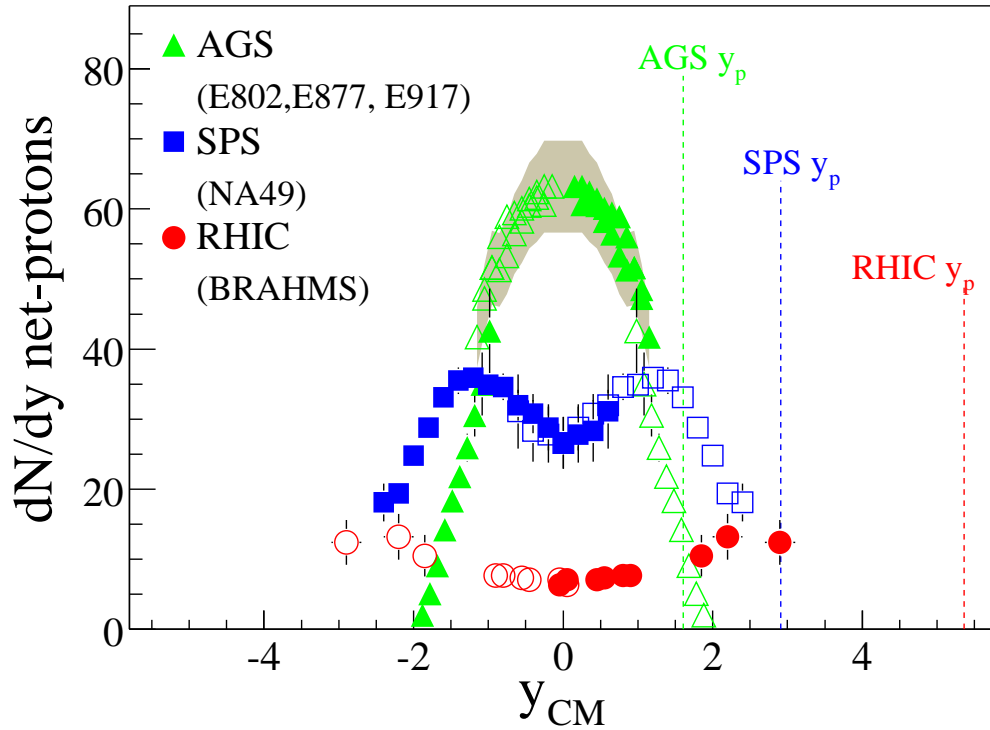


Figure 2.10. Net-proton rapidity density dN/dy as a function of rapidity at AGS [72] (Au + Au at $\sqrt{s_{NN}} = 5$ GeV), SPS [73] (Pb + Pb at $\sqrt{s_{NN}} = 17$ GeV) and in BRAHMS [71] (Au + Au at $\sqrt{s_{NN}} = 200$ GeV). The data are all for 5% most central collisions. Errors shown both statistical and systematic errors. The data have been symmetrized (see [71]).

particle production for pions is broken for kaons and protons due to asymmetry in strangeness production and reminiscent net-proton. These effects increase with growing rapidity, therefore the ratios decrease.

Antiparticle to particle ratios can also be used as an input for the statistical model. Amazingly simple dependence of antikaon to kaon ratio on antiproton to proton ratio is observed in wide range of energies and rapidities. Figure 2.13 shows BRAHMS experiment data at various rapidities and energies. AGS [75] and SPS [76] results at mid-rapidity are also shown.

Assuming that the expanding system achieves at some time chemical and thermal

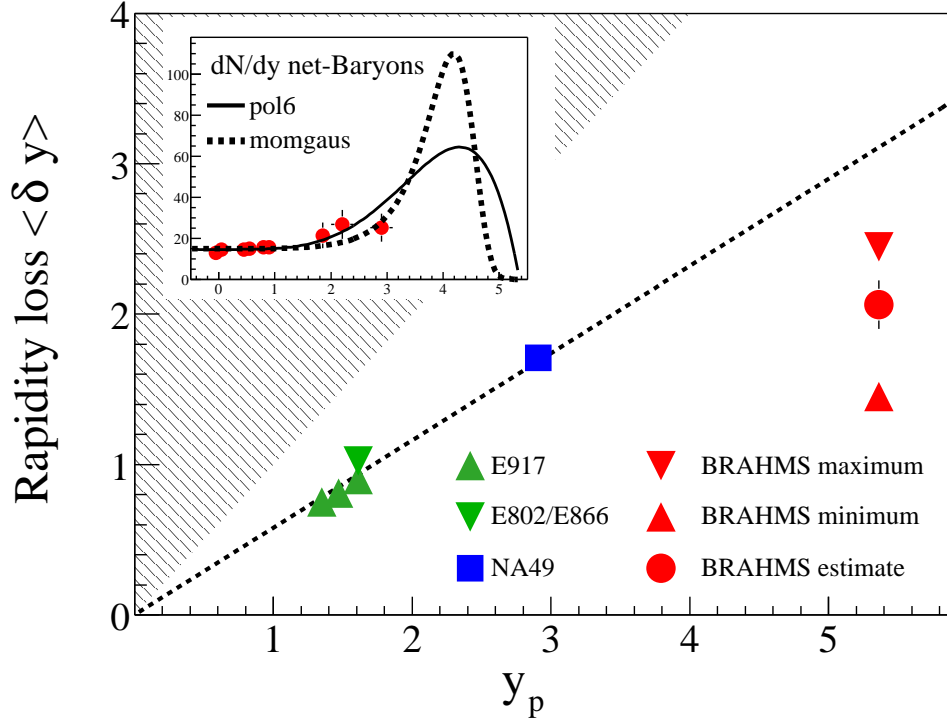


Figure 2.11. Rapidity loss as a function of projectile rapidity (in the CM). The hatched area indicates the unphysical region, and the dashed line shows the phenomenological scaling $\langle \delta y \rangle = 0.58 y_p$. Figure taken from [71].

equilibrium, the ratios can be written as:

$$\frac{\rho(p)}{\rho(\bar{p})} = \exp\left(\frac{-6\mu_{u,d}}{T}\right) \quad (2.4)$$

and

$$\frac{\rho(K^-)}{\rho(K^+)} = \exp\left(\frac{-2(\mu_{u,d} - \mu_s)}{T}\right) = \exp\left(\frac{-2\mu_s}{T}\right) \times \left[\frac{\rho(p)}{\rho(\bar{p})}\right]^{\frac{1}{3}}, \quad (2.5)$$

where ρ is the particle density, μ is the quark chemical potential, and T the temperature. Dotted curve in Figure 2.13 is obtained if strange chemical potential equals zero. The curve does not reproduce experimental points, however the function $\frac{\rho(K^-)}{\rho(K^+)} = \left[\frac{\rho(p)}{\rho(\bar{p})}\right]^{\frac{1}{4}}$ obtained with $\mu_s = 1/4\mu_{u,d}$ reproduces them remarkably well. This simple correlation persisting over a wide range of collision energies and rapidities in

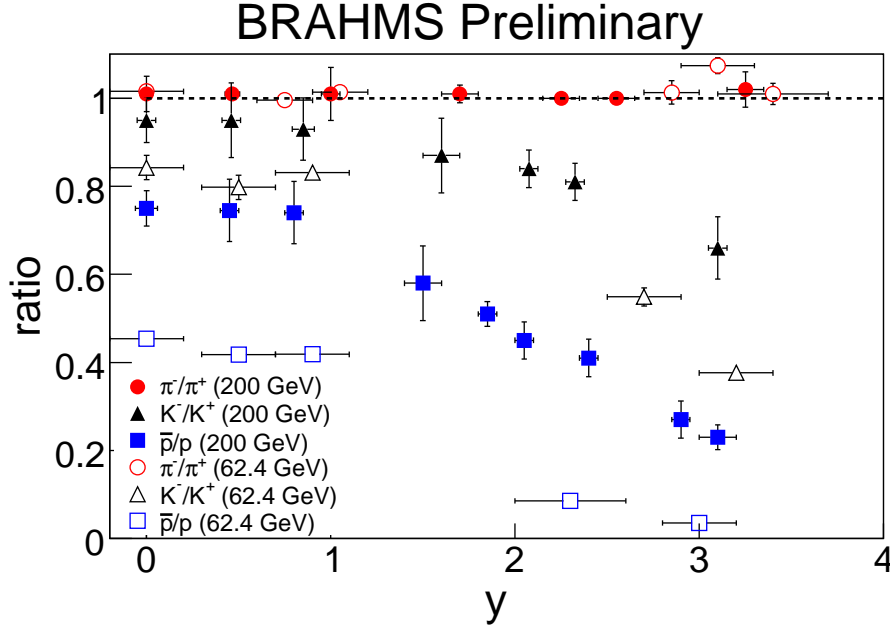


Figure 2.12. Ratios of anti-particles to particles (pions, kaons and protons) as a function of rapidity for Au + Au collisions at $\sqrt{s_{NN}} = 62.4$ and 200 GeV. Statistical and systematic errors are indicated. Figure taken from [77].

heavy ion collisions suggests existence of some simple primordial mechanism relating the strange and baryonic chemical potentials. Data obtained by NA49 and STAR on other particles containing strange quarks are also well fitted using $\mu_s = 1/4\mu_{u,d}$. It is important to look for theoretical explanation of the fact, and also to search for similar relation for heavier quarks.

Statistical model uses simultaneous fits to many particle species to obtain chemical potentials and temperature. Example fit in Becattini statistical model [78] is presented in Figure 2.13 as full line. The resulting temperature is 170 MeV and is interpreted as the temperature of the chemical freeze-out.

2.6.4. Thermal freeze-out

The temperature of thermal freeze-out may be deduced from the transverse momenta distribution of charged particles. Statistical reasons make the spectrum Maxwellian with a slope inversely proportional to the temperature (T_{fo}) of the source. Non-statistical phenomena in the medium result usually in additional radial-flow veloc-

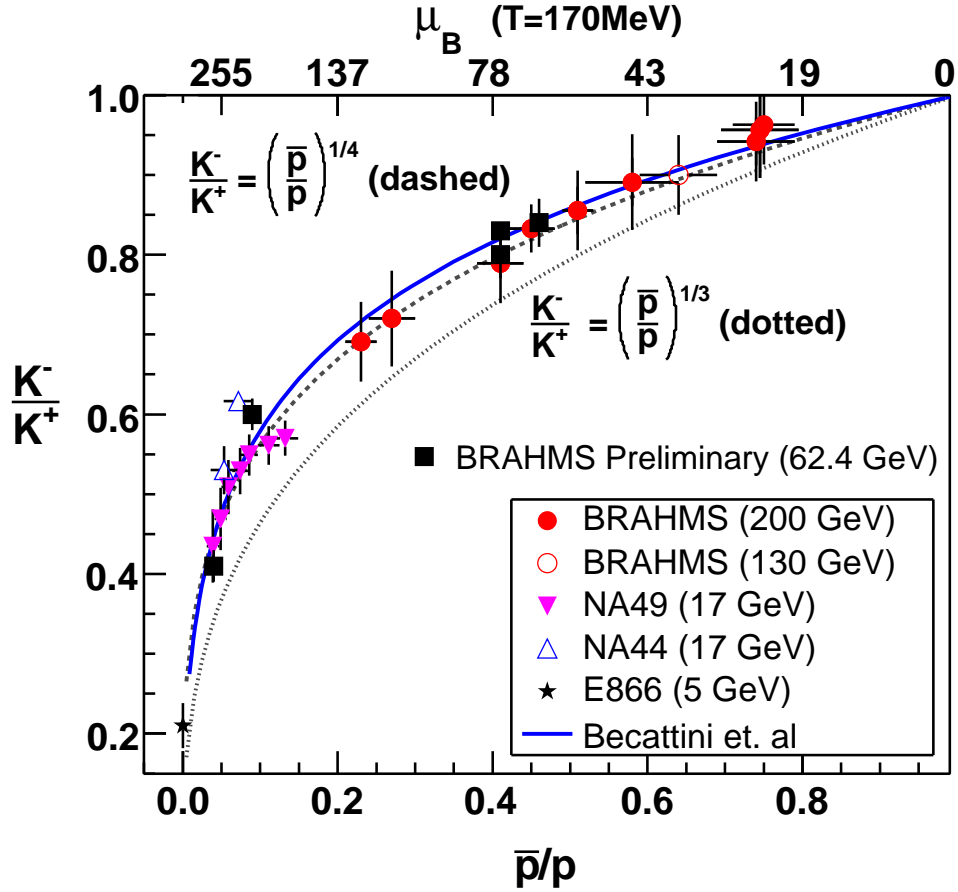


Figure 2.13. Correlation between K^-/K^+ and \bar{p}/p . The solid curve refer to statistical model [78] calculation with a chemical freeze-out temperature of 170 MeV. Figure taken from [77].

ity component (β_T) to the spectrum. These relationships have been merged in a blast-wave approach [79], where invariant m_T spectrum is fitted with function:

$$\frac{dN}{m_T dm_T} \propto \int_0^{R_{max}} r dr m_T I_0\left(\frac{p_T \sinh \rho}{T_{fo}}\right) K_1\left(\frac{m_T \cosh \rho}{T_{fo}}\right). \quad (2.6)$$

In the fit, I_0 K_1 and are modified Bessel functions, and $\rho = \tanh^{-1} \beta_T$ is the transverse rapidity. Source parameter is taken to be $R_{max} = 13$ fm for Au + Au collisions. For details see Ref. [80]. Results of simultaneous fits to various particle species are presented in Figure 2.14 as a function of the number of participants (i.e. centrality), and in Figure 2.15 as a function of rapidity.

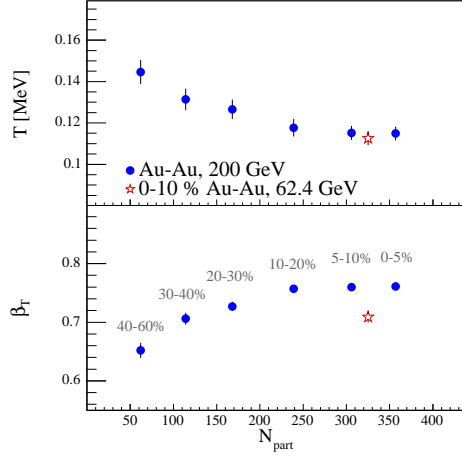


Figure 2.14. Kinetic freeze-out temperature and transverse flow velocity at mid-rapidity as a function of centrality for Au + Au at $\sqrt{s_{NN}} = 200$ GeV (dots). For the comparison we show result for 0 – 10% central Au + Au at $\sqrt{s_{NN}} = 62.4$ GeV (star). Figure taken from [77].

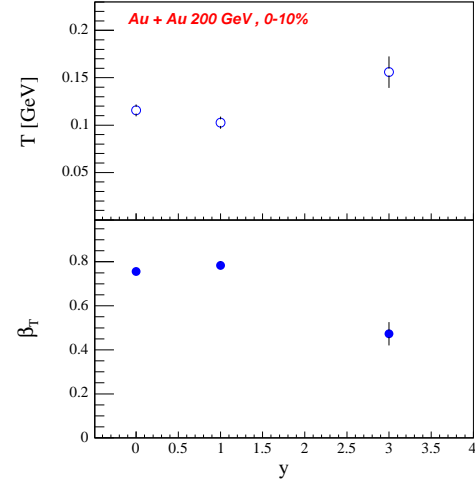


Figure 2.15. Kinetic freeze-out temperature and transverse flow velocity for central Au + Au at $\sqrt{s_{NN}} = 200$ GeV as a function of rapidity. Figure taken from [77].

The temperature of the thermal freeze-out is about $T_f = 120 - 140$ MeV, and is systematically lower than the temperature of chemical freeze-out, which confirms the naïve expectation that the freeze-out of particle ratios occurs before particle cease to interact. Furthermore it should be noted that the temperature is consistent with that obtained at SPS [81]. However flow velocity observed at RHIC is a factor of 1.5 higher than that observed at lower energies of SPS [81] and is about $\beta_T = 0.70 - 0.75 c$. The fact is attributed to larger initial energy density which causes larger pressure and consequently higher collective velocities.

Slow rise of obtained freeze-out temperatures is observed when going to more peripheral events, while the flow velocity decreases. This is manifestation of the lower densities in peripheral events. Similar behavior of the quantities is observed

in rapidity. At the mid-rapidity region, when $|y| < 1.0$, similar to multiplicity distribution (sec. 2.6.1), temperature and velocity are essentially constant, while in the forward rapidity region both temperature and velocity are substantially different and indicate smaller initial density of the medium.

2.6.5. Elliptic flow

Particle production in non-central heavy ion collisions is not azimuthally homogeneous due to asymmetric shape of the fireball created in the collision. However the observed particle distribution does not simply follow the calculated shape of the initial partonic medium. The main reason for the discrepancies are the differences in the density gradient. Study of the effects are therefore important for better understanding of initial stages of the collision.

It is common to factorize the azimuthal distribution as:

$$\frac{d^3N}{dydp_Td\phi} = \frac{d^2N}{dydp_T} \times \frac{1}{2\pi} \times (1 + 2v_1(y, p_T) \cos \phi + 2v_2(y, p_T) \cos 2\phi + \dots), \quad (2.7)$$

where ϕ is the particle azimuthal angle in respect to the reaction plane. $\frac{d^3N}{dydp_Td\phi}$ is the triple differential distribution of emitted particles. Dependence on the azimuthal angle is expanded into a Fourier series, where coefficient v_1 is called direct flow and represents the enhancement of the observed yield in the direction of reaction plane (and in fact is used for extracting information about reaction plane from the particle distribution). The second coefficient (v_2) is called elliptic flow, and is a measure of the off-plane modifications to the particle production.

BRAHMS experiment has measured elliptic flow [82] for unidentified charged particles and pions, as a function of the transverse momentum at various rapidities. v_2 is a growing function of transverse momentum up to $p_T \approx 2 \text{ GeV}/c$ (see Figure 2.16). This observation is relatively good described by the three dimensional hydrodynamical calculations [83,84]. In the higher p_T region, which is unavailable for BRAHMS due to limited acceptance, v_2 for identified particles begins to saturate as seen by PHENIX [85] and PHOBOS [86]. STAR [87] shows that v_2 for charged hadrons stay flat up to $p_T \sim 5 - 6 \text{ GeV}/c$, after which it drops steadily in the region $5 < p_T < 12 \text{ GeV}/c$. Elliptic flow decreases with increasing collision centrality, which is confirmed by all experiments. Results obtained by BRAHMS

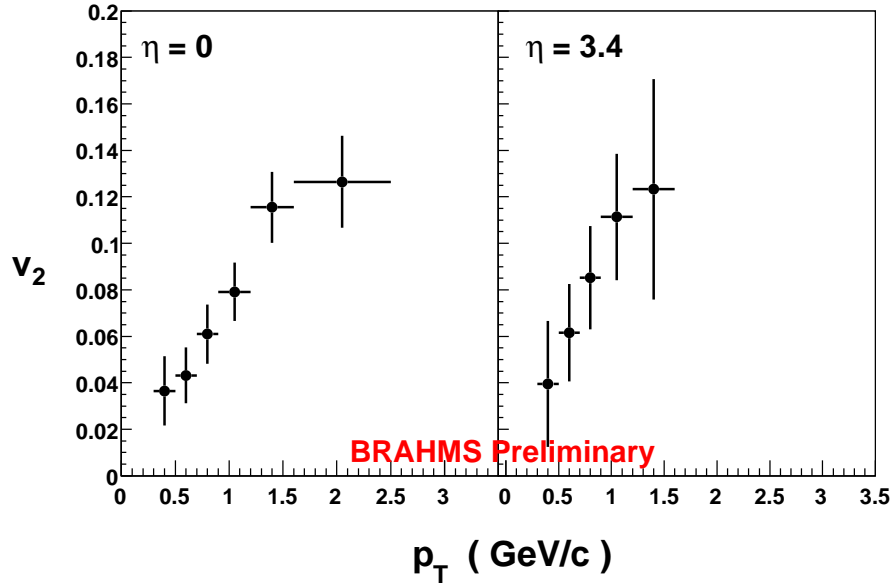


Figure 2.16. Elliptic flow of charged pions at $\eta = 0$ (left) and $\eta = 3.4$ (right). The data correspond to 10% – 20% central Au + Au events at $\sqrt{s_{NN}} = 200$ GeV. Only statistical errors are shown in the figure. Figure taken from [82].

experiment on rapidity dependence show very little change of integrated v_2 , which is presented in Figure 2.17. For comparison, PHOBOS [86] and STAR [87] measurements are also plotted in the figure. Both these experiments show that elliptic flow is a decreasing function of rapidity, which is also predicted by hydrodynamical models. The discrepancies may be caused by systematic errors introduced to BRAHMS results by extrapolation of the data to zero transverse momenta.

All experiments observe dependence of v_2 on quark content of the hadron - results for baryons are higher than for mesons. Figure 2.18 presents elliptic flow for various identified particles as obtained by STAR [87] in the low p_T region. Both axes of the plot has been divided by the number of valence quarks (n_q).

Intriguing scaling of the elliptic flow shows that the number of valence quarks is the most appropriate degree of freedom in description of flow. This result com-

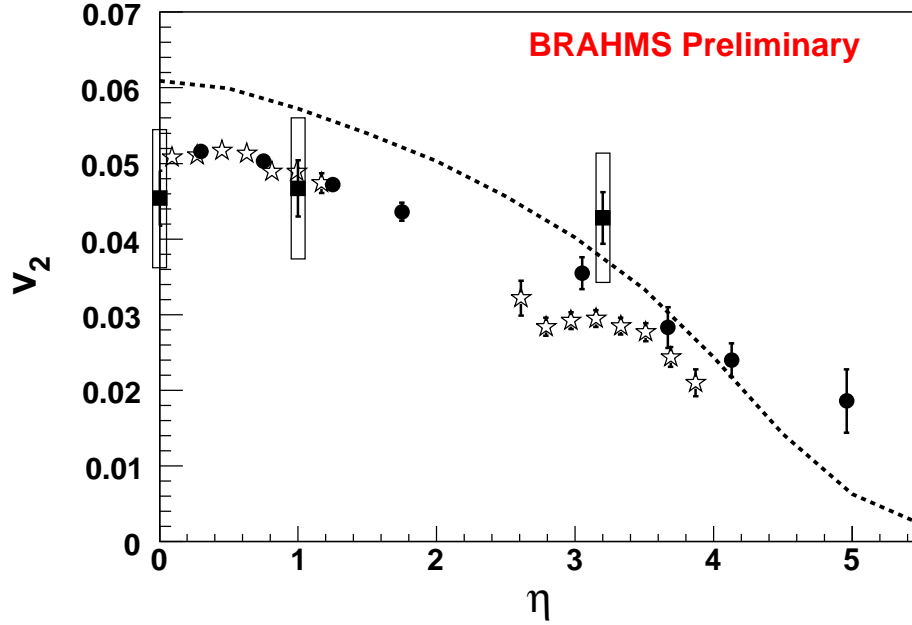


Figure 2.17. The p_T integrated elliptic flow of unidentified charge hadrons in Au + Au collisions at $\sqrt{s_{NN}} = 200$ GeV as a function of pseudo-rapidity. The square, circle and star symbols correspond to BRAHMS [82], PHOBOS [86] and STAR [87] data, respectively. The dotted line is a 3D hydrodynamic calculation [84]. Figure taken from [82].

bined with the achieved values of v_2 , which are larger than that obtained at SPS, and remain large in the intermediate p_T region, is very important in the discussion about nature of the matter produced in the collisions at RHIC. Although it cannot be treated as the final proof it strongly favor the claims that deconfined state of matter, QGP, is created in the relativistic heavy ion collisions.

2.6.6. Baryon enhancement

One of the most unexpected RHIC results [88] in Au + Au collisions at $\sqrt{s_{NN}} = 200$ GeV was the unusual enhancement in proton and antiproton yields for medium transverse momenta ($2 < p_T < 3$ GeV/ c) comparing to pion yields in this region.

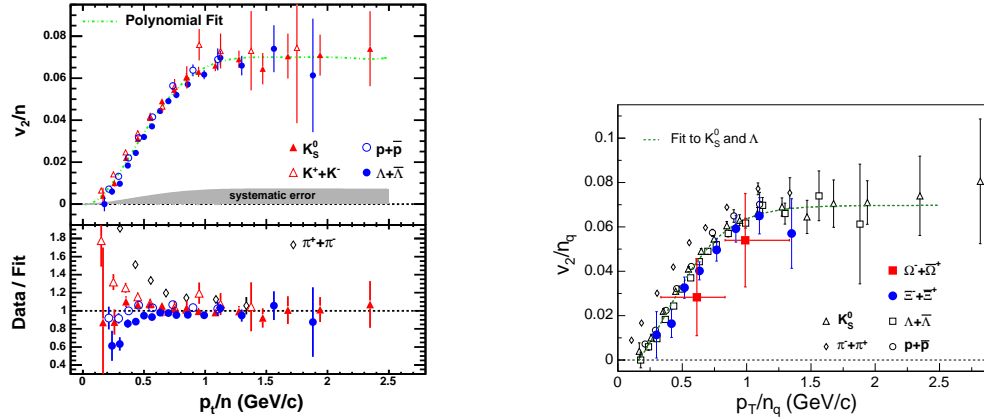


Figure 2.18. Identified particle v_2 from minimum bias collisions. The vertical axis and horizontal axis have been scaled by the number of constituent quarks (n). Left panel: kaons, protons and lambdas, right panel: pions, Λ 's, Ω 's and Ξ 's.

The latest BRAHMS results [89] are presented in Figure 2.19, where ratios of protons and antiprotons to pions are presented as a function of transverse momentum in Au + Au, Cu + Cu and p + p collisions at $\sqrt{s_{NN}} = 200$ GeV for two different rapidities. The ratios are generally an increasing function of transverse momenta up to $p_T \approx 2$ GeV/ c , while above this value observations suggest flattening of the ratios in the available p_T range. The value of the ratio saturation is the largest for Au + Au, smaller for Cu + Cu and the smallest for p + p collisions, which points out to the system size as one of the factors responsible for the value. Dependence on rapidity is in accordance with naïve expectations: p/π^+ (\bar{p}/π^-) ratio is higher (lower) at forward rapidity than at mid-rapidity due to increasing content of the primordial baryons in the fragmentation region at $\eta \approx 3.2$.

2.6.7. Jet suppression

In elementary collisions at high energy jets of hadrons flying in opposite directions had been observed. At the initial stage of the collision an energetic pair of quark-antiquark (or gluon-gluon) is sometimes created in a hard scattering process as presented in Figure 2.20. Those fast partons, being a color objects, have to fragment into hadrons on leaving the interaction region. Experimentally observed are two groups of high-momenta hadrons moving co-axially in opposite directions. It

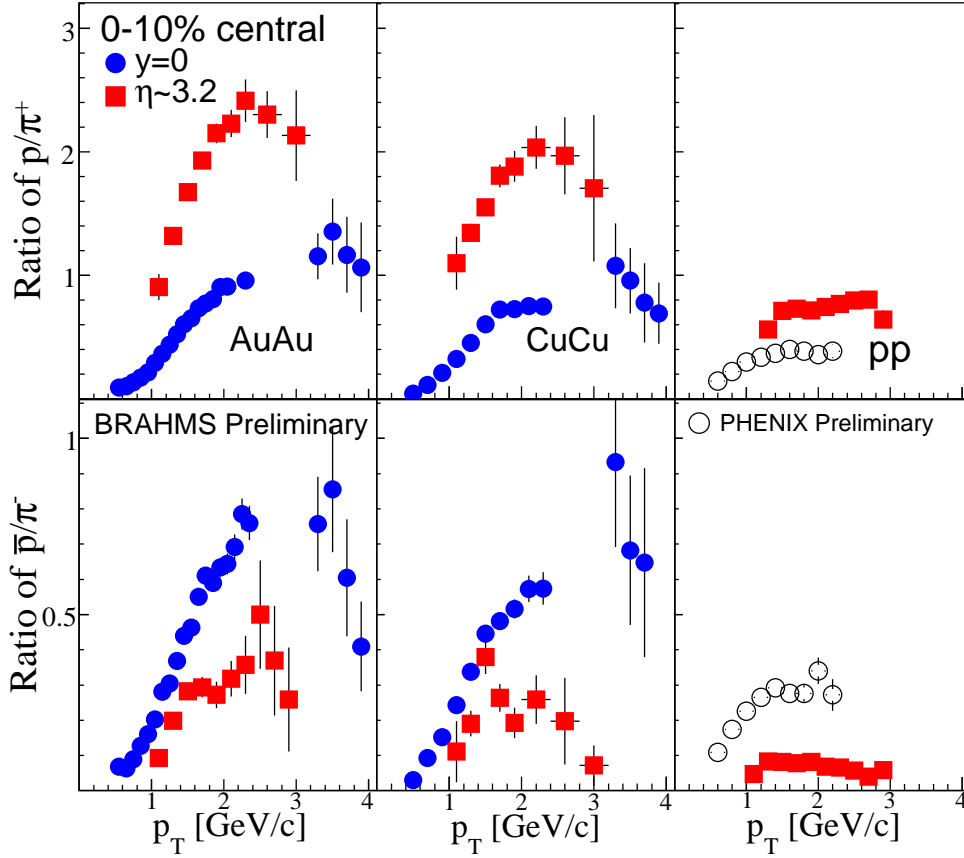


Figure 2.19. p/π^+ (\bar{p}/π^-) ratio as a function of p_T for different colliding systems at $\sqrt{s_{NN}} = 200$ GeV presented in top (bottom) panels. Right panels present ratios in Au + Au, middle in Cu + Cu and left in p + p collisions at mid-rapidity (blue circles) and forward rapidity of $\eta \approx 3.2$ (red squares). Figure taken from [89].

has been proposed that in heavy ion collisions, if QGP medium is created, the partons traversing this medium will experience huge energy loss, much greater than if they moved in hadron gas only. Expected effect is called jet quenching and there are two generally accepted methods to observe it.

1. **Azimuthal correlation.** In each event a particle (trigger particle) with the largest transverse momentum is selected. Assuming this particle is the leading particle of one jet it is important to study the azimuthal correlation of the associated particle production. This method requires a detector with

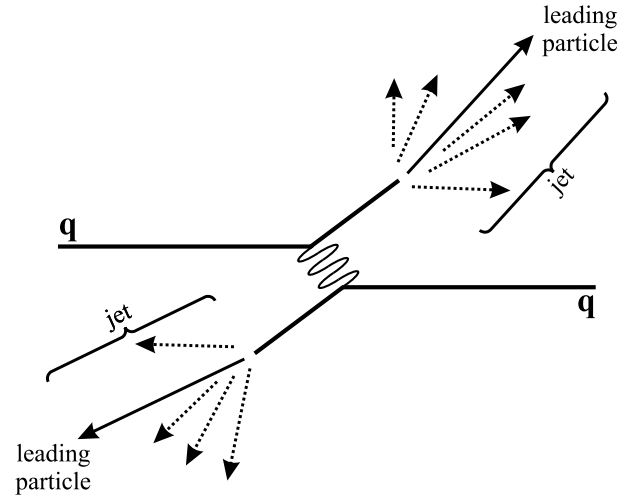


Figure 2.20. Schematic illustration of jet creation in hard quark-quark collision. Scattered partons hadronize into group of hadrons, called jets. The hadron carrying the largest fraction of scattered parton momentum is referred to as the leading particle.

large acceptance, hence BRAHMS experiment is unable of such measurements with the present detectors' layout. Results obtained by the STAR Collaboration [90,91] show that structure of the jets depends on the colliding system, centrality, momenta of the triggering and associated particles. Figure 2.21 shows azimuthal distribution of particles in reference to the triggering hadron. Going from left to right different panels show associated particle distributions for increasing transverse momentum of the triggering particle. The two bins in transverse momenta of associated particles are shown in top and bottom rows of the figure. The figure documents the emergence of the two opposite jets structure as the triggering momentum increases. The dependence of the jet structure on system size is shown in Figure 2.22. The figure shows the near-side (at $\Delta\phi \approx 0$) and away-side (at $\Delta\phi \approx \pi$) particle yields for different values of p_T^{trig} as a function of the number of participants. While the yield of the near-side peak does not change with centrality, the away-side peak decreases with increasing centrality.

The results obtained by STAR and PHENIX [92] strongly support the idea

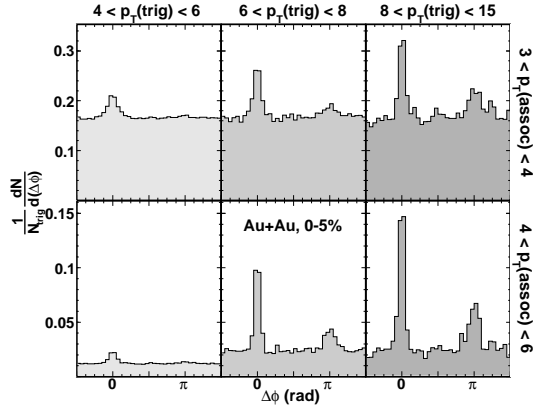


Figure 2.21. STAR Collaboration results [91] on azimuthal correlations of charged particles in 0 – 5% central Au + Au collisions at $\sqrt{s_{NN}} = 200$ GeV. Different transverse momentum ranges for the trigger particle are shown in left, middle and right panels. Top row shows associated particles with $3 < p_T^{assoc} < 4$ GeV/c and bottom with $4 < p_T^{assoc} < 6$ GeV/c. The p_T values indicated on the plot are in units of GeV/c.

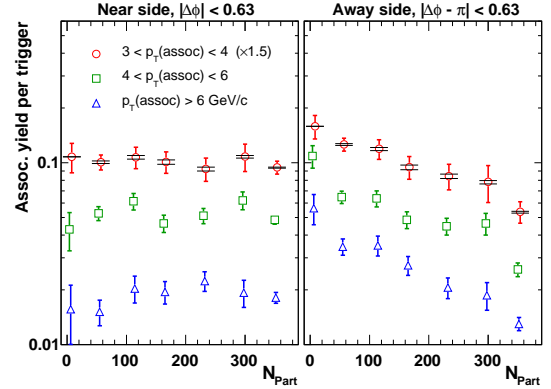


Figure 2.22. STAR Collaboration results [91] on centrality dependence of near- (left panel) and away-side (right panel) peak yields in Au + Au collisions at $\sqrt{s_{NN}} = 200$ GeV. The results are for the $8 < p_T^{trig} < 15$ GeV/c and three different bins of the associated particle transverse momenta has been shown. The left-most points in the two panels are obtained from the minimum bias d + Au collisions. The p_T values indicated on the plot are in units of GeV/c. For clarity $3 < p_T^{assoc} < 4$ GeV/c are scaled by 1.5. The errors bars are statistical, for the $3 < p_T^{assoc} < 4$ GeV/c the horizontal bars show the systematic uncertainty on background suppression, which is negligible for higher p_T s.

of the partonic in-medium energy loss. It is argued that the trigger particle belongs to the jet that was produced relatively close to the outer layer of the medium, and thus experience small energy loss, independent of the centrality.

The away-side peak shows that the opposite jet loses energy that strongly increases with the length of matter traversed.

2. **Nuclear modification factor (R_{AA}) studies.** Since R_{AA} is the main subject of the work, it will be thoroughly described in Chapter 3. At this point it is enough to say that another way of detecting in-medium jet modification is to compare the high- p_T particle production in heavy ion collisions with that from elementary collisions. From the collisions at lower energies it has been concluded that particle production at large transverse momenta, where particles are produced in initial hard scatterings, scale with the number of binary collisions. Deviations from this expected scaling observed by at RHIC (see next Chapter) suggest influence of the created medium on observed particle yields.

3 Nuclear modification factor

3.1. Definition

Nobody doubts in the statement that heavy ion collisions are not simple superposition of some number of nucleon-nucleon collisions. Initial parton distribution must be influenced by a nucleus environment. Nucleons from one nucleus do not collide with only one nucleon from the other, but rather interact with several on its way through the nucleus. Produced high- p_T particles are not moving in vacuum, as in $p + p$ reactions, but in a strongly interacting medium. Nevertheless, heavy ion collisions obey, at least up to some colliding energy, several simple scaling laws. The total particle yield must follow the total energy available for particle production, which scales at given collision energy with the number of particles involved in reaction. Therefore the bulk particle production in reactions even at RHIC scales at given beam energy with the number of participants [93,94]. High energy jets are produced in hard scattering processes at the initial stage of the collision with a relatively small cross section. Thus the probabilities of jet production in several collisions experienced by a parton on traversing another nucleus add and therefore jet production scales with the number of binary collisions [95]. This scaling has been observed up to energies available at the SPS [96].

Nuclear modification factor (R_{AA}) is constructed to be a measure of jet modifications in nuclear medium and is defined as:

$$R_{AA}(y, p_T) = \frac{1}{\langle N_{coll} \rangle} \frac{\frac{d^2 N_{AA}}{dp_T dy}}{\frac{d^2 N_{pp}}{dp_T dy}}, \quad (3.1)$$

where $\frac{d^2 N_{AA}}{dp_T dy}$ and $\frac{d^2 N_{pp}}{dp_T dy}$ is the particle production in $A + A$ and $p + p$ collisions respectively, in a given rapidity and transverse momentum bin. $\langle N_{coll} \rangle$ is the average number of binary collisions in the heavy ion collision.

Particle production by energetic jets is a dominant source of particle yield at large transverse momenta, generally above 2 GeV/ c , and it is in this region that we expect

the R_{AA} to be consistent with unity, if there are no nuclear modifications. At the lower momenta particle production should scale with the number of participants, and therefore nuclear modification factor converge to N_{part}/N_{coll} , which is about 1/3 in central Au + Au reactions. Expected dependence of R_{AA} in case of no nuclear modifications is shown in figure 3.1.

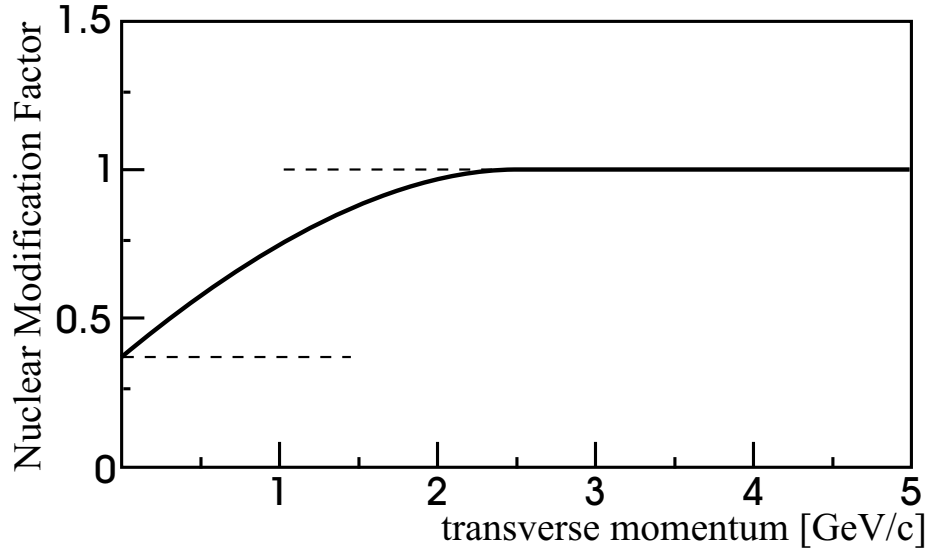


Figure 3.1. Expected behavior of nuclear modification factor, R_{AA} .

Sometimes, due to lack of appropriate p + p data, which enables to calculate R_{AA} , a ratio of central to peripheral spectra is used (R_{cp}), on the premise that ultra-peripheral events look very like elementary collisions. Although this quantity is also referred to as the nuclear modification factor, it is affected by remnants of nuclear effects in peripheral events. It is defined as:

$$R_{cp}(y, p_T) = \frac{\frac{1}{\langle N_{coll} \rangle_{central}} \frac{d^2 N_{AA}}{dp_T dy} |_{central}}{\frac{1}{\langle N_{coll} \rangle_{peripheral}} \frac{d^2 N_{AA}}{dp_T dy} |_{peripheral}}. \quad (3.2)$$

3.2. Nuclear modification factor at SPS

Results obtained by SPS experiments [96,97], reveal unexpected enhancement of R_{AA} around $p_T \approx 2 \text{ GeV}/c$. This observation was explained in terms of a phenomenon called Cronin enhancement [98]. It is argued, that the quarks of the colliding nuclei experience multiple scatterings which results in broadening of the initial parton transverse momenta (k_T broadening). This causes enhancement of particle production at $p_T \approx 2 \text{ GeV}/c$.

WA98 Collaboration in [96] announced that in central Pb + Pb collisions at the top SPS energy, R_{cp} at high p_T is smaller than predicted by models. The observation however is inconclusive, since no suppression is observed for R_{AA} .

3.3. Nuclear modification factor at RHIC

Experimental data gathered at RHIC opened a possibility of comparing R_{AA} for various energies and colliding systems in a new energy domain, where strong in-medium effects are expected. First evidence of particle suppression has been observed at $\sqrt{s_{NN}} = 130 \text{ GeV}$ in Au + Au collisions at RHIC by STAR [99] and PHENIX [100] for unidentified hadrons. The first results from BRAHMS experiment [101] confirmed the strong particle production suppression above $3 \text{ GeV}/c$ in Au + Au collisions at $\sqrt{s_{NN}} = 200 \text{ GeV}$, as presented in Figure 3.2.

This is interpreted as the jet quenching in a strongly interacting medium created just after the collision, which is usually identified as the QGP. Interesting fact is that for the transverse momenta around $2 \text{ GeV}/c$ there is a peak in the R_{AA} , which can be identified as remnants of the initial Cronin effect [98].

At this point it is necessary to validate expected scaling of R_{AA} with the number of binary collisions. PHENIX Collaboration presented nuclear modification factor [103,104] for direct photons, which are not expected to experience any in-medium modifications. Consistency of the photons' R_{AA} with unity, shown in Figure 3.3, confirms scaling with N_{coll} .

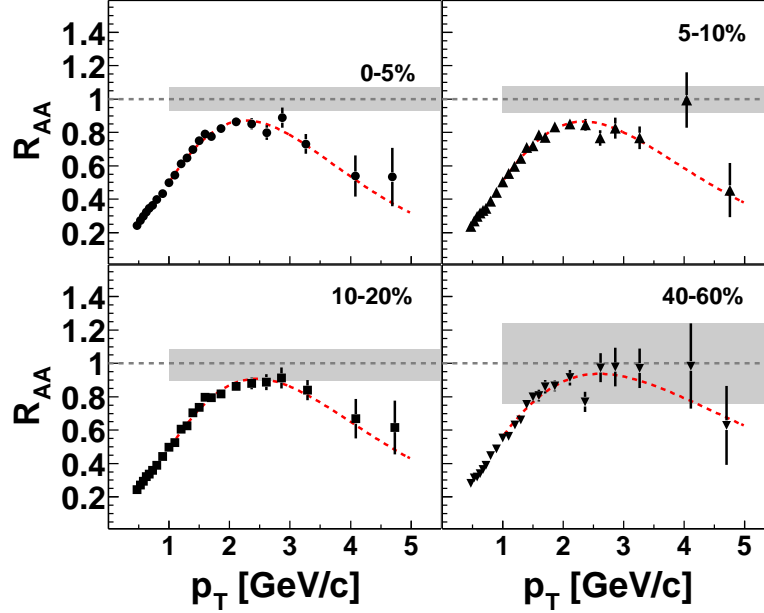


Figure 3.2. Nuclear modification factor for unidentified hadrons in $Au + Au$ central collisions at $\sqrt{s_{NN}} = 200$ GeV for different centrality classes [101]. The dashed lines indicates the ratio of the fits to the data and the reference data. The gray areas indicate the uncertainty of the $\langle N_{coll} \rangle$ scaling. $p + p$ reference spectra was taken from UA1 experiment [102].

3.3.1. Energy dependence

BRAHMS experiment has measured [105] nuclear modifications factors for $Au + Au$ collisions at $\sqrt{s_{NN}} = 62.4$ and 200 GeV. Comparison of R_{AA} at the two energies is presented in Figure 3.4. No suppression is observed in BRAHMS mid-rapidity data at smaller energies, due to limited transverse momentum acceptance. The consistency of R_{AA} with unity observed around $p_T \approx 2$ GeV/ c is accidental, and caused by the remnants of Cronin effect also seen in $\sqrt{s_{NN}} = 200$ GeV data. Other experiments [107] observe that suppression appears also for this lower collision en-

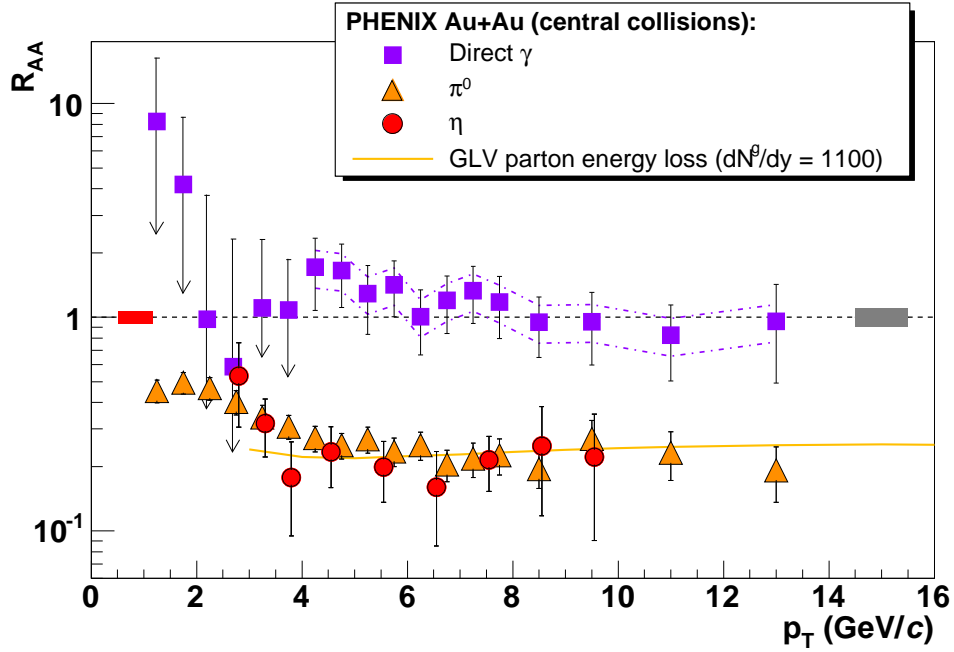


Figure 3.3. Comparison of the nuclear modification factor for direct photons, π^0 and η measured by PHENIX Collaboration [104] in Au + Au collisions at $\sqrt{s_{NN}} = 200$ GeV.

ergy at higher p_T . For central events the R_{AA} decreases to eventually level out at $p_T \approx 6$ GeV/c. The suppression factor for $\sqrt{s_{NN}} = 62.4$ GeV seems to be very similar to that at $\sqrt{s_{NN}} = 200$ GeV in the high transverse momenta region.

3.3.2. Fireball size dependence

Another interesting dependency of R_{AA} is the dependency on the size of the created fireball. There are two ways of modifying the fireball volume, either by selecting the collision centrality or by changing the colliding nuclei.

1. **Centrality dependence.** Dependence of R_{AA} on centrality [105] in Au + Au collisions at $\sqrt{s_{NN}} = 200$ GeV is presented in Figure 3.5. In central events strong suppression is observed, and R_{AA} is about 1/3 at high p_T . Particle production in peripheral collisions scales with N_{coll} (for centralities 40 – 60%).

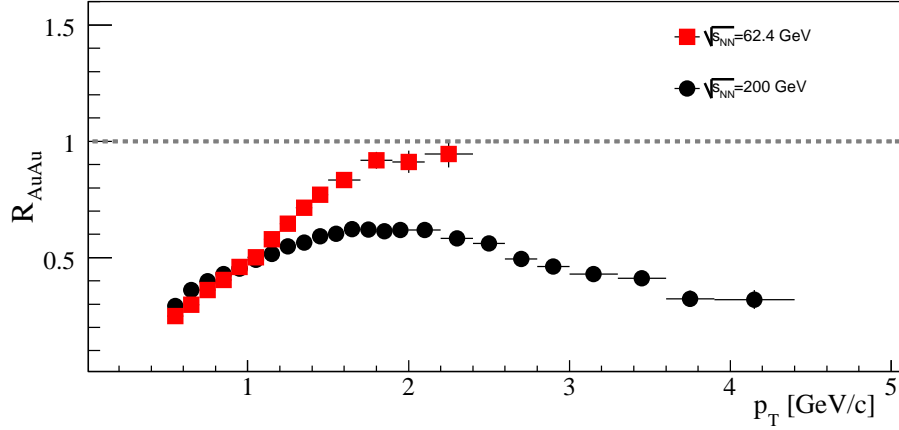


Figure 3.4. R_{AA} for unidentified particles measured at $\eta \approx 0$ for Au + Au at $\sqrt{s_{NN}} = 62.4$ and 200 GeV for the most central collisions [105] ($p + p$ reference is based on ISR collider data [106]).

The results are compatible with simple expectations, that in the more central events the distance for the particle to travel through the dense medium is longer.

2. **System dependence.** Figure 3.6 presents nuclear modification factors [105] as a function of centrality for Au + Au and Cu + Cu collisions at $\sqrt{s_{NN}} = 62.4$ GeV. For Cu + Cu collisions no suppression at all is observed - Cronin peak is already visible for the most central events. The results for the two systems at the same centrality classes are very different - R_{AA} is larger for the smaller system.

In Figure 3.7 these two dependencies have been summarized in one plot. In the region above $p_T \approx 5$ GeV/ c , where the nuclear modification factors do not change with transverse momenta, R_{AA} has been integrated and plotted versus number of participants. The data used in this plot are for identified π^0 taken by PHENIX experiment [108] in Au + Au and Cu + Cu collisions at $\sqrt{s_{NN}} = 200$ GeV. As expected, strong correlation is observed, namely the nuclear modification factor

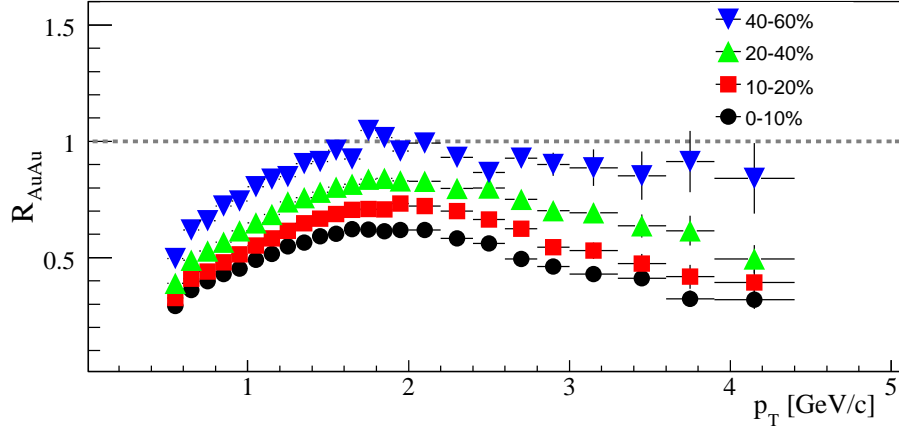


Figure 3.5. R_{AA} for unidentified particles measured at $\eta \approx 0$ for Au + Au collisions at $\sqrt{s_{NN}} = 200$ GeV for different centrality classes indicated on the plot [105] (p + p reference is based on ISR collider data [106]).

depends strongly on the size of the fireball. This suggests that similar number of participants forms similar size and density of the fireball. Consequently similar modification of energetic jets is observed.

3.3.3. Rapidity dependence

The rapidity dependence of the nuclear modification factor is the main subject of this work and the new results obtained by the author will be presented in Chapter 5. Early results of the BRAHMS experiment [109] are shown in Figure 3.8. Almost no dependence on rapidity is observed. It appears that the suppression is even stronger at forward rapidity than at mid-rapidity [109].

3.3.4. Identified particles

The modification factors for identified hadrons reveal an unexpected and fascinating feature. There is huge discrepancy in the shape of nuclear modification factors for mesons and for baryons. Left panel of Figure 3.9 shows R_{AA} for mesons (kaons and ϕ 's) and right panel shows R_{AA} for identified protons, Λ 's and Ξ 's, as measured by STAR experiment [110]. While nuclear modification factor for all the

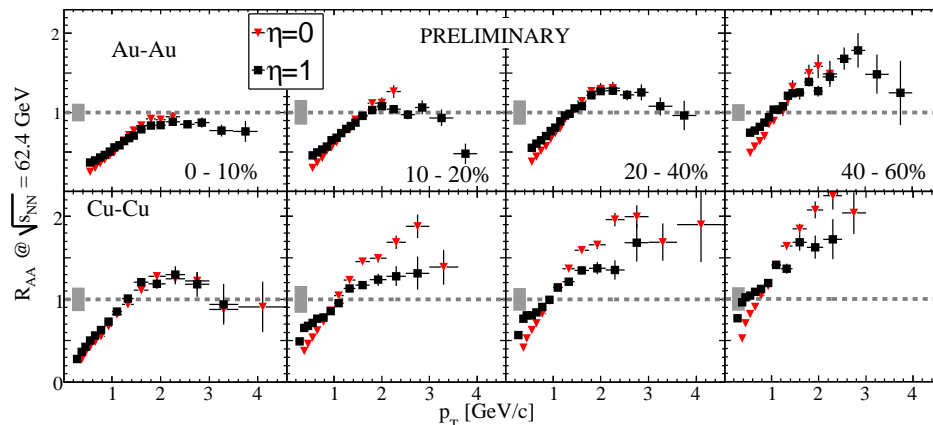


Figure 3.6. R_{AA} for unidentified particles measured at pseudo-rapidities $\eta \approx 0$ and $\eta \approx 1$ for Au + Au (upper row) and for Cu + Cu (bottom row) systems at $\sqrt{s_{NN}} = 62.4$ GeV for different centrality classes indicated on the plot [105] (p + p reference is based on ISR collider data [106]).

mesons lies below unity, baryons experience a significant enhancement in the region $1 \lesssim p_T \lesssim 5$ GeV/ c . This is clearly an effect of the observed baryon enhancement in the Au + Au collisions at the top RHIC energy (see section 2.6.6).

High p_T PHENIX data on suppression for light mesons (π^0 and η), where $R_{AA} \approx 0.2$, suggests similar mechanisms of energy loss. Although STAR data does not reach to that high transverse momenta, their results suggest decrease of the nuclear modification factor above $p_T \approx 3$ GeV/ c . R_{AA} for kaons and ϕ s seems also to converge to 0.2 in the highest p_T bins. It is still unclear if the baryons also experience quenching at similar level, but the data show that R_{AA} decreases in the high transverse momenta region. STAR [110] also points at apparent scaling of nuclear modification factors in the medium p_T region with strange quark content. Ξ hyperons with two strange quarks are more enhanced than Λ hyperons with only one s quark, while protons with no strange quark are even less enhanced. It seems to be confirmed for the mesons particles, since pions and η mesons, with no s quark, experience more quenching in that region than mesons with one strange quark (kaons

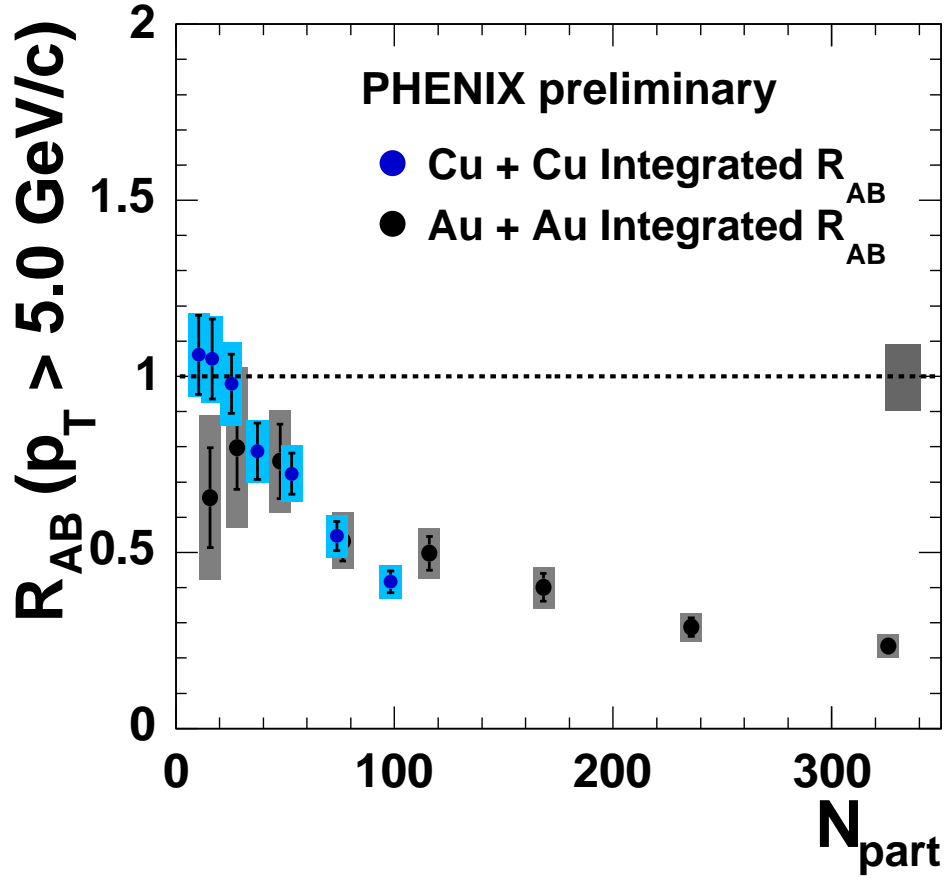


Figure 3.7. Integrated R_{AA} for Au + Au and Cu + Cu collisions at $\sqrt{s_{NN}} = 200$ GeV measured by PHENIX as a function of N_{part} [108].

and ϕ).

3.3.5. d + Au collisions

Even before observation of jet quenching physicists disputed whether the expected suppression would be caused by initial or final state effect. It has been proposed that the discussion might be settled by measurement of nuclear modification factor in d + Au collisions, where no creation of dense medium is expected. Results obtained by BRAHMS [109] on R_{dAu} show no suppression in the mid-rapidity region (see Figure 3.10) but rather a Cronin type enhancement is observed.

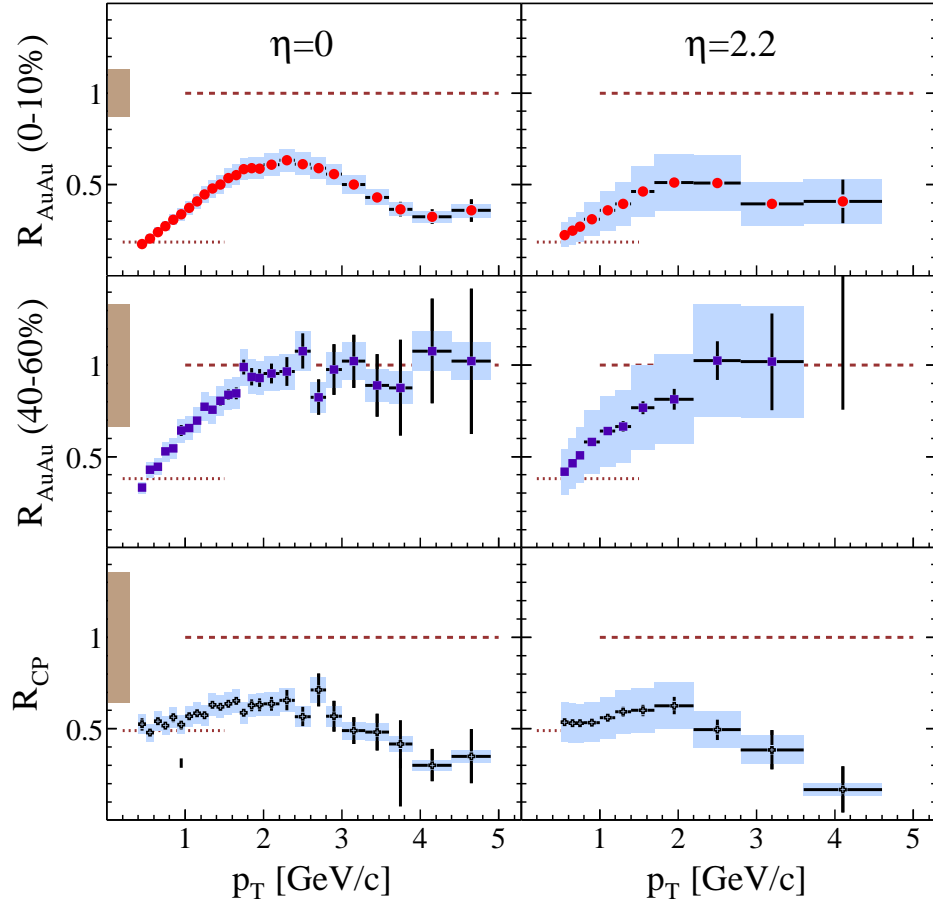


Figure 3.8. Rapidity dependence of the nuclear modification factor for unidentified hadrons in the BRAHMS experiment [109] in Au + Au collisions at $\sqrt{s_{NN}} = 200$ GeV.

This strongly favors the scenario of jet quenching in the dense medium created in Au + Au collisions opposite to interpretations basing on initial state effects, like gluon saturation [67].

BRAHMS collaboration has also reported [111] on rapidity evolution of R_{dAu} . The measurements reveal decrease of the nuclear modification factor with increasing rapidity as presented in Figure 3.11. It suggests that particle production in the

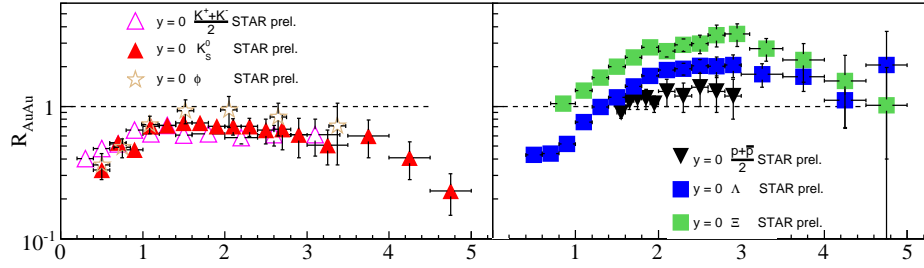


Figure 3.9. Preliminary STAR results [110] on nuclear modification factors in central (0 – 5%) Au + Au collisions at $\sqrt{s_{NN}} = 200$ GeV for mesons (left panel) and baryons (right). For comparison inclusive charged hadrons R_{AA} is presented as a dotted line.

forward rapidity region is quenched due to the initial gluon saturation [67].

3.4. Theoretical interpretation

High energy partons produced in p + p collisions move and fragment into jets of hadrons in the vacuum, as schematically shown in Figure 2.20. The fragmentation process is described by the Dokshitzer-Gribov-Lipatov-Altarelli-Parisi (DGLAP) [114] QCD evolution equations. In as early as 1982 Bjorken [115] predicted that jets moving in a dense medium would experience elastic energy loss. Soon it was realized that jet quenching would be rather triggered by induced gluon radiation and brehmstrahlung. The results at RHIC confirm the scenario of the in-medium jet suppression and thus the following sections will summarize various theoretical approaches to this problem.

3.4.1. Multiple parton scattering

The model of jet quenching created by Gyulassy, Levai and Vitev (GLV) [116, 117] was the only one to predict the level of suppression as well as flatness of R_{AA} at high p_T . In this approach authors calculate the energy loss of the jet parton by gluon radiation in multiple scatterings on the color charges in medium. The non-

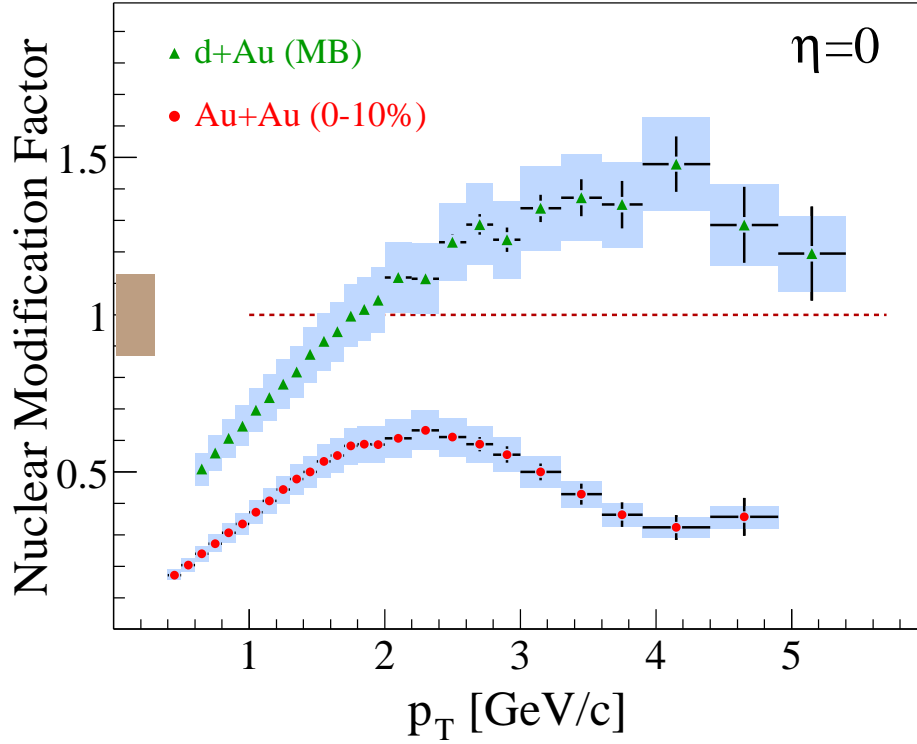


Figure 3.10. BRAHMS experiment results [109] on nuclear modification factor for unidentified hadrons measured for minimum bias d + Au collisions at $\sqrt{s_{NN}} = 200$ GeV compared to central Au + Au collisions. The gray band at $p_T = 0$ is the uncertainty on the scale of R_{AuAu} .

Abelian character of the interactions is taken into account by inclusion of Landau-Pomeranchuk-Migdal (LPM) interference effects [118]. The energy loss modifies the momentum of the jet's leading hadron in the fragmentation functions used in DGLAP [114] QCD evolution equations. Parton energy loss in the dense medium, dE , depends on several quantities, like medium density, initial parton energy and length of matter traversed by the parton. In GLV model [117] the energy loss depends on the initial parton energy like $\log(E)/E$, and grows with the medium size L like L^2 due to long range interferences between color charges. The linear propor-

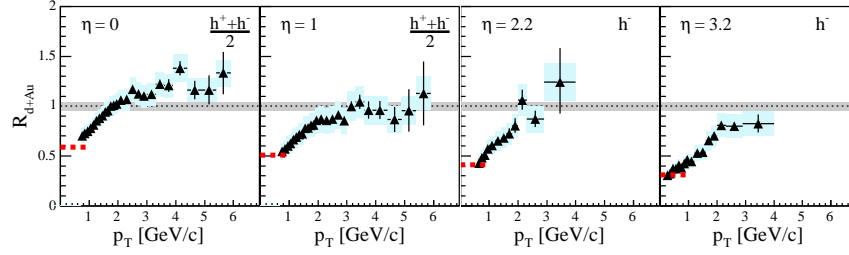


Figure 3.11. Nuclear modification factor for charged hadrons measured in central $d + Au$ collisions at pseudo-rapidities $\eta = 0, 1, 2.2, 3.2$ [111].

tionality of dE to the medium density and the rapid decrease of the density in heavy ion collisions with time, softens the mentioned dependencies. Complex calculations show that dE is proportional to E , and grows faster than linearly, but slower than quadratically, with L . Authors also calculate the initial gluon density (at time $\tau = 0.2 \text{ fm}/c$), which is about $dn_g/dy \approx 1000 \pm 200$.

In the GLV approach the authors [132] explain the baryon to meson enhancement with a novel baryon transport dynamics in nucleus-nucleus collisions [133]. In their model slope of the Regge trajectory controls hadron transport for small transverse momenta. This suggests that the baryon production should be enhanced compared to meson production as $\sqrt{3} : \sqrt{2}$.

3.4.2. Twist expansion

Wang in his works [119,120] uses higher-twist matrix elements for $e + A$ collisions in rescattering on the hit quark in the nucleus. Starting from computing modifications in cold nuclear matter (in $e + A$ collisions from HERMES DIS data) he introduces the energy loss into modified DGLAP equations in $Au + Au$ collision. The results indicate that the initial gluon density at $\sqrt{s_{NN}} = 200 \text{ GeV}$ is larger than in Au nucleus by a factor of about 30 [120–122]. In his model the energy loss initially at time $\tau = 0.2 \text{ fm}/c$ reaches value $dE/dx|_0 = 13.8 \pm 3.9 \text{ GeV}/\text{fm}$, but due to density decrease the average energy loss is about $dE/dx \approx 1 \text{ GeV}/\text{fm}$.

3.4.3. Surface emission

Dainese with his collaborators [123] developed a Parton Quenching Model (PQM) which bases on the pQCD framework for calculation of parton energy loss in multiple elastic scatterings, developed by Baier, Dokshitzer, Mueller, Peigné, and Schiff [124]; Zakharov [125]; Salgado and Wiedeman [126]; referred to as BDMPS-Z-SW framework. In their model the soft medium which quenches the jet production is simulated using Wood-Saxon density profiles. The results indicate that the dense medium created in the collision is too thick for partons to pass. Thus only the partons produced in the thin surface layer (about 1.7 fm) of the hot and dense medium escape experiencing relatively small energy loss of less than 0.3 GeV/fm.

Similar approach to that presented by Dainese [123] has been used by Eskola [127]. In their model the low p_T part is obtained assuming saturation of final state gluon distribution, which then expands and cools down hydrodynamically. The high p_T jets are simulated using pQCD parton-parton cross sections, and energy loss is applied to the fragmentation functions. The nucleus density profile is obtained using Wood-Saxon profile.

3.4.4. Hydrodynamic model

Hirano and Nara [128,129] use their model of 3D hydrodynamical model for simulating the dense medium. Parton production in hard scatterings as well as its fragmentation is simulated using PYTHIA [130] model. In their recent works they assume parton energy loss in the GLV [117] mechanism. The special feature of their model is the easiness of calculations at various rapidities, as presented in Ref. [129].

3.4.5. Recombination

Different from the GLV and Wang models, the recombination model by Hwa [131] does not try to evaluate the in-medium energy loss. Authors are postulating that the hadron transverse momentum spectrum results from two overlying quark distributions: thermal source with exponential decrease in p_T with a given temperature, and a power law distribution of shower quarks from energetic jets. Quarks from the two distributions recombine to create hadrons. In this approach pion transverse momentum distributions are fitted to obtain the two mentioned quark distributions. Then other hadron spectra are calculated. This model shows that in the medium

p_T region ($2 < p_T < 5$ GeV/ c) the contribution of hadrons composed of thermal (T) and shower (S) quarks is particularly important. The observed enhancement of baryon to meson ratio in this p_T region is a straightforward output of the model. It is claimed by the authors that the recombination may also be parametrized in the parton fragmentation approach.

3.4.6. CGC

The influence of initial state effects like Color Glass Condensate (see section 2.5.2) on mid-rapidity jet quenching in Au + Au collisions at RHIC has been excluded by lack of suppression in d + Au collisions. However, CGC is probably responsible for jet quenching in the forward rapidity region of Au + Au collisions. It is argued that the saturation of gluon densities at small x results in smaller parton production in hard scatterings, and thus suppresses the nuclear modification factor.

3.4.7. Summary

Experimental results on nuclear modification factors in Au + Au, Cu + Cu and d + Au collisions at RHIC indicate that the jet quenching should be attributed to the final state effects solely, at least in the mid-rapidity region. The quenching of the jets is proportional to the density of the dispersing medium, which is usually identified with the strongly interacting Quark-Gluon Plasma (QGP). The long range interferences also influence the suppression. It is even possible that the inner core is completely opaque to the jet propagation, and the jet emission is dominated by the production in the surface. It is still unclear whether the hadronization is due to fragmentation processes as in the vacuum, or rather quark recombination in the dense medium.

4 Data analysis chain

4.1. Introduction

The Forward Spectrometer arm was schematically presented in section 2.4 (for detailed description see [61]). It is a very powerful tool to study the transverse momenta distributions of charged hadrons. It was designed to trace and identify particles up to very high momenta. The cost of this wide momentum range is relatively small acceptance of 0.8 milisteradians that has to be properly accounted for in data analysis. Corrections to acceptance, in-flight decays, absorption, multiple scattering and efficiency are large and it is of great importance to determine these corrections with a high precision. In this chapter I will present particle tracking and identification as well as various corrections applied to the data. It is however essential to start with the global event characteristics, namely vertex position and centrality.

4.2. Event characteristics

4.2.1. Vertex position

One of the colliders' drawbacks in comparison with simple accelerators is lack of fixed target and consequently problems with determination of the position of the collision vertex. Colliding beams are of finite transverse dimensions and when crossing, they form an interaction region of considerable length (about 1 meter), as schematically depicted in Figure 4.1. Most of the collisions are randomly taking place in this region, referred to as the nominal interaction region. To determine the vertex position a set of global detectors is used: ZDC, BB and in the case of $p + p$ collisions also CC (see Figure 2.2). ZDCs are sensitive to the spectator neutrons, whereas BB and CC to charged particles produced in the fragmentation region, for nucleus-nucleus and $p + p$ collisions, respectively.

They are placed symmetrically on both sides of the nominal interaction region



Figure 4.1. Interaction region in RHIC experiments.

along the beam pipe, and measure the time difference between arriving particles. This can be translated into position of the vertex along the beam axis. Results from these global detectors can be verified by more sophisticated measurements using tracks of particles emitted at mid-rapidity. Comparison of the vertex position determined by BB with the one obtained from the track extrapolation to the interaction region is shown in Figure 4.2. Results indicate that BB vertex resolution is $\sigma_{BB} = 0.7$ cm. Similar analysis for ZDC and CC give resolutions of $\sigma_{ZDC} = 2.8$ cm and $\sigma_{CC} = 0.7$ cm, respectively.

4.2.2. Centrality determination

Precise determination of the vertex position is crucial for good centrality measurements, since Multiplicity Arrays (see section 2.4 and Figure 2.2) acceptance depends on the vertex position [134]. A large number of charged particles is produced in nucleus-nucleus collisions at RHIC energies. It is very trivial to note that the more central the event is the more particles should be created in the collision. Thus the multiplicity is the measure of centrality. Figure 4.3 presents the multiplicity distribution determined with use of the MA in Au + Au reactions at $\sqrt{s_{NN}} = 200$ GeV, with the division showing centrality determination.

4.3. Particle Tracking

The construction of the yield in the BRAHMS experiment consists of several stages that shall be presented in this section.

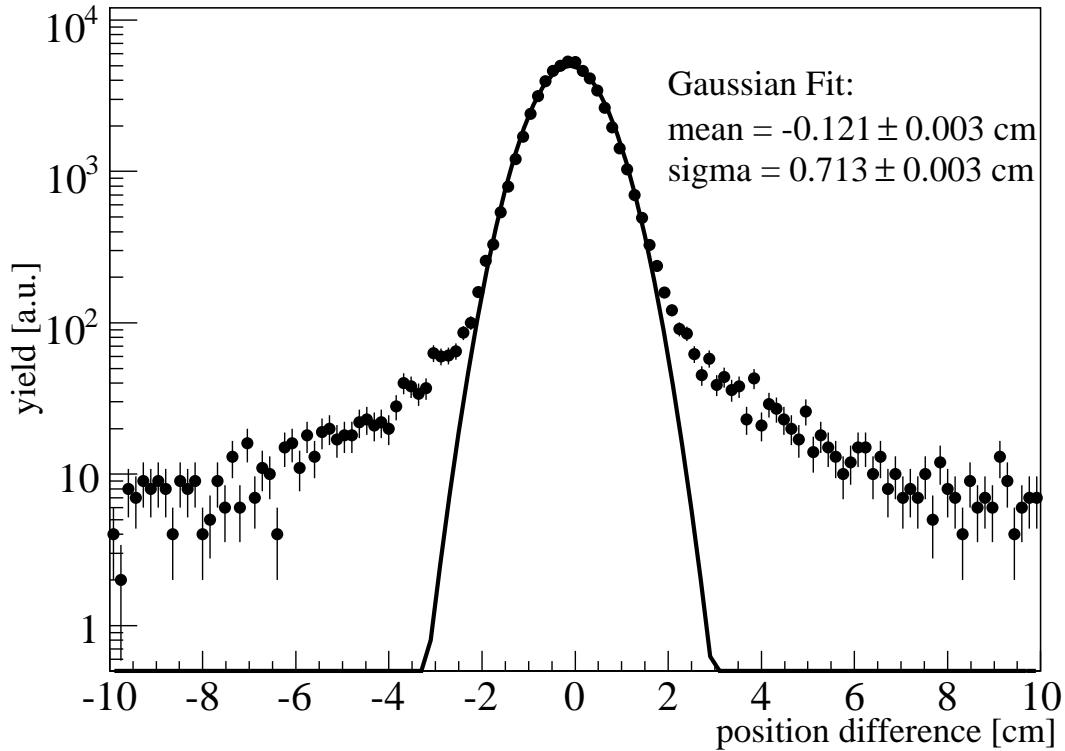


Figure 4.2. Difference in position between BB vertex and TPM1 vertex.

4.3.1. Local tracking

Local tracking bases on information from tracking detectors and produces parameterization of the detected particle trajectories. Due to difference in tracking for time projections chambers (TPC) and drift chambers (DC) local tracking has to be discussed separately for this two kinds of detectors.

4.3.1.1. TPC

Generally tracking detectors utilize the fact of a gas ionization by moving charged particles. In TPCs, electrons created along the particle trajectory move upwards toward anode wires in a constant electric field (+1200V), as schematically presented in Figure 4.4. In the last stage of the drift, beyond the cathode wires, they are accelerated by strong anode field and create the ionization shower. The ionized electrons are collected by the anode wires, whereas the positively ions are collected

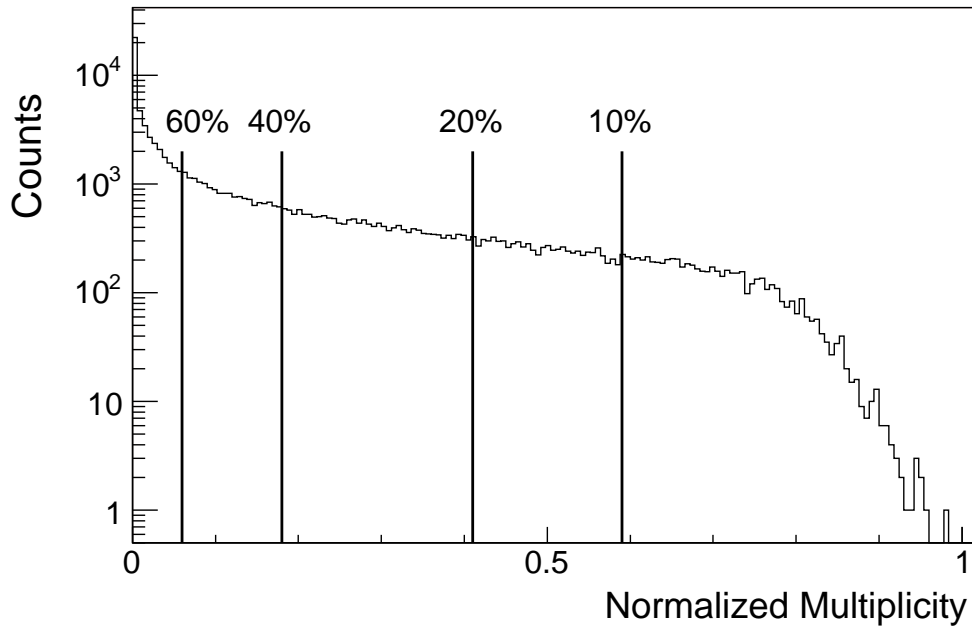


Figure 4.3. MA multiplicity distribution. Lines show the limits for indicated centralities.

by active pads that are spanned just behind the anode wires.

The signal output from a pad delivers time and the collected charge information. Assuming constant drift velocity the time information is translated into distance of the particle trajectory to the active pad whereas the charge information is used for the noise discrimination. Since usually more than one pad is activated by the shower, the amplitude information from adjacent pads is used to determine the position of the hit along the pad array. Therefore TPCs signal contains 3-dimensional information about hit position. The information from the full set of pad arrays provides 3D information about particle trajectory and the TPC tracking bases on the procedure that combines hits to form the straight lines. For more information see [135].

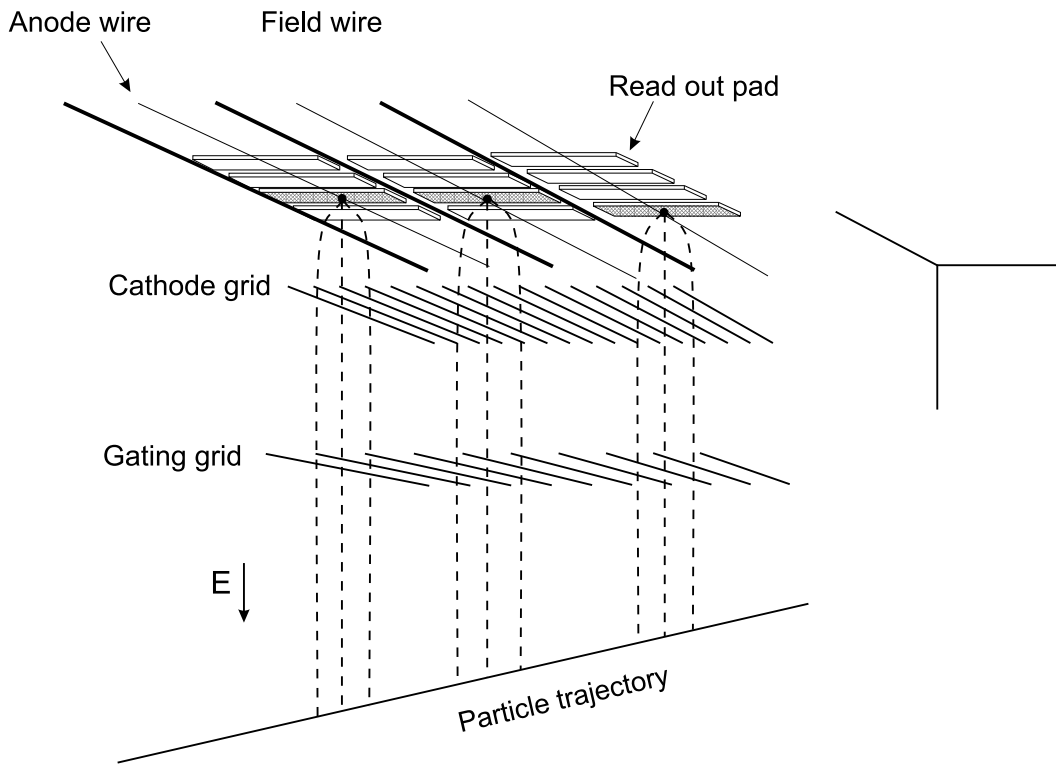


Figure 4.4. Schematic picture of the TPC readout plane and electron drift lines.

4.3.1.2. DC

The basic idea of the drift chamber is ionization of a gas by fast-moving charged particles. In the DCs thus created ions move in a strong electric field present inside the chamber. The field is shaped by a positively charged wire (anode wire) with a potential of about +1000V placed in the center and several more (typically 8) wires (cathode and field wires) placed around on the edges of a detecting cell with a potential of about -1000V, as shown in Figure 4.5. The ionized electrons that move towards anode wire are responsible for signal detecting, while slowly moving positive ions are collected by cathode/field wires. Anode and cathode wires are grouped into detecting planes.

DCs consist of three identical modules. Each module is a set of detecting planes (8 in case of T4 and T5, and 10 for T3), oriented in four different directions, also called views. The wires are vertical in the first two (three for T3) planes (X) (thus

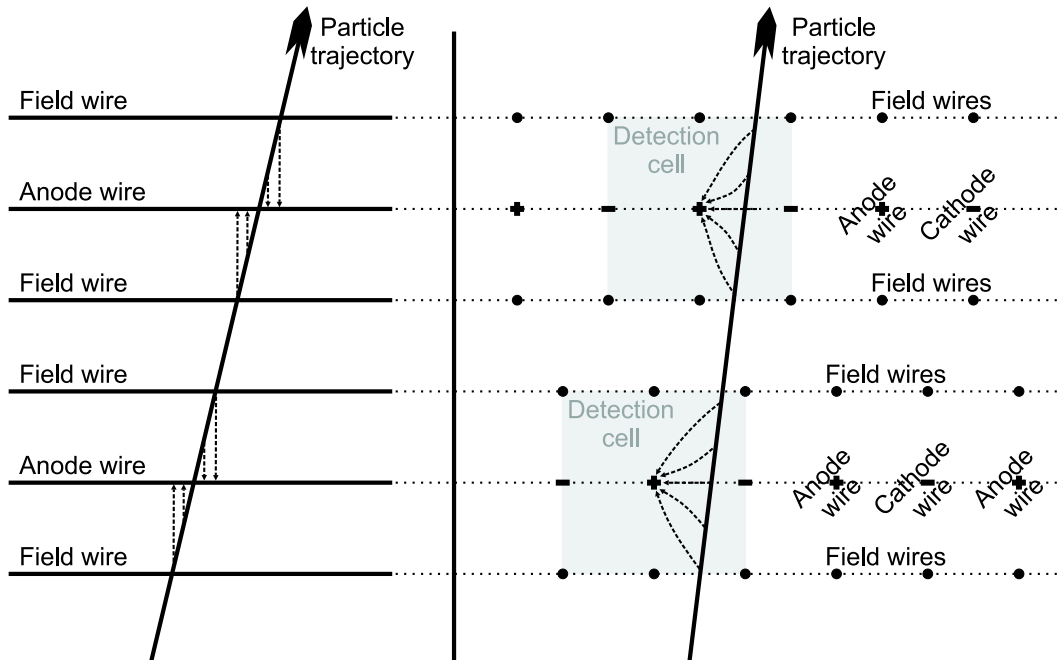


Figure 4.5. Schematic picture of DC wires layout.

detecting horizontal position of the particle track), horizontal in the two (three in T3) next planes (Y), rotated by $+18^\circ$ from vertical in the two next planes (U), and rotated by -18° from vertical in the last two planes (V). The second plane in each view is always shifted by quarter of a cell width in respect to the first one.

The ionized electrons in the gas move towards the anode wire with a certain drift velocity (typical of few centimeters per microsecond), while the signal inside the wire move with much greater speed close to the speed of light. Thus the time of the signal give information about the distance the ionized electrons traveled inside the gas and, consequently, about the distance of the particle trajectory to the anode wire. The signal does not therefore give a full three-dimensional point through which a particle traveled and information from different detection planes has to be compiled to calculate the particle trajectory. Various reconstruction problems and their solutions are presented in [136,137].

The design of DCs results in an excellent one-hit resolution of $95\mu\text{m}$ and $110\mu\text{m}$, with efficiency of 99% and 99%, in T4 and T5, respectively. The observed discrep-

ancy in performance of T4 and T5 is caused by much larger background in the latter detector. This problem of worse performance of the drift chambers in high multiplicity environment is known and is even more clearly apparent in the case of T3 detector where one hit resolution drops to $120\mu\text{m}$ and efficiency varies from 70% to 93% depending on the collision centrality and spectrometer settings. On the design level the problem was tried to be solved by reduction of cell width of T3 detector from 2.2 cm to 1.0 cm and increase of X and Y views by one plane in each module.

Special enhancement method was also devised to increase the tracking efficiency in the drift chambers using projections of reconstructed tracks from other detectors to the detector under study. Only hits located in the vicinity of the extrapolated tracks are selected and that leads to a reduction of the combinatorial background and enabling local track reconstruction in high-background environment. The use of this method reduces local tracking inefficiencies by about 60% (see [137]).

4.3.2. Global tracking

The next level of data reconstruction is the global tracking. Local tracks from different detectors are matched through the magnets using vertical parameters of the tracks, which should not be changed in the vertical magnetic field of the bending magnets. Particle momenta are calculated from the track curvature inside the magnets, using the following formula:

$$p = \frac{B \cdot l}{(\sin \Phi_b - \sin \Phi_f) \sqrt{1 - \alpha_y^2}}, \quad (4.1)$$

where B is the magnitude of vertical magnetic field, l the length of the magnet, Φ_{OUT} and Φ_{IN} are defined in Figure 4.6, while α_y is the averaged vertical slope of the tracks. For more details see [138].

Particle trajectory is then matched with the global vertex determined using information from the global detectors, to verify whether given particle is the primary one (coming from the true collision vertex), or is the particle created in secondary processes, in which case it is not included in further analysis. All the hits used to create the local tracks are then used to create a global fit of the particle trajectory. The chi-square parameter of the global fit may be then used to remove incorrectly matched tracks or the in-flight decays.

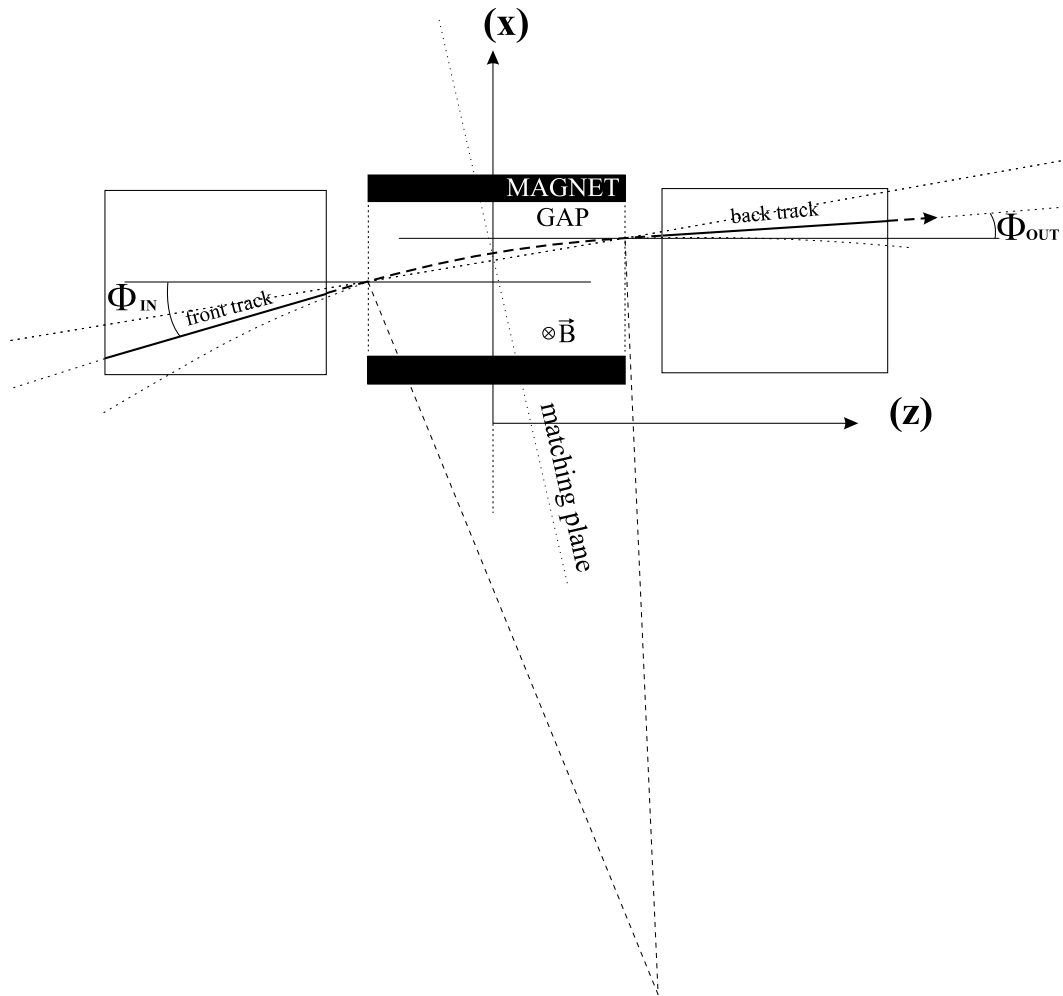


Figure 4.6. Top view of a charged particle trajectory. The relative scale between magnet and tracking chambers is not respected for clarity.

This global fit is also used to calculate the average particle momenta, using formula similar to Equation 4.1. The hits in the hodoscope detectors (H1 and H2) and a ring in RICH detector that are closest to the particle trajectory are identified with the track. Information from the global detectors is also combined to retrieve information about the collision vertex and centrality. Recently also information about the reaction plane is determined.

This is a standard procedure used in the BRAHMS experiment to produce the

global tracks. In the following sections the analysis chain developed especially for this work is presented.

4.4. Particle identification

BRAHMS uses different methods for particle identification (PID) in FS depending on the momentum of the particle. In this work, which focuses mainly on high transverse momenta spectra only Ring Imaging Cherenkov (RICH) was used for PID.

The RICH detector, presented schematically in Figure 4.7, measures the Cherenkov radiation [139] produced by a charged particle moving with velocity v greater than the speed of light ($v_{light} = c/n$) in the gas that fills the detector. The radiation is emitted at a specific angle α :

$$\cos \alpha = \frac{v_{light}}{v} = \frac{c}{n \cdot v}, \quad (4.2)$$

where n is the gas refraction index. The light, produced along the particle trajectory, reflects from a concave mirror at the back of the detector towards finely segmented readout plane of Photo-Multiplier Tubes (PMT). The light focused on the detection plane form ring with radius r :

$$r = L \tan(\cos^{-1}(\frac{1}{n}[1 + \frac{m^2}{p^2}])), \quad (4.3)$$

where $L = 150$ cm is the focal length, m and p are the mass and momentum of the particle, respectively.

Figure 4.8 presents the ring radius measured by the RICH detector versus momenta of the matched tracks. The experimental points (black dots) group along three bands, which are identified as three different particle species: pions, kaons and protons, from top to bottom. In order to calculate the refraction index, narrow slices of 1 GeV/ c have been done in momenta. Sum of three Gaussian functions has been fitted to the obtained distribution, as shown in Figure 4.9. Thus obtained parameters have been used to fit identification functions defined by equation 4.3. The fitted functions are plotted in Figure 4.8 as red, green and blue solid curves for pions, kaons and protons, respectively.

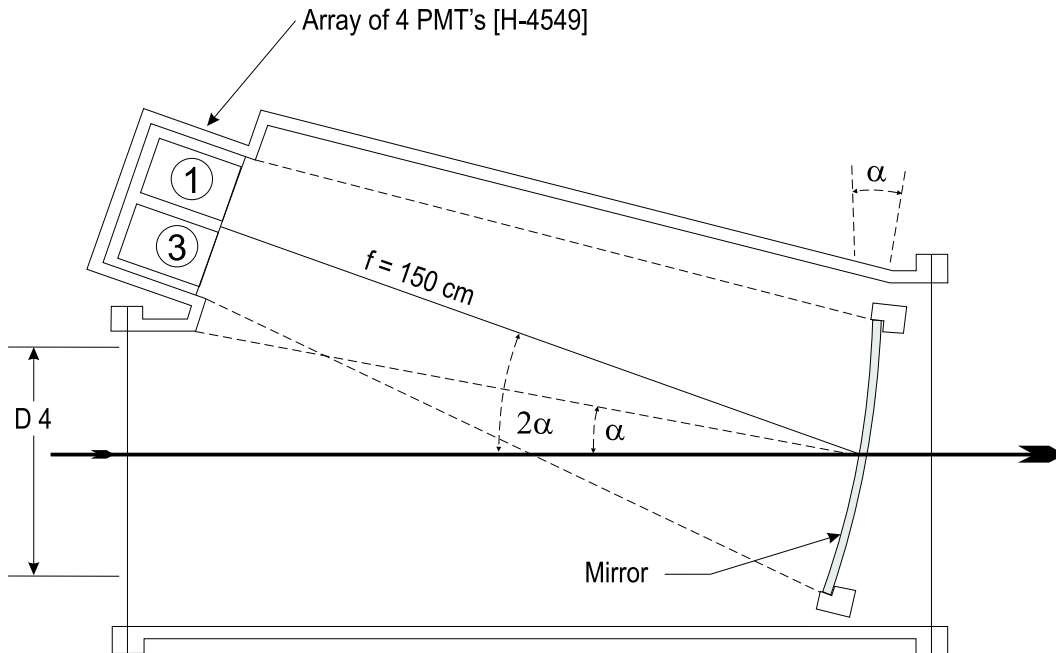


Figure 4.7. Schematic view of the RICH detector.

To calculate the bounds of particle identification, equation 4.3 has been modified to account for the inaccuracy in determination of the radius (δr) and momentum (δp). Radius inaccuracy was taken to be equal to the widths of the fitted Gaussians (multiplied by 3.5), while for δp constant values of 0.4, 0.6 and 0.8 for pions, kaons and protons, respectively, were used. Resulting identification limits are plotted as dotted lines of appropriate colors.

Particles outside of the limiting bounds with non-zero ring radius were not studied at all. When no ring in the RICH detector was found, the particle was assumed to be proton, if its momentum was below the proton threshold, otherwise it was not used in later analysis. Particles inside the bands that could be unequivocally identified were assigned a special number. In the region above $p_T \approx 30 \text{ GeV}/c$, where pion and kaon bounds begin to overlap, the PID is associated according to the probability distribution determined by the Gaussian fits.

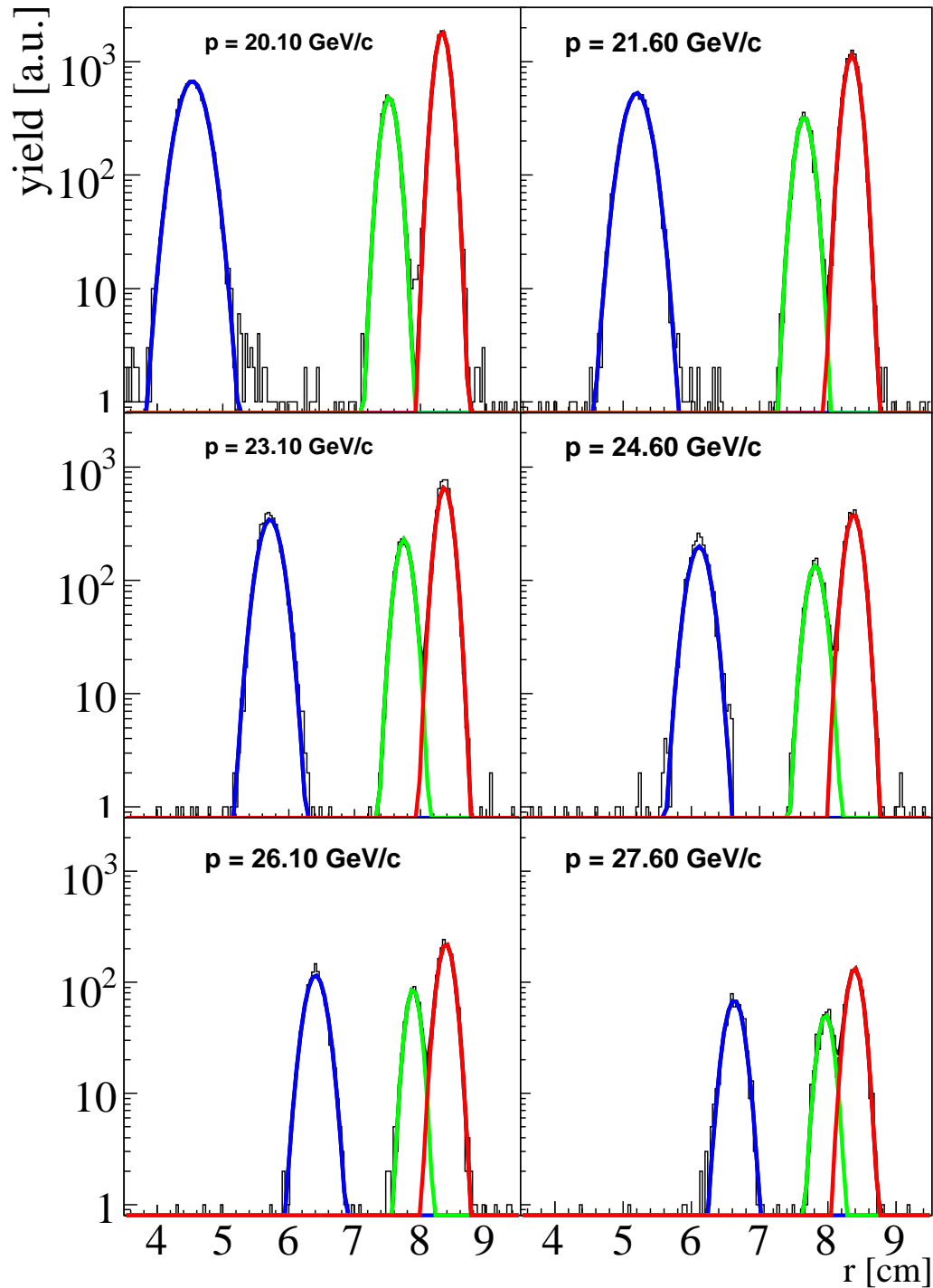


Figure 4.8. Three Gaussian fits to ring radius distribution at various momenta, indicated on the plots. Red, green and blue curves are fits to pions, kaons and protons, respectively.

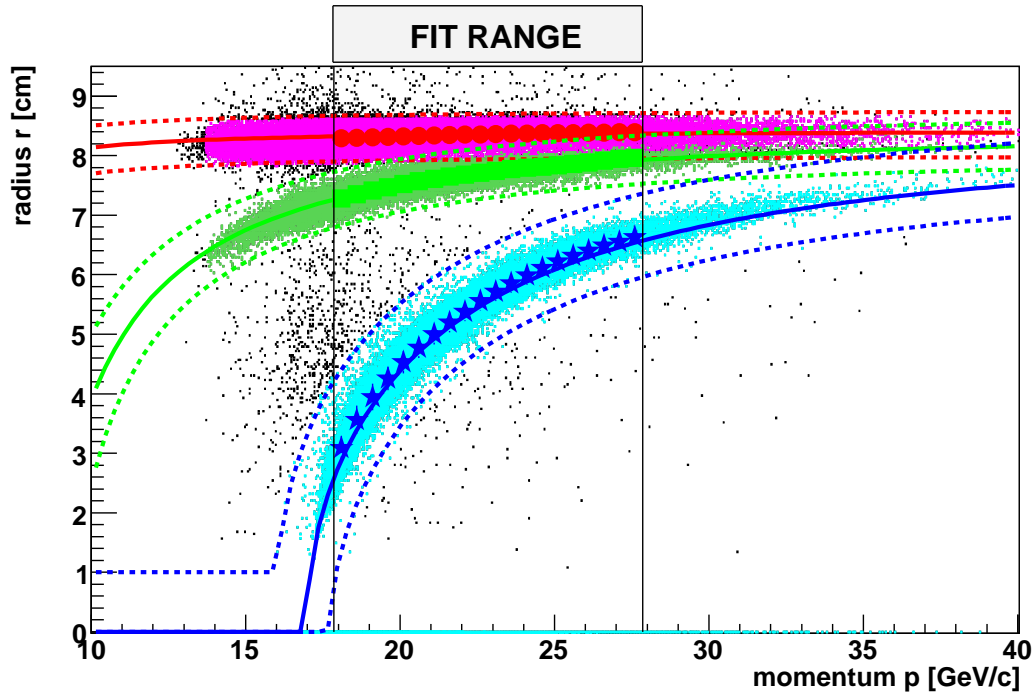


Figure 4.9. Plot showing particle identification curves on ring radius versus momentum plot. Black points show all unidentified particles, red, green and blue show pions, kaons and protons, respectively. Points represent the Gaussian fits (see Figure 4.8), solid lines fits to the points with Eqn. 4.3, and dotted lines represent identification limits.

4.5. Corrections

The data was corrected for efficiency, acceptance, in-flight decays and multiple scattering in the spectrometer. Calculations of corrections are presented below.

4.5.1. Acceptance

For each spectrometer setting a detailed simulation was performed using the BRAHMS detector layout. Due to the dependence of the spectrometer acceptance on the collision vertex the analysis has been performed separately in small vertex bins of 5 cm. A uniform distribution of particles in transverse momentum p_T and polar θ angle was simulated. Due to finite spectrometer acceptance particles were

simulated in a small region of the polar ($\Delta\theta$) and azimuthal ($\Delta\phi$) angle, slightly larger than the angle span of the D1 magnet entrance. The momentum spectrum was cut at $p_T = 6 \text{ GeV}/c$, as no experimental points are detected above the value (due to finite statistics).

Each simulated particle was then checked if it fits within all the magnets and detectors acceptance limits, including certain dead regions of the TPCs. Finally, a fiducial cut on the last tracking detector (T5) was assumed, and only particles from inside the region were treated as accepted.

The ratio of the accepted particles to the simulated ones define the spectrometer acceptance. For convenience, the distributions are stored in two dimensional histograms, where the axis are rapidity and transverse momentum. The final acceptance is thus defined as:

$$Acceptance(y, p_T) = \frac{accepted(y, p_T)}{simulated(y, p_T)} \times \frac{\Delta\phi}{2\pi}. \quad (4.4)$$

Overlap of the experimental data (represented by black boxes) with the acceptance maps (as color histogram) is presented in Figure 4.10. Good agreement is observed for all bins. At the acceptance edges several mismatches are observed, which are related mainly to tracking inefficiencies areas near the edges of the detectors, some unaccounted for errors in magnetic field near the edges and possibly the differences between the true detector positions and that inputted into simulations on a level smaller than the bin-size. To account for these errors edge bins has been disregarded in further analysis.

4.5.2. Efficiency

BRAHMS has developed a special method of calculating the detector efficiencies using only experimental data. The idea is to use the tracks in one of the detectors, extrapolate them to the detector under study and look for the matching tracks in the detector. The number of tracks that were found divided by the number of extrapolated tracks is a relatively good estimator of the efficiency. Moreover, not only the detector efficiency is calculated, but also the efficiency of the matching between the two detectors is accounted for.

The efficiency in a given detector depends on various variables. The most trivial

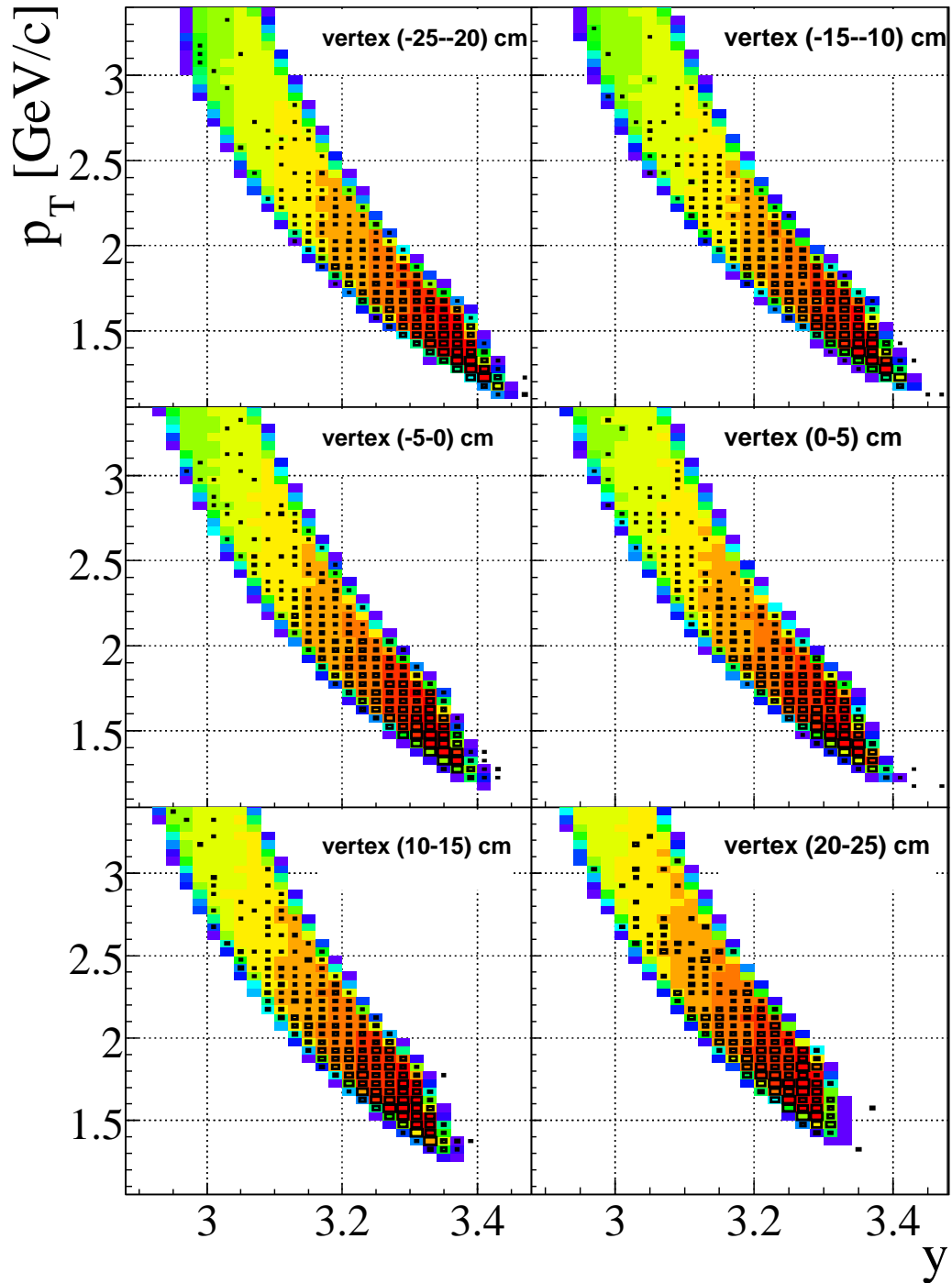


Figure 4.10. The measured data histograms overlaid on the acceptance maps for different vertex bin cuts. The acceptance map is colored and the data is represented by black boxes.

is the position and angular dependence. Due to various detector problems there are regions in each detector that are less efficient. Very important is also the fact, that the tracking efficiency is generally lower in higher background environments, so that parts of the detector experiencing larger background have smaller efficiency. This effect is observed in centrality dependence of the efficiency. More central collisions suffer from lower efficiency. Example dependencies of efficiency for the T3 detector is presented in Figure 4.11.

Therefore for correcting data for efficiency, in Au + Au collisions centrality-position 2 dimensional maps are used. For p + p collisions, where centrality is not measured, position-angle maps are used.

RICH efficiency is determined in a similar fashion. In a relatively low background environment RICH efficiency should solely depend on the ring radius. The efficiency is constant at a level of about 97% for radii larger than $R \gtrsim 2$ cm, while below this value the efficiency drops to 0%. The largest difficulty is in calculating the number of protons in the RICH veto mode, that is below the threshold. It is important to properly include the contamination of pions and kaons, which ring was not detected. In BRAHMS experiment (see Figure 4.12) this is achieved by applying RICH efficiency calculated for high momentum (blue line in the figure) to lower momentum particles. Thus the contamination of pions and kaons as well as a correction for veto protons (red points in the figure) is obtained.

4.5.3. In-flight decay, scattering and absorption

GEANT [140] simulation is used to correct data for the in-flight decays and the particle scattering. Particles are generated in the phase space that overlaps with the spectrometer acceptance and transported through the BRAHMS FS geometry setup. From the number of particles that can be identified at the end of the spectrometer, the correction is calculated. According to our expectations the correction depends solely on the particle specie and momentum, as shown in Figure 4.13.

Physical processes of decay and absorption are completely different for various particle species. To be precise, the largest correction due to decay is expected for kaons, less for pions. On the other hand absorption should have the largest effect on antiprotons. It is trivial to observe that all of the corrections spoken of in this

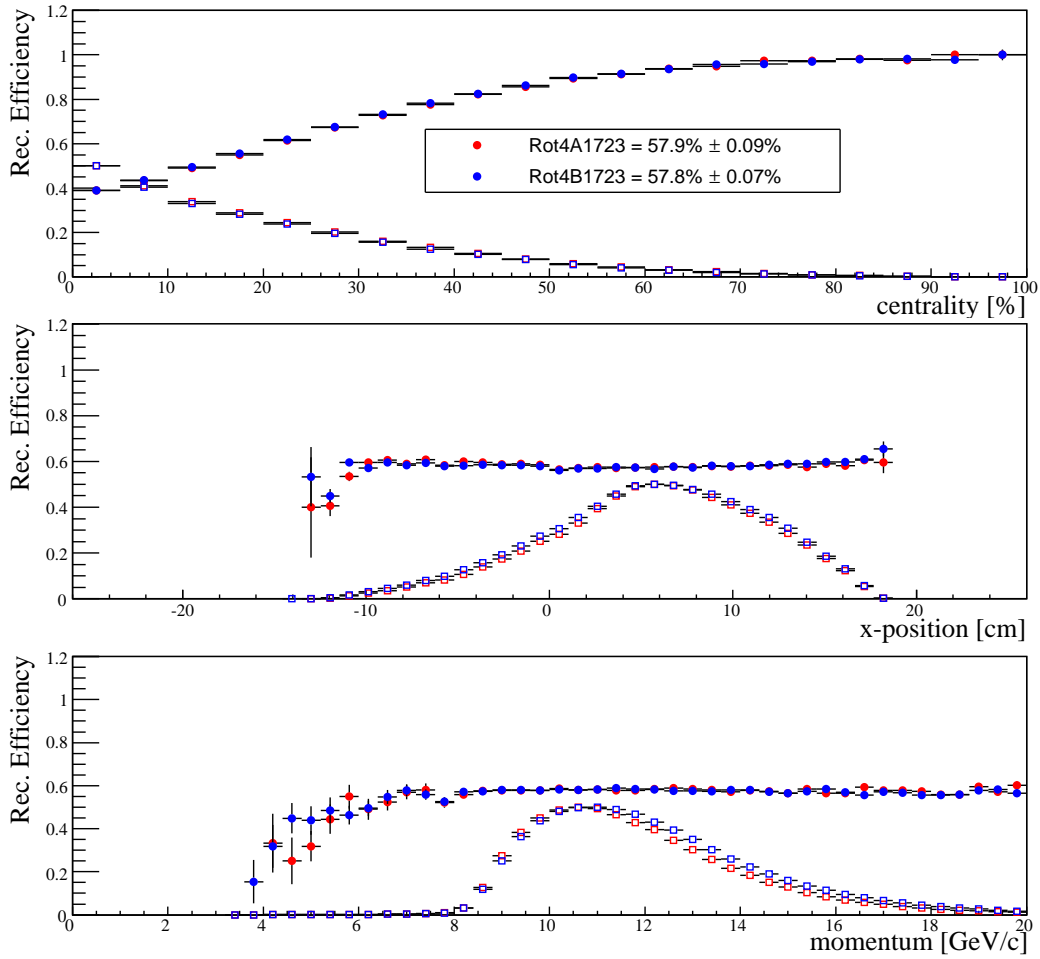


Figure 4.11. T3 efficiency as a function of centrality (top panel), horizontal position in the detector (middle panel) and momentum (bottom panel) in Au + Au collisions at $\sqrt{s_{NN}} = 200$ GeV.

subsection are the largest for low momentum particles.

4.6. Triggers and yield normalization

Event trigger in nuclear experiments is a decisive system composed of detector and electronic circuits, both responding very fast. The detector is to measure interesting events, while electronic circuits have to take quick decision basing on signals

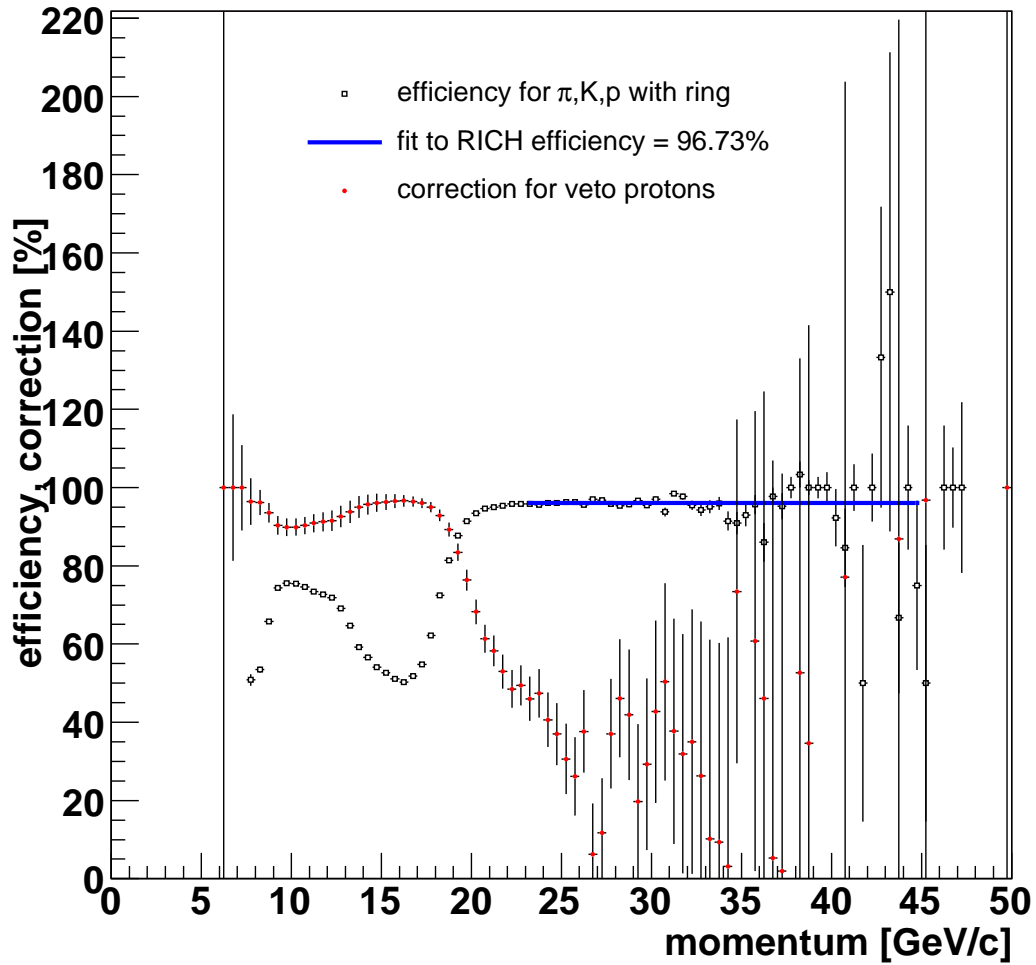


Figure 4.12. RICH efficiency for veto protons.

from the detector about recording or discarding a given event.

BRAHMS experiment has two kinds of triggers. The first kind is called the minimum bias trigger, and its designed to detect full inelastic cross-section. From obvious reasons only global detectors may be utilized in this trigger. In case of Au + Au collisions ZDC and BB are used, while for p + p only CC. Decision about recording of the event is taken if the time difference between signals from detectors placed on the opposite sides of the nominal interaction region suggests that an event occurred. Second level trigger (track trigger) selects the events with tracks in the spectrome-

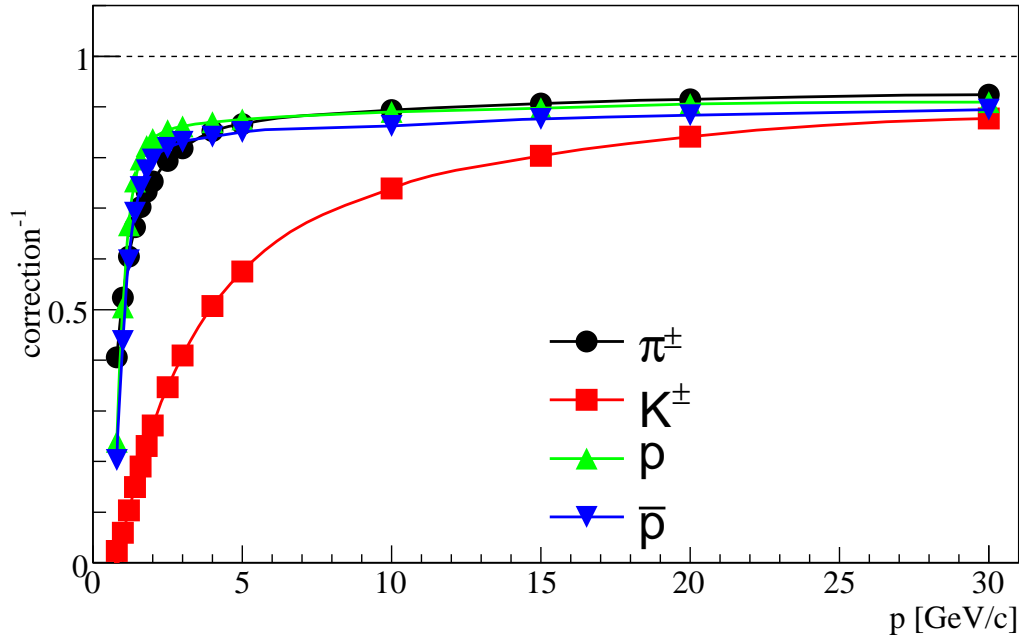


Figure 4.13. Decay, scattering and absorption corrections as a function of momentum for pions (black circles), kaons (red squares), protons (green triangles) and antiprotons (blue upside-down triangles).

ters. There are three triggers here: MRS trigger (signal coincidence in TOFW and ZDC), FFS trigger (H1+ZDC) and FS trigger (H1+H2+ZDC) (in the $p + p$ reactions CC is used instead of ZDC).

BRAHMS acquisition system can record no more than about 150 events per second. However, there are thousands of events per second taking place in the interaction region (with minimum bias trigger). In fact, often the number of MRS triggers alone per second exceeds 1000. This situation forces BRAHMS to record selectively the most interesting events. The selection bases on specific scale-downs applied for each trigger individually. Scale-downs are the ratios of all events to the events that we want to record. Extraction of the absolute yield in the data analysis requires proper normalization that bases on the scale-down information. Below I present the normalization method used in obtaining results of this thesis.

For simplicity reasons lets reduce problem to two triggers only, one minimum

bias trigger (MB) and another one (A) that selects events having tracks in FS. Out of N events seen in the interaction region N_{MB} is the number of events seen by MB trigger only, and $N_{MB,A}$ are those seen by MB and A triggers. There are also a number of tracks T , divided into T_{MB} and $T_{MB,A}$, respectively. In an ideal situation, if all events could be recorded, yield can be written as:

$$\frac{T}{N} = \frac{T_{MB} + T_{MB,A}}{N_{MB} + N_{MB,A}}. \quad (4.5)$$

This is presented graphically in Figure 4.14.

In BRAHMS only a fraction of events is recorded on disk as decided by the scale-down factors, S_{MB} and S_A . Out of N_{MB} events a fraction ($\overline{N_{MB}} = 1/S_{MB} \times N_{MB}$) was recorded, which is shown on figure as an area shaded by right-falling lines. For $N_{MB,A}$ it is more complicated, since both triggers participate in decisive procedure, some ($1/S_{MB}$) were recorded by trigger MB (right-falling lines in Figure 4.14) and some ($1/S_A$) were recorded by trigger A (left-falling lines in Figure 4.14). As can be seen the fraction of the events recorded on disk is not a simple sum, but has to be rather written in form:

$$\overline{N_{MB,A}} = \left(1 - \left(1 - \frac{1}{S_{MB}}\right)\left(1 - \frac{1}{S_A}\right)\right) \times N_{MB,A}. \quad (4.6)$$

Similar fractions of the tracks were recorded on disk ($\overline{T_{MB}}$ and $\overline{T_{MB,A}}$). Now the proper way to calculate the yield using the tracks and events recorded on disk is:

$$\frac{T}{N} = \frac{T_{MB} + T_{MB,A}}{N_{MB} + N_{MB,A}} = \frac{\frac{1}{S_{MB}} \times \overline{T_{MB}} + \frac{1}{1 - \left(1 - \frac{1}{S_{MB}}\right)\left(1 - \frac{1}{S_A}\right)} \times \overline{T_{MB,A}}}{\frac{1}{S_{MB}} \times \overline{N_{MB}} + \frac{1}{1 - \left(1 - \frac{1}{S_{MB}}\right)\left(1 - \frac{1}{S_A}\right)} \times \overline{N_{MB,A}}}. \quad (4.7)$$

Equation 4.7 that has been obtained for the simplified case of two triggers, can be generalized into:

$$\frac{T}{N} = \frac{\sum_t T_t}{\sum_t N_t} = \frac{\sum_t \left(\left(1 - \prod_{s_t} \left(1 - \frac{1}{s_t}\right)\right) \times \overline{T}_t \right)}{\sum_t \left(\left(1 - \prod_{s_t} \left(1 - \frac{1}{s_t}\right)\right) \times \overline{N}_t \right)}, \quad (4.8)$$

where t runs over different trigger combinations (MB and MB,A in this simplified case), while s_t are appropriate scale-downs for different triggers in a given trigger combination.

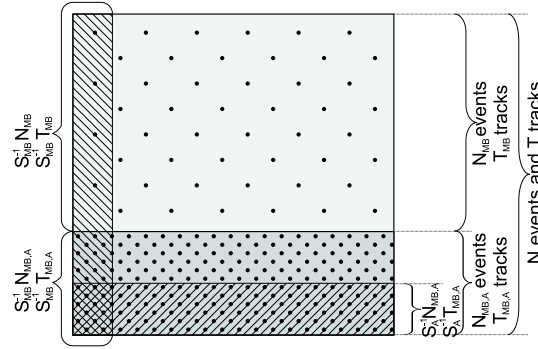


Figure 4.14. Events (plain) and tracks (dots) seen by triggers MB and A of the experiment. Areas marked with right- and left-falling lines represent recorded events and tracks.

4.7. Construction of particle spectra

It has been mentioned that the acceptance of BRAHMS spectrometer arms is very small. This implies that in order to obtain large coverage in rapidity and transverse momentum it is necessary to analyze many spectrometer settings. Generally the change of the spectrometer angle probes different rapidities, while steering amplitude of magnetic field in FS magnets governs the accessible p_T range. Figure 4.15 presents coverage of the rapidity- transverse momentum ($y - p_T$) phase space with the use of many spectrometer settings distinguished with the use of different colors.

Calculation of all the corrections has been done separately for every particle in small vertex bins (with a width of 5 cm) and centrality bins (in case of Au + Au collisions only, with a width of 10%) for each spectrometer setting. Thus obtained $y - p_T$ maps were subsequently averaged. Figure 4.16 presents averaged transverse momentum spectrum and individual spectra from different spectrometer settings used for the average. Resulting $y - p_T$ map for positive pions in Au + Au collisions at $\sqrt{s_{NN}} = 200$ GeV is presented in Figure 4.17.

4.8. Glauber Model

To calculate the nuclear modification factor it is necessary to know the number of binary collisions for given centrality class. It is common to use the Glauber

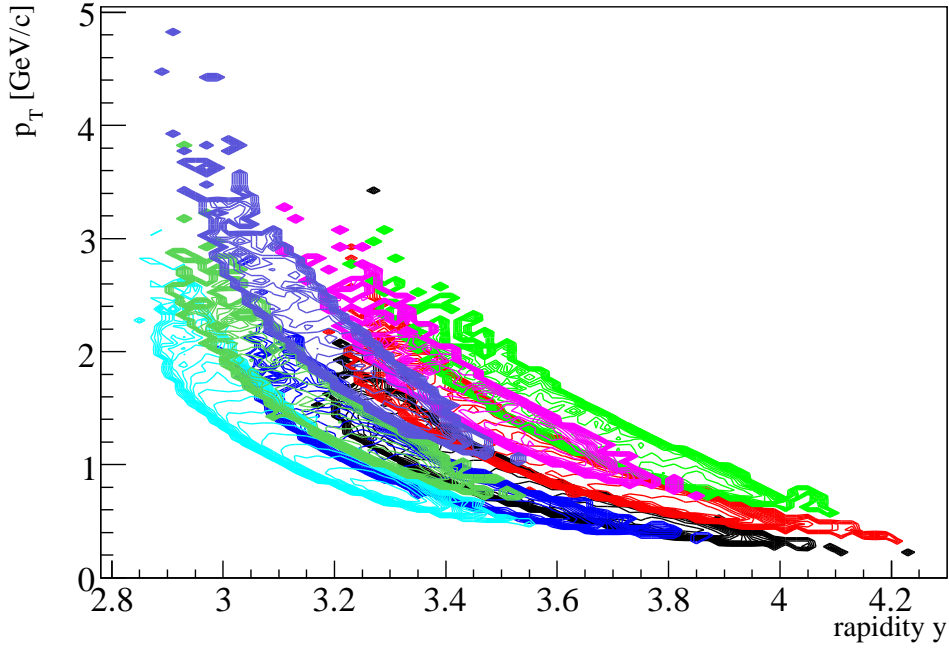


Figure 4.15. $y - p_T$ scatter plot coverage with different spectrometer settings represented by different colors.

model [141] to obtain N_{coll} and N_{part} . In practice there are two possible realizations of the model, referred to as the Monte Carlo Glauber Model and the Optical Glauber Model.

1. **Optical Glauber Model.** In the approach the number of binary collisions and number of participants is calculated analytically in the overlap region of two colliding nuclei [142]. In BRAHMS experiment spherically symmetric Woods-Saxon nucleus density profile is used:

$$\rho(r) = \frac{\rho_0}{1 + \exp \frac{r-r_0}{c}}, \quad (4.9)$$

where radius parameter $r_0 = 6.38^{+0.27}_{-0.13}$ fm, density $\rho_0 = 0.169 \text{ fm}^{-3}$ and diffusivity $c = 0.535 \pm 0.01$ fm. Thickness function in the overlapping region of

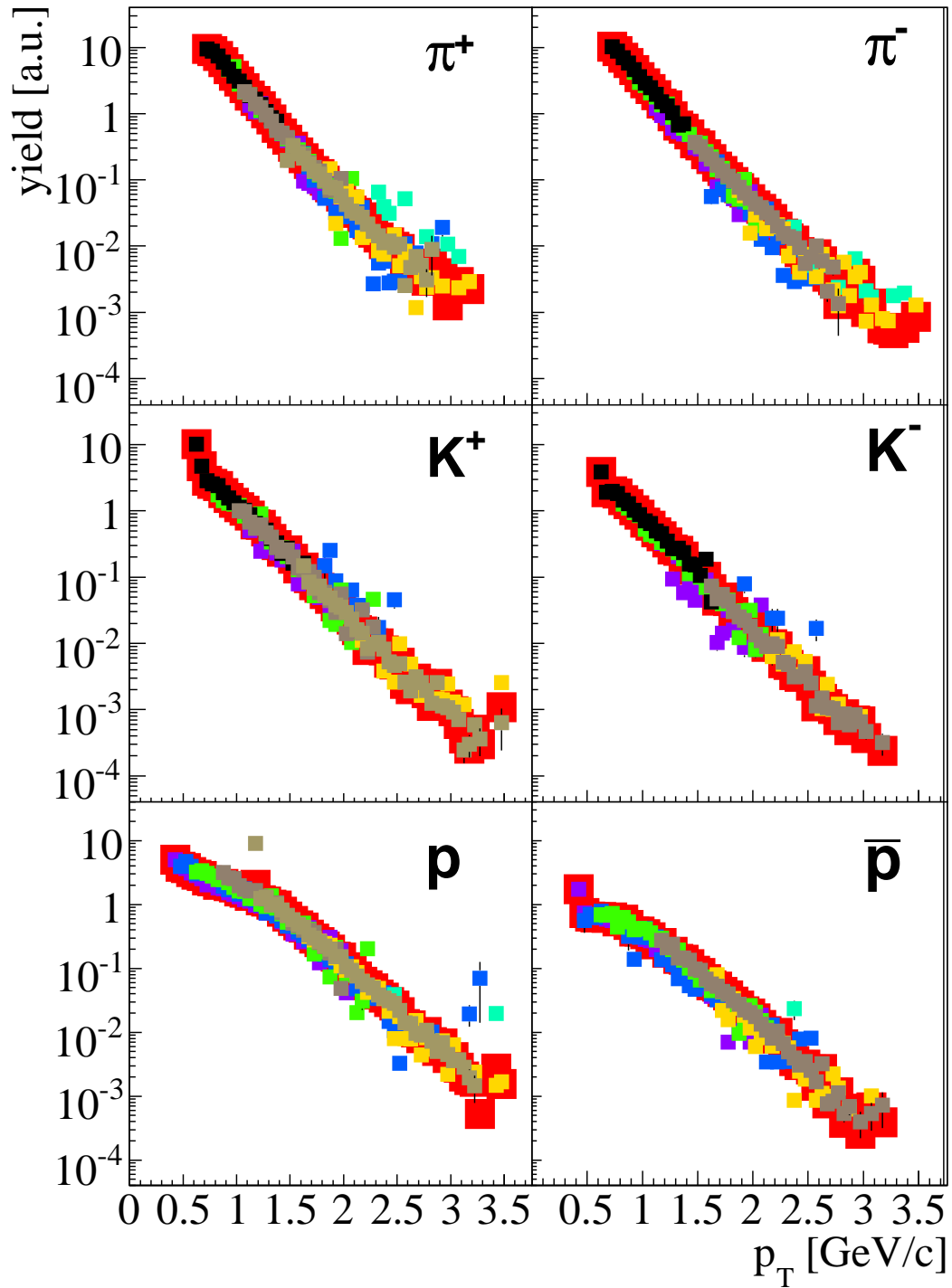


Figure 4.16. Contribution of different spectrometer settings to the final transverse momentum spectra (shown as red squares) are presented as smaller squares with different colors.

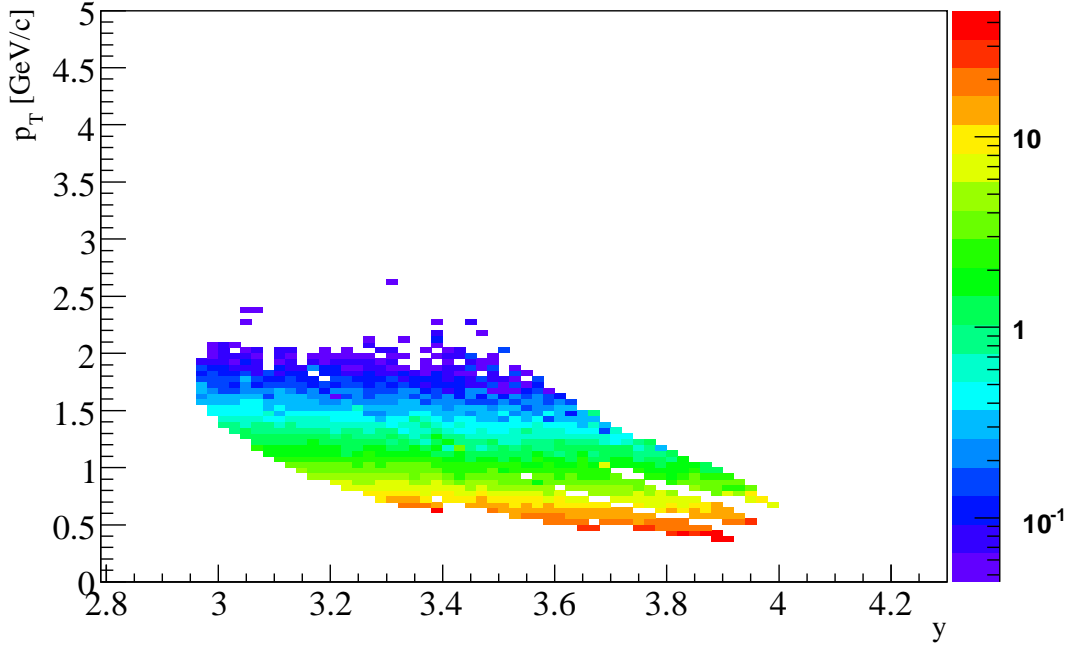


Figure 4.17. $y - p_T$ scatter plot coverage obtained after applying all corrections and normalizing to the number of events.

the collision at impact parameter \vec{b} is given by integral

$$T_{AA}(b) = \int d^2s dz_1 dz_2 \rho_1(\vec{s}, z_1) \rho_2(\vec{s} - \vec{b}, z_2), \quad (4.10)$$

where \vec{s} is vector perpendicular to the beam axis z , while z_1 and z_2 are nucleons' positions along the beam axis. The function (normalized to unity) gives probability of finding nucleons from both nuclei at a given position. Using the thickness function it is possible to calculate the number of binary collisions:

$$N_{coll} = A \cdot A \cdot T_{AA}(\vec{b}) \sigma_{N+N}^{inel}, \quad (4.11)$$

and the number of participants:

$$N_{part} = 2A \int d^2s T_{AA}(\vec{s}) [1 - (1 - T_{AA}(\vec{s} - \vec{b}) \sigma_{N+N}^{inel})^A]^2, \quad (4.12)$$

where the value of nucleon-nucleon inelastic cross-section is set to $\sigma_{N+N}^{inel} = 42 \pm 2$ mb for collisions at $\sqrt{s_{NN}} = 200$ GeV.

2. **Monte Carlo Glauber Model.** In this model Monte Carlo (MC) method is used to simulate positions of individual nucleons in two nuclei (at a given impact parameter) according to a density profile set by the Woods-Saxon distribution. The two nuclei are subsequently brought to collide at a given impact parameter. The nucleons from different nuclei move with straight trajectories and are said to “interact”, if the distance (r) between them is small enough:

$$r \geq \sqrt{\frac{\sigma_{N+N}^{inel}}{\pi}}. \quad (4.13)$$

Summing over interacting nucleons gives the number of participants, while the number of binary collisions is determined by summing the interactions.

The results of the two approaches are generally similar except for the peripheral region. This is caused by the cut-off in the impact parameter in the optical model, while in MC calculations there is no limitation on impact parameter. Prescriptions of the model can be find in Ref. [143] and references within.

5 Results

5.1. Introduction

Previous chapters gave an overview of selected observables studied at the RHIC collider with a special focus on the nuclear modifications of jets created in the heavy ion collisions.

In this chapter new results obtained by author of this dissertation will be presented. Since the beginning of my work with the BRAHMS Collaboration five years ago I have been working on data taking, detector calibrations and software development. In the last three years I focused on obtaining identified particle transverse momentum spectra at forward rapidities in Au + Au and p + p collisions at $\sqrt{s_{NN}} = 200$ GeV. This required creation of dedicated programs to analyze the data taken with the Forward Spectrometer and the global detectors. Special techniques have been developed by myself for particle identification using RICH detector (section 4.4) and normalization of the particle spectra (section 4.6). A lot of work has been put into calculation of the tracking detector efficiencies (section 4.5.2), which is entirely maintained by the Krakow group. For this work a completely novel approach to the RICH efficiency has been developed. In order to increase the acceptance of the spectrometer the new method of applying fiducial cuts has been introduced (section 4.5.1).

For the first time high quality transverse momentum spectra of identified particles from BRAHMS experiment for Au + Au and p + p collisions at $\sqrt{s_{NN}} = 200$ GeV at rapidities larger than 3 were obtained and are presented in section 5.2. The spectra have been used to construct the nuclear modification factors at large rapidity in Au + Au collisions (see section 5.3). This is of particular interest for understanding the mechanisms of particle suppression in this rapidity region.

5.2. Identified particle spectra

The $y - p_T$ map coverage analyzed in this work is presented in Figures 5.1 and 5.2, for Au + Au and p + p collisions at $\sqrt{s_{NN}} = 200$ GeV, respectively. Left (right) panels in both figures present scatter plots for positive (negative) identified particles: pions, kaons and protons from top to bottom. The analysis uses data from Front Spectrometer set at three angles (4° , 3° and 2.3°) and three different magnetic fields. Minimum bias event statistics obtained for the analyzed settings are presented in Table 5.1.

Au + Au	4°	3°	2.3°	Au + Au	4°	3°	2.3°
positive				negative			
full field	10767k	1098k	455k	full field	11010k	2105k	1547k
$1/\sqrt{2}$ field	1677k		1633k	$1/\sqrt{2}$ field			1848k
half field	5007k	1170k	676k	half field	3975k	2493k	1475k

p + p	4°	3°	2.3°	p + p	4°	3°	2.3°
positive				negative			
full field	11282k		27401k	full field	20302k		22842k
$1/\sqrt{2}$ field	1140k			$1/\sqrt{2}$ field	2357k		
half field	4307k		1194k	half field	4208k		1525k

Table 5.1

Minimum bias event statistics for each analyzed spectrometer settings in case of Au + Au (upper row) and p + p (bottom row) analysis.

The pion data covers rapidity from $y \approx 3.0$ to $y \approx 4.0$. The widest transverse momentum range ($0.7 \gtrsim p_T \gtrsim 3.0$ GeV/ c) is obtained for rapidity bin $3.1 < y < 3.3$. For heavier particles the $y - p_T$ space coverage moves to smaller rapidities

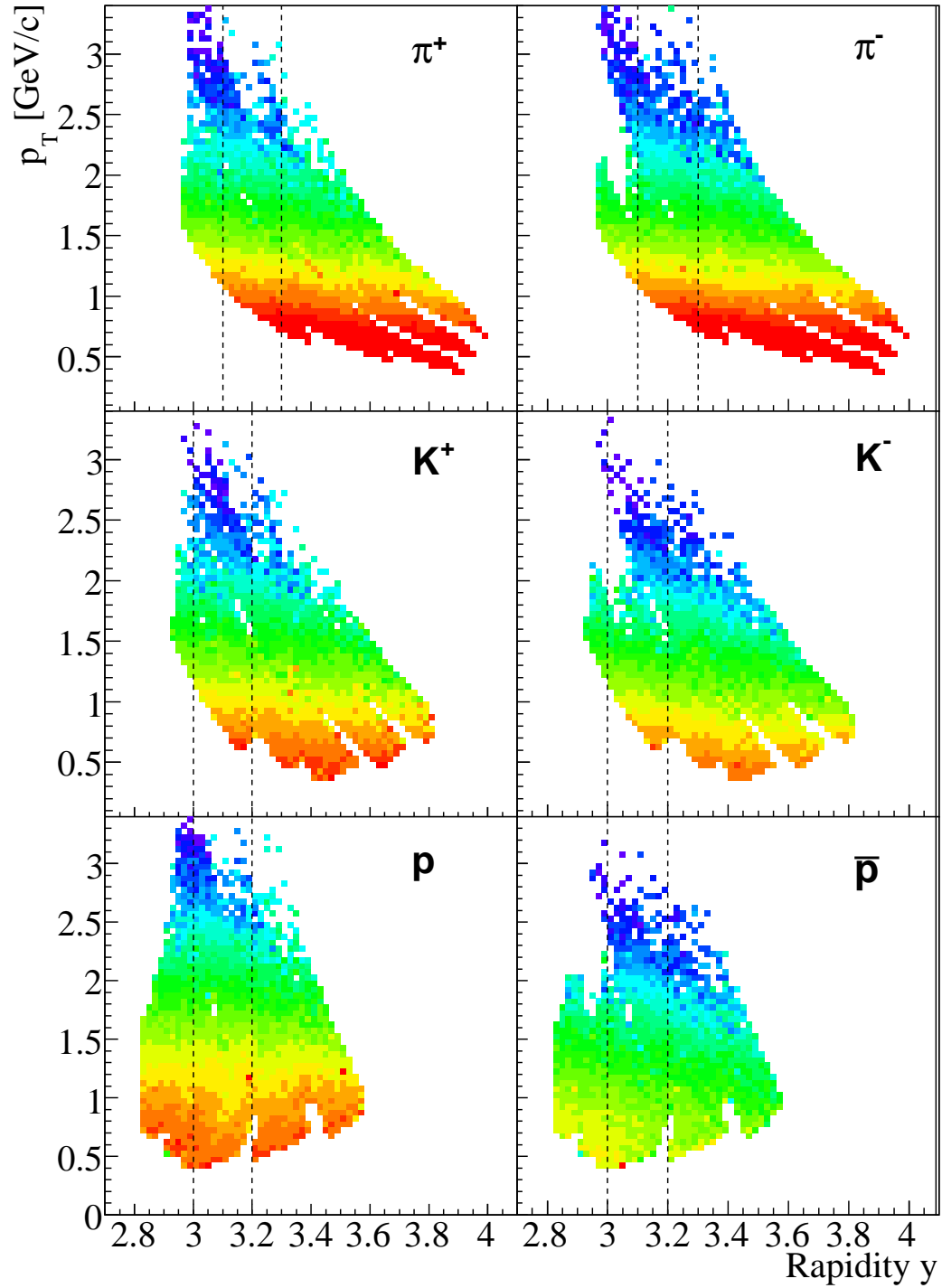


Figure 5.1. $y - p_T$ scatter plots in Au + Au collisions at $\sqrt{s_{NN}} = 200$ GeV for identified particles: pions, kaons and protons are shown in top, middle and bottom panels, respectively. Left (right) panel presents positive (negative) particle spectra. The dashed lines illustrate the rapidity intervals used in analysis of R_{AA} .

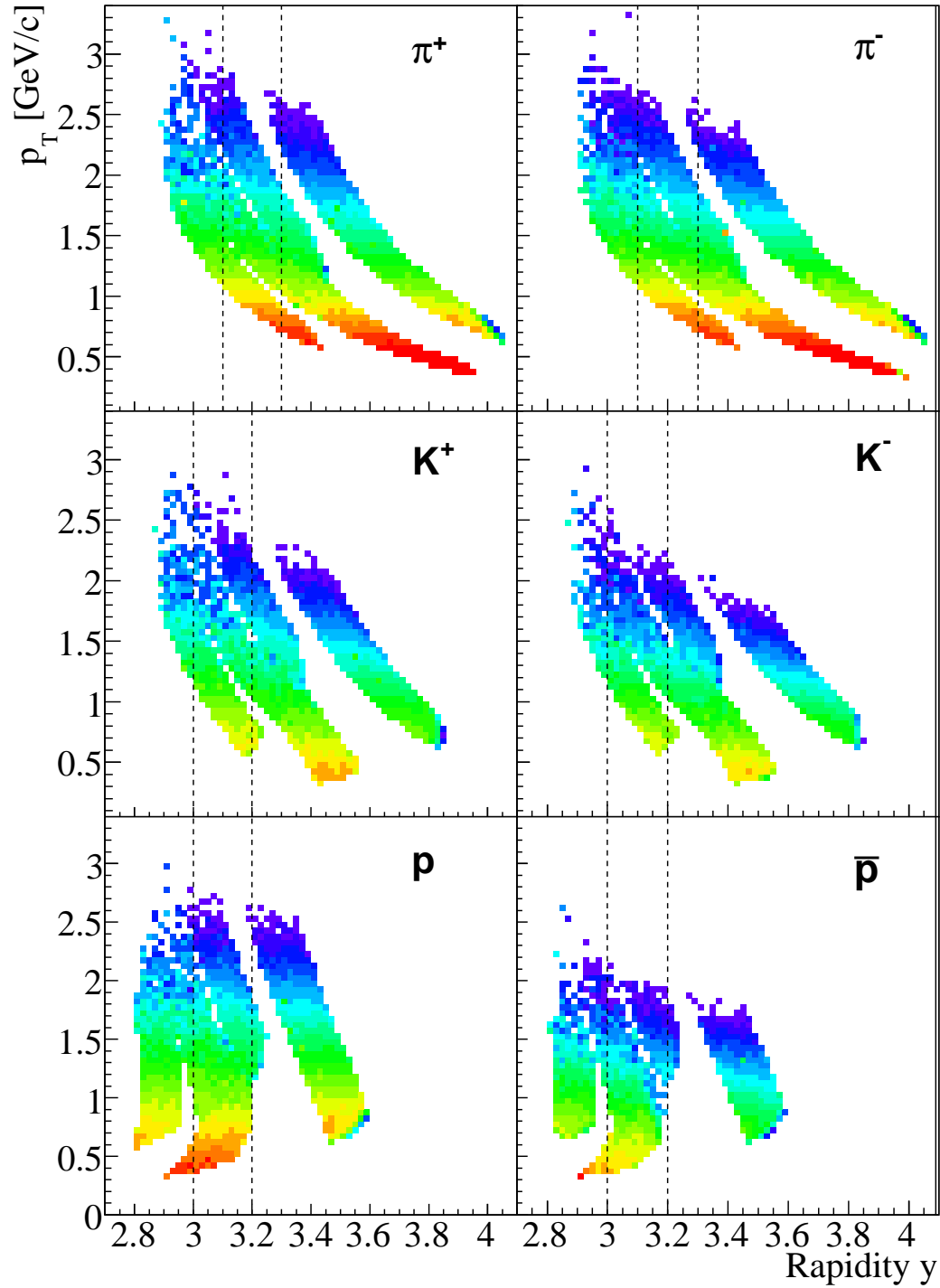


Figure 5.2. $y - p_T$ scatter plots coverage in $p + p$ collisions at $\sqrt{s_{NN}} = 200$ GeV for identified particles: pions, kaons and protons are shown in top, middle and bottom panels, respectively. Left (right) panel presents positive (negative) particle spectra. The dashed lines illustrate the rapidity intervals used in analysis of R_{AA} .

and transverse momenta. Therefore the rapidity is covered from $y \approx 2.9$ (2.8) to $y \approx 3.8$ (3.6) for kaons (protons). The largest p_T range is reached for the rapidity bin $3.0 < y < 3.2$, where transverse momentum coverage is $0.6 \gtrsim p_T \gtrsim 3.0$ GeV/ c and $0.4 \gtrsim p_T \gtrsim 3.0$ GeV/ c for kaons and protons, respectively. There are no corrections applied for the feedback from particle resonances decay to pion, kaon (from ϕ , Ω or K^*) nor proton (mostly from Λ) production. However, in obtaining the nuclear modification factors these corrections do cancel out.

Transverse momentum spectra for identified particles in Au + Au (for four indicated centralities) and p + p collisions are presented in Figure 5.3. Left panels present positive particles (pions, kaons and protons in the top, middle and bottom panel, respectively), while right one negative particles. The error bars indicated on the plot are only statistical, and in most cases are smaller than the marker size. Shape of the spectra obtained for Au + Au collisions is essentially the same in various centrality classes for all particle species under study, but shows differences as compared to p + p transverse momentum spectra.

5.3. Nuclear modification factor

5.3.1. Numbers of binary collisions and participants

In order to obtain nuclear modification factors it is necessary to properly calculate number of binary collisions. This value cannot be experimentally observed, it can only be deduced from the event centrality using theoretical model of nucleus-nucleus collision. This estimation is the largest source of systematic uncertainties to the presented results on R_{AA} .

All four RHIC experiment uses the Glauber Model that was presented in section 4.8, to calculate both the number of participants and the number of binary collisions.

The values of N_{part} and N_{coll} used by the BRAHMS experiment are summarized in Table 5.2.

5.3.2. R_{AA} for unidentified hadrons

Weak dependence of R_{AA} on rapidity has already been reported by the BRAHMS Collaboration in [109], where nuclear modification factors for unidentified hadrons at mid-rapidity and forward rapidity of 2.2 were shown. The independence of R_{AA}

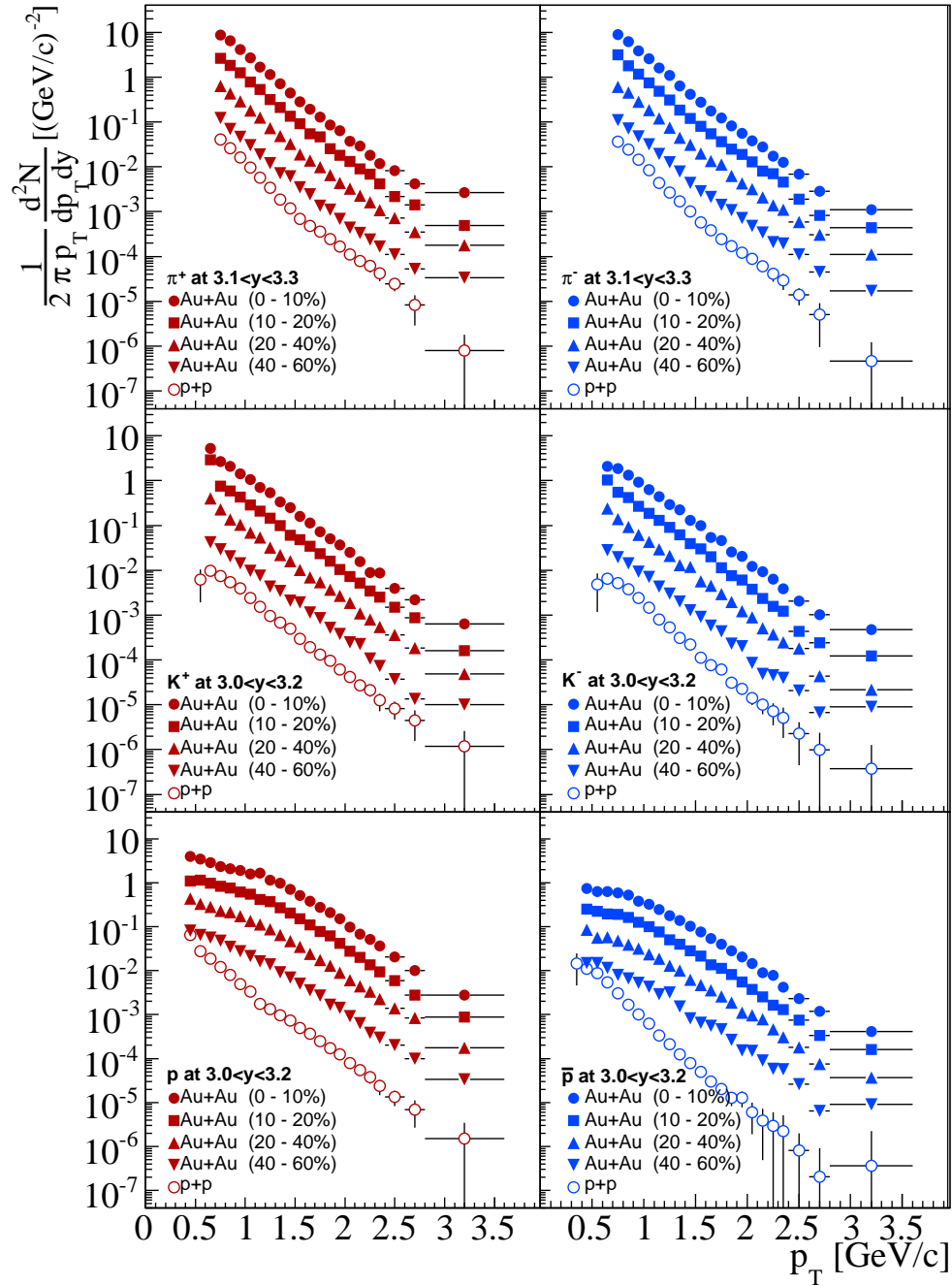


Figure 5.3. Transverse momentum spectra for identified particles in Au + Au and p + p collisions at $\sqrt{s_{NN}} = 200$ GeV. Pions, kaons and protons are shown in top, middle and bottom panels, respectively. Left (right) panel presents positive (negative) particle spectra. Rapidity bin for the projections had been defined in Figures 5.1 and 5.2. Solid points show spectra from Au + Au collision at four different centralities (for convenience spectra at centrality 10 – 20%, 20 – 40% and 40 – 60% are scaled by 0.4^1 , 0.4^2 and 0.4^3 , respectively). Open points show spectra for p + p collisions.

centrality σ/σ_{tot} [%]	$\langle N_{part} \rangle$	$\langle N_{coll} \rangle$	$\langle b \rangle$ [fm]
0 - 10	$328.6^{+3.87}_{-5.82}$	$886.8^{+96.72}_{-123.96}$	$3.2^{+0.19}_{-0.14}$
10 - 20	$233.3^{+7.97}_{-8.51}$	$534.3^{+71.43}_{-85.22}$	$6.0^{+0.34}_{-0.26}$
20 - 40	$134.2^{+9.01}_{-8.63}$	$244.2^{+44.28}_{-47.53}$	$8.5^{+0.48}_{-0.37}$
20 - 30	$161.7^{+8.93}_{-8.90}$	$315.5^{+52.00}_{-57.63}$	$7.8^{+0.44}_{-0.34}$
30 - 40	$107.4^{+9.09}_{-8.36}$	$174.8^{+36.55}_{-37.44}$	$9.2^{+0.52}_{-0.40}$
40 - 60	$56.1^{+7.76}_{-6.49}$	$71.2^{+19.65}_{-17.83}$	$10.9^{+0.62}_{-0.48}$
40 - 50	$70.9^{+8.42}_{-7.25}$	$96.8^{+24.34}_{-22.88}$	$10.3^{+0.59}_{-0.46}$
50 - 60	$41.9^{+7.09}_{-5.79}$	$46.9^{+15.20}_{-12.78}$	$11.5^{+0.66}_{-0.51}$
60 - 90	$12.7^{+3.55}_{-2.72}$	$10.6^{+4.85}_{-3.45}$	$12.0^{+0.79}_{-0.59}$
60 - 70	$22.7^{+5.31}_{-4.18}$	$20.8^{+8.54}_{-6.35}$	$12.0^{+0.71}_{-0.55}$
70 - 80	$10.8^{+3.42}_{-2.53}$	$8.2^{+4.19}_{-2.79}$	$12.0^{+0.77}_{-0.59}$
80 - 90	$4.7^{+1.93}_{-1.41}$	$3.1^{+1.82}_{-1.20}$	$12.0^{+0.88}_{-0.65}$

Table 5.2

Numbers of participants and numbers of binary collisions for different centrality classes in Au + Au collisions at $\sqrt{s_{NN}} = 200$ GeV calculated with Glauber model.

with rapidity has been explained in a 3D hydrodynamical model of Hirano and Nara [129], where high- p_T jets generated in perturbative QCD loose energy in the medium that evolves according to 3D hydrodynamic equations. The authors of [129] also make a prediction on behavior of R_{AA} at larger rapidity of 3.25. Comparison of their predictions with the nuclear modification factor obtained in my analysis is plotted in Figure 5.4.

Identified particle spectra in Au + Au and p + p collisions have been added to obtain spectra for unidentified hadrons (h^+ , h^- and $h^+ + h^-$). Spectra from Au + Au collisions were divided by appropriate spectra from p + p reactions and scaled by the number of binary collisions. In the whole available transverse momentum range the

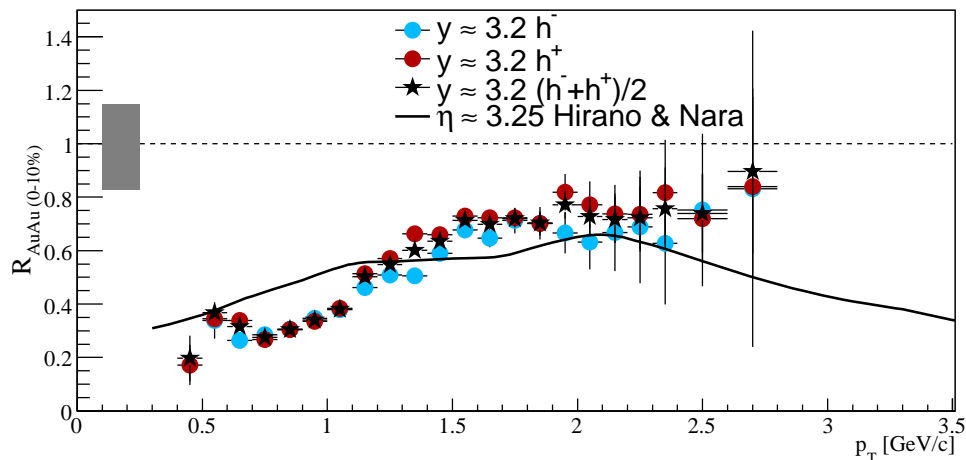


Figure 5.4. Nuclear modification factor for unidentified hadrons in Au + Au collisions at $\sqrt{s_{NN}} = 200$ GeV. Blue circles show R_{AA} for negative hadrons, red for positive, while black crosses is for all charged hadrons. Statistical errors at points are shown. The systematic error arising from the N_{coll} uncertainty and normalization error is represented by gray box at unity.

nuclear modification factor for unidentified hadrons stays below unity. Even above 2 GeV/c, where particle production should be dominated by the jet fragmentation, no scaling with N_{coll} is achieved. The predictions by Hirano and Nara show overall good agreement in the level of suppression, however the shape of R_{AA} slightly differs from that observed experimentally. Unfortunately, limited acceptance of the Forward Spectrometer does not allow for measurements at $p_T > 3.5$ GeV/c, where hydrodynamical calculations show decrease of the nuclear modification factor.

5.3.3. R_{AA} for identified hadrons

Spectra obtained for the pions, kaons and protons (see section 5.2) are used in the present section to calculate nuclear modification factors at $y \approx 3.2$ in 10% central Au + Au collisions at $\sqrt{s_{NN}} = 200$ GeV.

The spectra obtained for identified positive and negative hadrons in the Au + Au collisions were divided by appropriate p + p spectra. The positive and negative spectra have been added to obtain average spectra for pions ($\pi^+ + \pi^-$), kaons ($K^+ + K^-$) and protons ($p + \bar{p}$). Figure 5.5 presents nuclear modification factors for identi-

fied hadrons (pions, kaons and protons) which were obtained at forward rapidity of $y \approx 3.2$. Nuclear modification factors for identified pions is below unity in the whole transverse momentum range, and has a maximum at $p_T \approx 1.8 \text{ GeV}/c$ reaching value of about 0.5. Kaons also show suppression, with a shape similar to that of pions. For these strange mesons however the level of suppression is smaller, hence R_{AA} reaches 0.8. Nuclear modification for protons show enhancement above $p_T \approx 1.3 \text{ GeV}/c$. It raises from the lowest transverse momenta in the whole available p_T range, although signs of decrease are seen above $p_T \approx 2.2 \text{ GeV}/c$. The systematic errors in this region are however too large to make any strong conclusions.

It is incredible to notice that the behavior of the nuclear modification factors for identified hadrons at forward rapidity mimics that observed at mid-rapidity. Figure 5.6 presents comparison of the nuclear modification factors obtained by PHENIX [144] and STAR [110] Collaborations at mid-rapidity with BRAHMS results at forward rapidity $y \approx 3.2$ for pions, kaons and protons. There is almost no difference between the results at the two presented rapidities, which is most probably caused by the coincidental interplay between influence of the jet quenching and the slope of the spectra on R_{AA} (see section 5.4).

5.3.4. Centrality Dependence

Figure 5.7 shows centrality dependence of the nuclear modification factors for identified hadrons at forward rapidity. For all three particle species strong and similar dependence on centrality is observed, R_{AA} grows with decreasing collision centrality. Pions and kaons, which for central collisions experience strong suppression, in peripheral collisions scale with the number of binary collisions (i.e. R_{AA} is consistent with N_{coll} scaling). R_{AA} for kaons reveals enhancement already for 20 – 40% centrality bin, while for pions only the most peripheral bin presented in this analysis (40 – 60%) shows Cronin-type behavior. The enhancement of proton production observed in central Au + Au collisions in the medium transverse momentum range also increases with decreasing centrality.

Similar strong dependence of R_{AA} on centrality has been also observed at mid-rapidity. Transverse momentum independence of π^0 nuclear modification factor

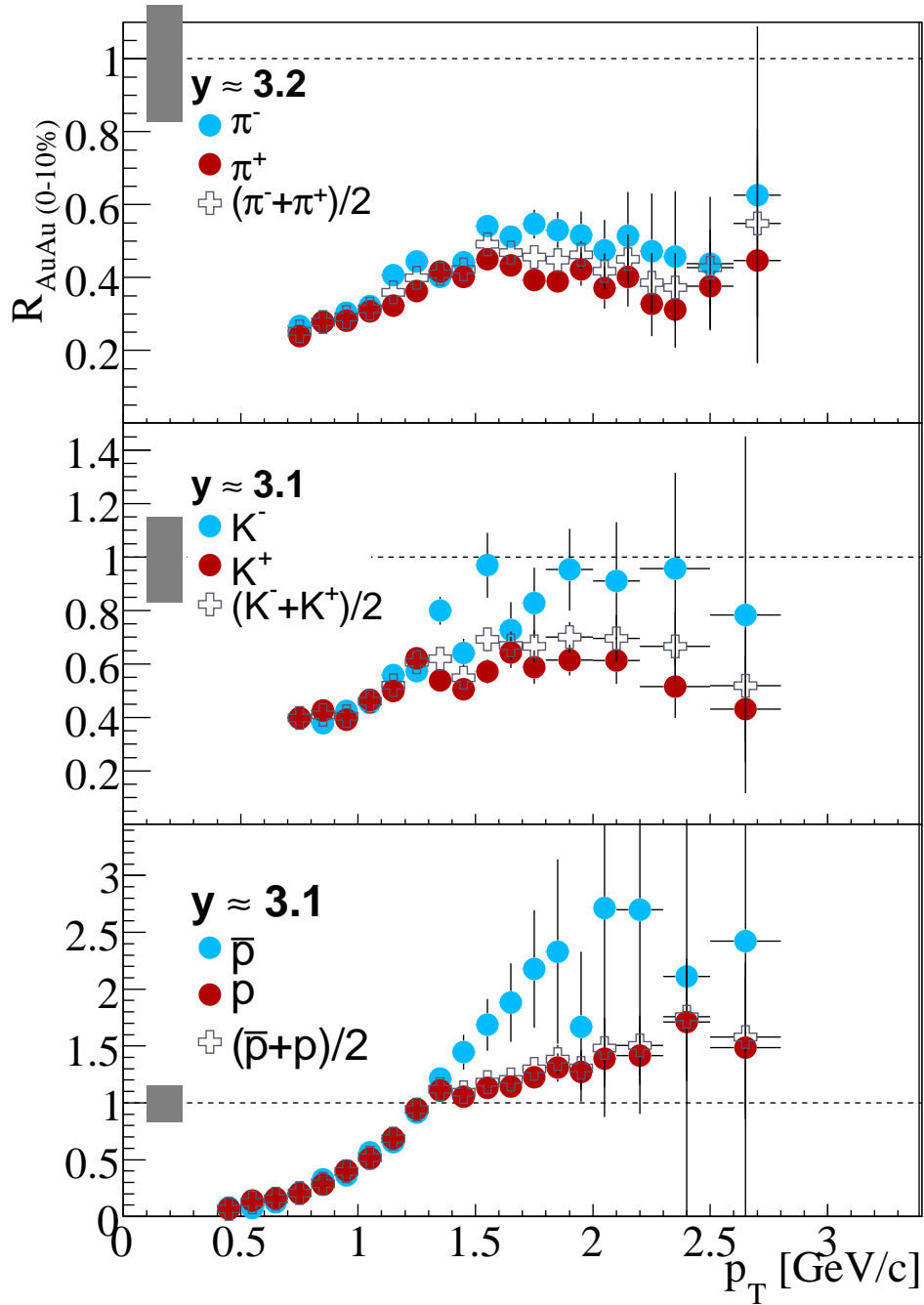


Figure 5.5. Nuclear modification factor for identified hadrons in Au + Au collisions at $\sqrt{s_{NN}} = 200$ GeV. Top panel shows pions, middle kaons and bottom protons. In all panels blue circles show R_{AA} for negative hadrons, red for positive, while black crosses for the sum of positive and negative. Statistical errors at points are shown. The systematic error arising from the N_{coll} uncertainty and normalization error is represented by gray boxes at unity.

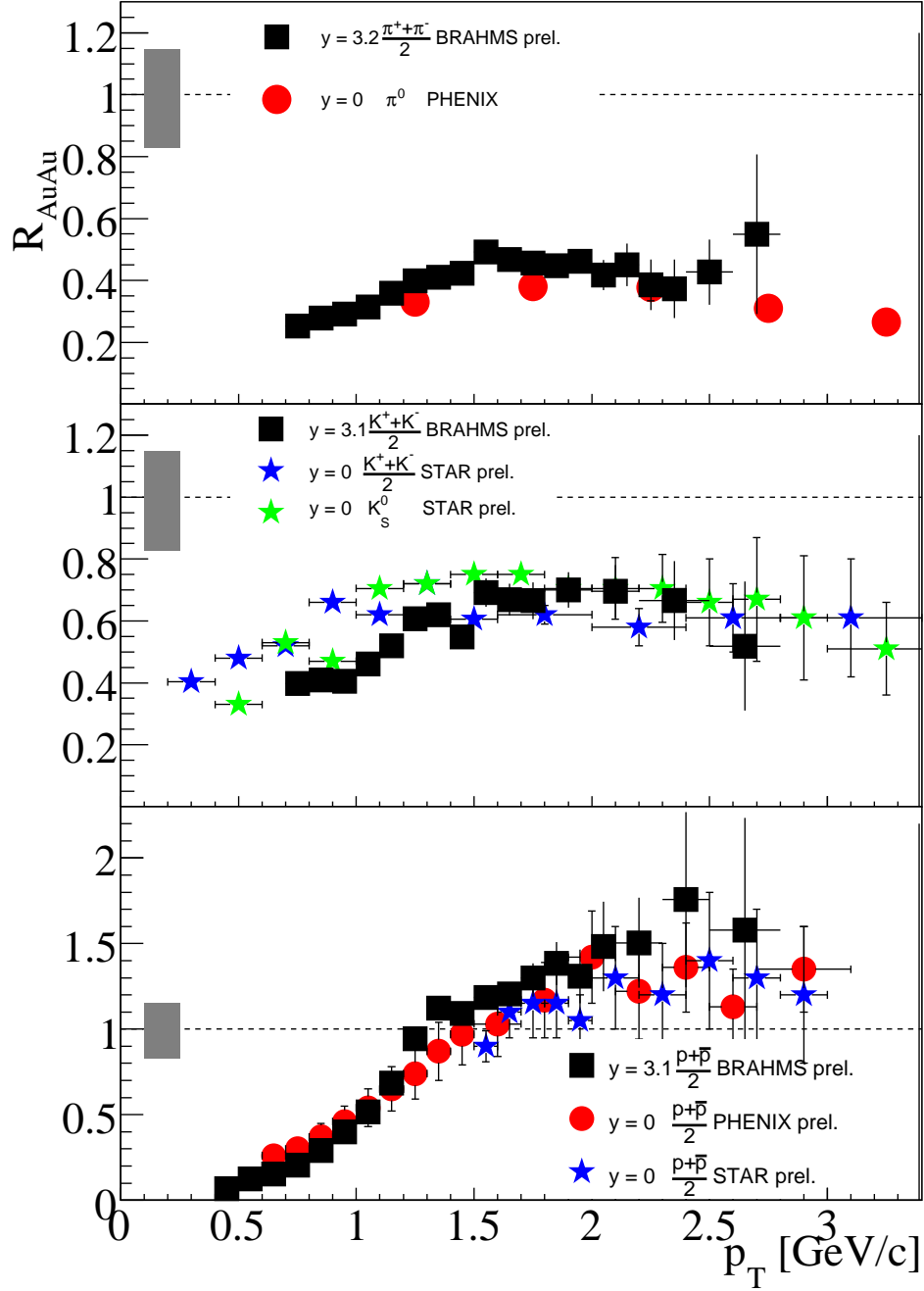


Figure 5.6. Comparison of nuclear modification factors obtained for central Au + Au collisions at $\sqrt{s_{NN}} = 200$ GeV at mid-rapidity and forward rapidity for identified hadrons. Top panel shows pions, middle - kaons and bottom - protons. In all panels red circles are PHENIX mid-rapidity data [144], green and blue stars are STAR [110] results at $y \approx 0$, while black squares are BRAHMS results at forward rapidity ($y \approx 3.2$) obtained in this work. Statistical errors at points are shown. The systematic error arising from the N_{coll} uncertainty and normalization error is represented by gray boxes at unity.

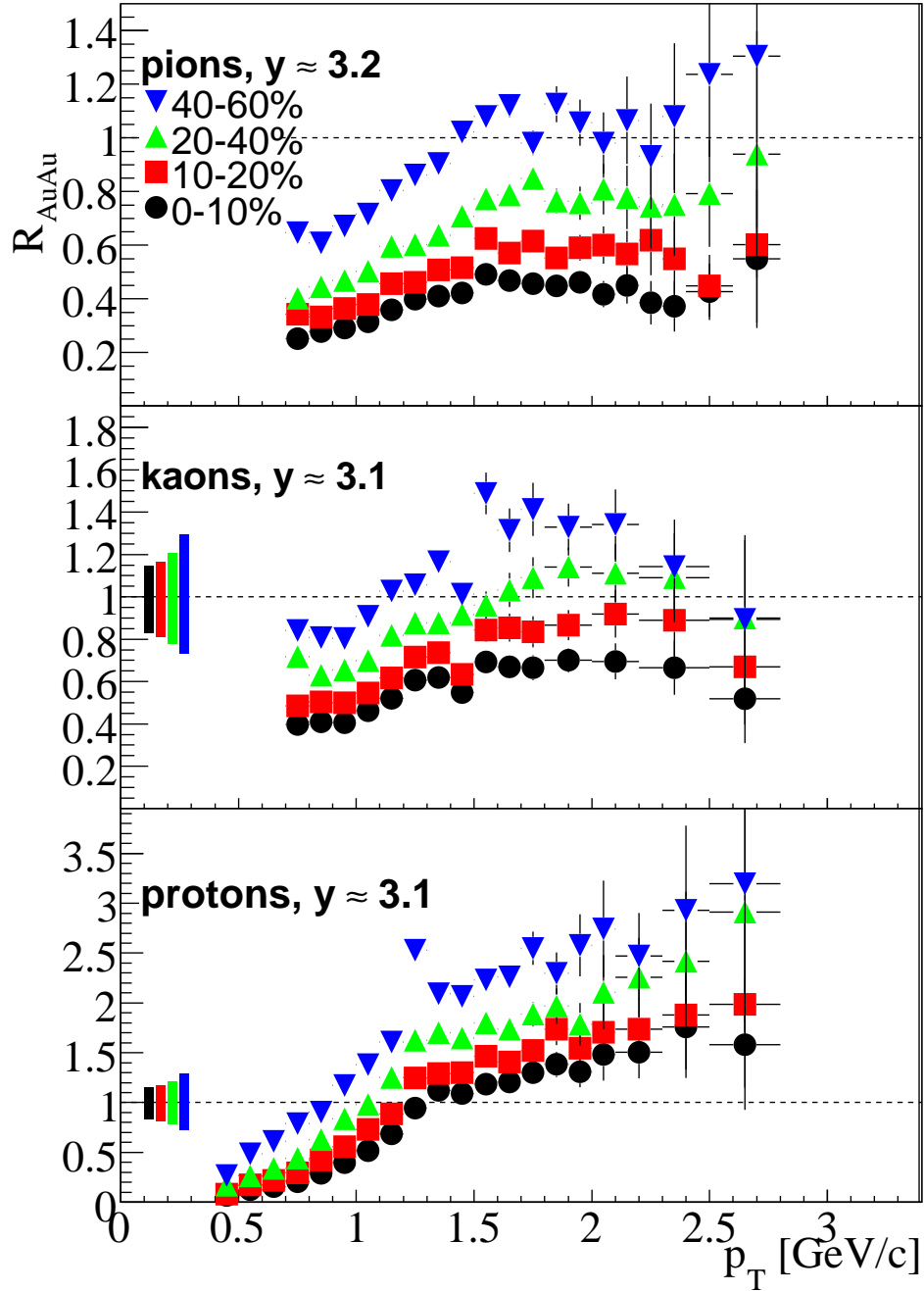


Figure 5.7. Centrality evolution of the nuclear modification factors in Au + Au collisions at center-of-mass energy 200 GeV at forward rapidity of 3.2 for identified hadrons. Top panel shows pions, middle kaons and right - protons. Black circles, red squares, green triangles and blue triangles represent different centrality classes: 0 – 10%, 10 – 20%, 20 – 40% and 40 – 60%, respectively. Statistical errors are shown as error bars at points. Systematic uncertainties that increase with decreasing centrality are shown as appropriate colors bars at unity.

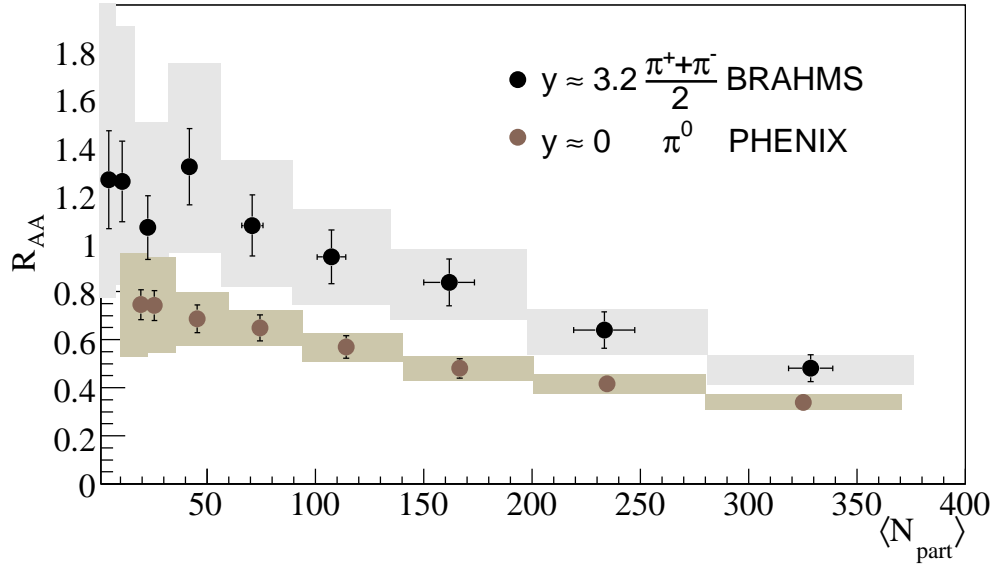


Figure 5.8. Change of integrated nuclear modification factor with centrality in Au + Au collisions at $\sqrt{s_{NN}} = 200$ GeV. Brown circles are PHENIX data [144] for neutral pions at mid-rapidity, black squares are results for charged pions obtained at rapidity $y \approx 3.2$.

for $p_T > 5$ GeV/ c inspired the PHENIX Collaboration [108] to present integrated R_{AA} as a function of the number of participants (see section 3.3.2). This inspired me to plot similar dependence at forward rapidity for high transverse momenta ($p_T > 2$ GeV/ c), where nuclear modification factors for identified pions (π^+ and π^-) are approximately independent of p_T . The results of PHENIX results for π^0 and BRAHMS experiment results for charged pions in the same transverse momentum region are presented in Figure 5.8. It is very intriguing that although suppression for central events is comparable at the two rapidities, R_{AA} grows faster at forward rapidity than at mid-rapidity with decreasing centrality. This is consistent within theoretical frame of parton energy loss in strongly absorbing medium [123]. In the model, particle production at mid-rapidity is dominated by surface emission, while at forward rapidities transition to emission from the whole volume may occur. The transition in consequence leads to stronger dependence on N_{part} , observed in the experimental data.

5.3.5. Higher rapidities

BRAHMS experiment can also measure and identify particles at rapidities larger than 3.2. It is clear from the $y - p_T$ scatter plots presented in section 5.2 that going to larger rapidities limits the p_T coverage. Nevertheless, as presented in Figure 5.9 available data show that pions even at the highest available rapidity ($3.7 < y < 3.9$) still experience suppression in central Au + Au collisions at top RHIC energy, even though the transverse momentum range is very limited. The strong suppression for $y \approx 3.8$, where p_T range reaches 2.4 GeV/ c is remarkable and suggests that the strongly interacting dense medium extends up to very high rapidities. Surprising fact is that at larger rapidities nuclear modification for kaons in Au + Au central collisions is consistent with unity. R_{AA} for protons does not reveal any dependence with rapidity in the range covered in the present analysis.

5.4. Discussion of the results

Independence of nuclear modification factor on rapidity still requires theoretical explanation. There are however several possible physics pictures that currently seem to be most promising in explaining the phenomenon.

5.4.1. Slope influence

Hirano and Nara [129] observed that the nuclear modification factor is affected by the slope of the p_T spectrum. In short, the same nuclear modification will produce larger change of R_{AA} in the case of steeper transverse momentum spectrum. They also observe, that the particle p_T spectrum above ~ 2.5 GeV/ c is more steep in the forward rapidity region than at mid-rapidity. Therefore weaker in-medium jet quenching at large rapidity may produce nuclear modification factor comparable to that observed at mid-rapidity. They argue that the observed similarity of the suppression level at mid-rapidity and forward rapidity might be a coincidence.

5.4.2. CGC effect

It has been proposed [145] that the suppression of jets at forward angles may be in part caused by initial state effects, like CGC. Central d + Au collisions at mid-rapidity reveal Cronin-type enhancement, at forward rapidities however small level

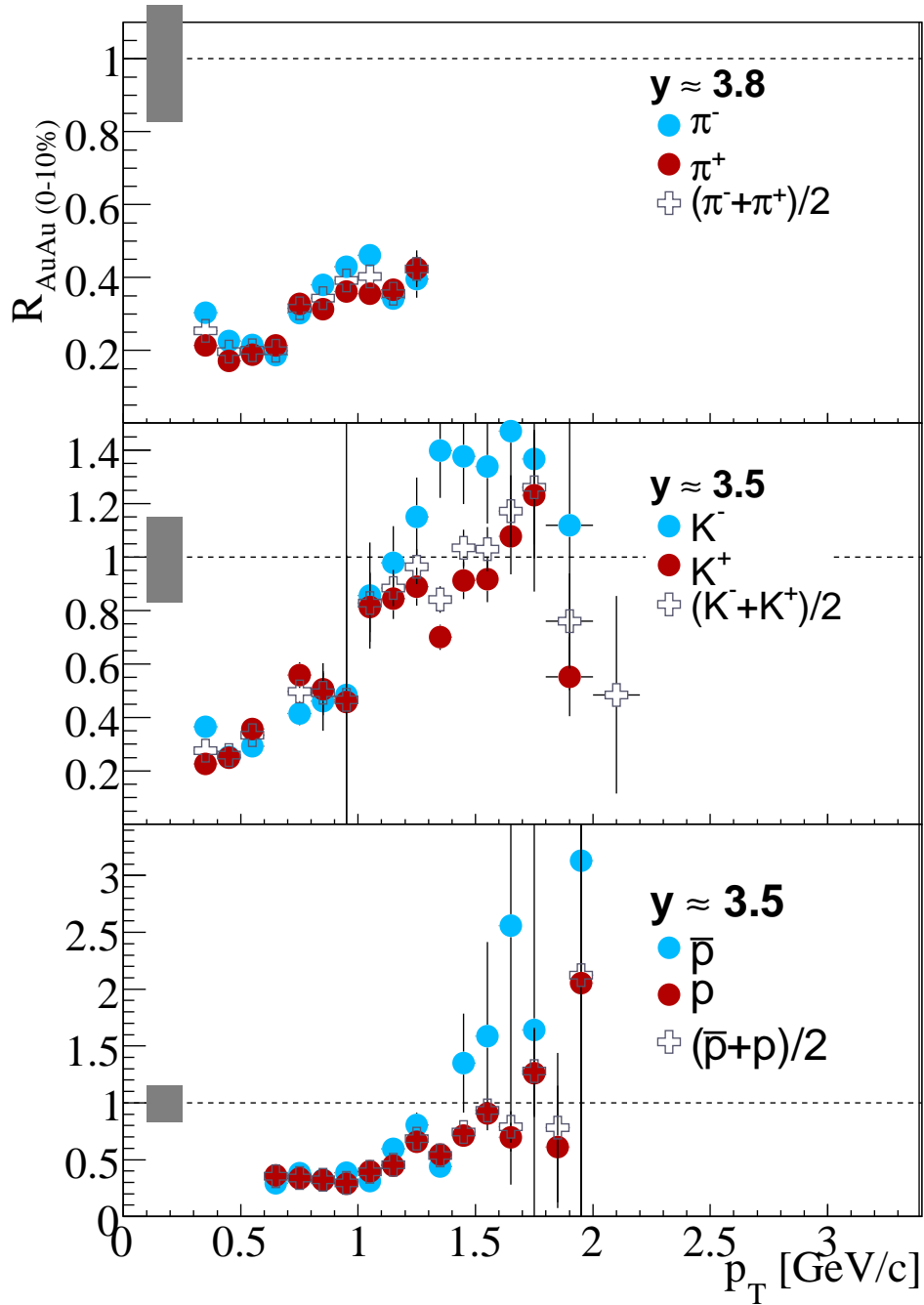


Figure 5.9. Nuclear modification factors at the highest available rapidity for identified hadrons. Top panel shows pions, middle kaons and bottom - protons. In all panels blue circles show R_{AA} for negative hadrons, red for positive, while black crosses for the sum of positive and negative. Statistical errors at points are shown. The systematic error arising from the N_{coll} uncertainty and normalization error is represented by gray boxes at unity.

of suppression is observed. Since no dense medium is expected to be created in d + Au collisions the suppression is usually explained in terms of the CGC effect. As has been referred in section 3.4.6 high energy jet production may be quenched due to saturation of gluon densities at small x , which is experimentally observed in the forward rapidity region. The explanation of the forward rapidity suppression is however not possible in terms of CGC effects only, final state interactions have probably larger impact on the suppression.

5.4.3. Scaling with energy density

When comparing centrality dependence of R_{AA} at mid-rapidity and forward rapidity, number of participants was used as a scaling variable. It was supported by the fact of almost perfect scaling of the nuclear modification factor for Au + Au and Cu + Cu collisions with this variable. It has been however suggested that R_{AA} would show smoother dependence on the energy density. This variable can be estimated using Bjorken formula [68] and experimental $dN_{ch}/d\eta$. Such estimation has been performed and results of the analysis are shown in Figure 5.10. The dependencies at mid-rapidity and forward rapidity are almost aligned in the comparison, except for the two most central points at forward rapidity. To confirm the scaling with energy density it is important to make a systematic survey of all available data gathered by the RHIC experiments. In particular, rapidity comparison presented in this section should be amended with the data gathered at lower energy of $\sqrt{s_{NN}} = 62.4$ GeV and for smaller colliding system (Cu + Cu).

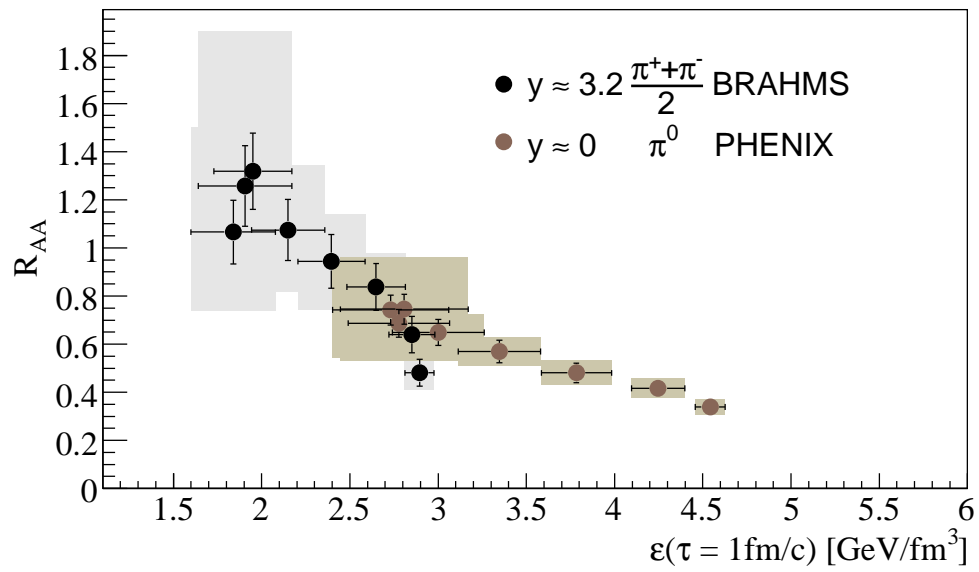


Figure 5.10. Change of integrated nuclear modification factor with energy density (ϵ) in Au + Au collisions at $\sqrt{s_{NN}} = 200$ GeV. Brown circles are PHENIX data [144] for neutral pions at mid-rapidity, black squares are results for charged pions obtained at rapidity $y \approx 3.2$.

6 Conclusions

BRAHMS experiment has been designed for precise measurement of the identified hadron transverse momentum spectra in the wide range of rapidities. Especially the forward rapidity coverage, unique among the family of RHIC experiments, requires special treatment. Results obtained on nuclear modification factors in the forward rapidity region are of particular interest as they are the only ones to give information about the longitudinal evolution of the hot and dense medium created in heavy ion collisions at ultra-relativistic energies.

In my work for the first time high quality results on forward rapidity identified particle production had been obtained. Unexpectedly strong suppression of high transverse momenta pions and kaons in central Au + Au collisions at $\sqrt{s_{NN}} = 200$ GeV is observed at $y \approx 3.2$, at a level similar to that measured at mid-rapidity. Independence of R_{AA} on rapidity is also seen for protons, which experience medium- p_T enhancement in all accessible rapidity range at RHIC. The similarity of the nuclear modification factors at forward rapidity to that at mid-rapidity is presumably caused by interplay between the in-medium jet quenching and slope influence. The nuclear modification factor for all hadron species measured by the BRAHMS experiment increase with decreasing centrality, and the growth is faster than that observed at mid-rapidity, which is consistent with the surface emission scenario. Preliminary results show approximate scaling of the averaged R_{AA} with the initial energy density at $y \approx 0$ and 3.2.

The results indicate that the quark-gluon plasma extends longitudinally to very forward region of $y \approx 3.2$ and that the particle production is dominated by the surface emission. Comparison with the 3D hydrodynamical model shows that the mechanisms of particle suppression at forward rapidities are still not thoroughly understood. Analysis performed within my doctoral research allows for verification of the jet quenching models in terms of their ability to explain the forward rapidity data. The results have been presented by me at the Quark Matter conference in

Budapest in 2005 [146] and at the RHIC & AGS Annual Users' Meeting at BNL in 2006.

A The BRAHMS Collaboration

I. Arsene¹¹, I.G. Bearden⁶, D. Beavis¹, S. Bekele¹⁰, C. Besliu⁹,
 B. Budick⁵, H. Bøggild⁶, C. Chasman¹, C.H. Christensen⁶,
 P. Christiansen⁶, R. Clarke⁹, R. Debbe¹, J.J. Gaardhøje⁶, K. Hagel⁷,
 H. Ito¹, A. Jipa⁹, J.I. Jordre¹¹, F. Jundt², E.B. Johnson¹⁰,
 C. Jørgensen⁶, R. Karabowicz³, E.J. Kim¹⁰, T.M. Larsen⁶, J.H. Lee⁶,
 Y.K. Lee⁴, S. Lindal¹¹, G. Løvholden², Z. Majka³, M. Murray¹⁰,
 J. Natowitz⁷, B.S. Nielsen⁶, D. Ouerdane⁶, R. Płaneta³, F. Rami²,
 C. Ristea⁶, O. Ristea⁹, D. Röhrich⁸, B.H. Samset¹¹, S.J. Sanders¹⁰,
 R.A. Sheetz¹, P. Staszczak³, T.S. Tveter¹¹, F. Videbæk¹, R. Wada⁷,
 H. Yang⁸, Z. Yin⁸, and I.S. Zgura⁹

¹*Brookhaven National Laboratory, USA*

²*IREs and Universit Louis Pasteur, Strasbourg, France*

³*Jagiellonian University, Kraków, Poland*

⁴*Johns Hopkins University, Baltimore, USA*

⁵*New York University, USA*

⁶*Niels Bohr Institute, University of Copenhagen, Denmark*

⁷*Texas A&M University, College Station, USA*

⁸*University of Bergen, Norway*

⁹*University of Bucharest, Romania*

¹⁰*University of Kansas, Lawrence, USA*

¹¹*University of Oslo, Norway*

References

REFERENCES

1. Dharmakirti (circa 7th century BC) and later Nyaya-Vaisesika school (6th century BC to the 1st century BC)
2. Leucippus (first half of 5th century BC) and his student Democritus (born around 450 BC; died in about 370 BC)
3. J.J. Thomson, *Philos. Mag.* **44**, 293 (1897).
4. J.J. Thomson, *Philos. Mag.* **7**, 237 (1904).
5. E. Rutherford, *Philos. Mag.* **21**, 669 (1911).
6. N. Bohr, *Philos. Mag.* **26**, 1 (1913).
7. M. Planck, *Verh. deutsch. Phys. Ges.* **2**, 237 (1900); *Ann. d. Phys.* **31**, 758 (1910); *Verh. deutsch. Phys. Ges.* 138 (1911); *Ann. d. Phys.* **37**, 642 (1912).
8. A. Einstein, *Ann. d. Phys.* **17**, 132 (1905); **20**, 199 (1906); **22**, 180 (1907).
9. W. Heisenberg, *ZS Phys.* **33**, 879 (1925).
10. E. Schrödinger, *Ann. Phys.* **384**, 361 (1926), *Ann. Phys.* **384**, 489 (1926), *Ann. Phys.* **384**, 734 (1926).
11. E. Rutherford, *Philos. Mag.* **37**, 581 (1919).
12. E. Rutherford, *Proc. Roy. Soc.* **A97**, 374 (1920).
13. F. Rasetti, *Proc. Nat. Acad. Sci.* **15**, 515, (1929).
14. W. Pauli, *Fünf Arbeiten zum Ausschliessungsprinzip und zum Neutrino, Texte zur Forschung Vol.27* (Wissenschaftliche Buchgesellschaft Darmstadt, 1977).
15. J. Chadwick, *PRSL* **A136**, 692 (1932).
16. H. Yukawa, *PTP* **17**, 48 (1935).
17. P.A.M. Dirac, *Proc. Roy. Soc.* **A133**, 60 (1931).
18. C.D. Anderson, *Phys. Rev.* **43**, 491 (1933).
19. C.D. Anderson and S.H. Neddermeyer, *Phys. Rev.* **50**, 263 (1936).
20. R.J. Van De Graaff, *Phys. Rev.* **38**, 1919 (1931) in: "Minutes of the Schenectady Meeting September 10, 11 and 12, 1931", *Phys. Rev.* **38**, 1915 (1931).

21. R. Wideröe, Arch. f. Elektrotech. **21**, 387 (1929).
22. D.H. Sloan and E.O. Lawrence Phys. Rev. **38**, 2021 (1931).
23. E.O. Lawrence and M.S. Livingston, Phys. Rev. **38**, 834 (1931).
24. C.M.G. Lattes, H. Muirhead, G.P.S. Occhialini, and C.F. Powell, Nature **159**, 694 (1947).
25. E. Gardner, C.M.G. Lattes, Science **107**, 270 (1948).
26. M. Gell-Mann, California Institute of Technology Synchrotron Laboratory Report No. CTSL-20, 1961 (unpublished)
27. Yuval Ne'eman, Nuclear Phys. **26**, 222 (1961).
28. M. Gell-Mann, Phys. Rev. **106**, 1296 (1957).
29. M. Gell-Mann, Phys. Rev. **125**, 1067 (1962).
30. V.E. Barnes *et al.*, Phys. Rev. Lett. **12**, 204 (1964).
31. M. Gell-Mann, Phys. Lett. **8**, 214 (1964).
32. G. Zweig, CERN reports: CERN-TH-401, CERN-TH-412 (1964).
33. B.J. Bjorken and S.L. Glashow, Phys. Lett. **11**, 255 (1964).
34. O.W. Greenberg, Phys. Rev. Lett. **13**, 598 (1964).
35. M.-Y. Han and Y. Nambu, Phys. Rev. **139**, B1006 (1965).
36. R.P. Feynman, Phys. Rev. Lett. **23**, 1415 (1969).
37. J.D. Bjorken, Phys. Rev. **179**, 1547 (1969), Phys. Rev., **185**, 1975(1969).
38. J.I. Friedman, H.W. Kendall, R.E. Taylor *et al.*, Phys. Rev. Lett. **23**, 930 (1969), Phys. Rev. Lett., **23**, 935 (1969).
39. C.N. Yang, R.L. Mills, Phys. Rev. **96**, 191 (1954).
40. D.J. Gross, F. Wilczek, Phys. Rev. Lett. **30**, 1343 (1973).
41. H.D. Politzer, Phys. Rev. Lett. **30**, 1346 (1973).
42. J.C. Collins, M.J. Perry, Phys. Rev. Lett. **34**, 1353 (1975).
43. M.M. Aggarwal *et al.* (WA98 Collaboration), Eur. Phys. J. **C23**, 225 (2002).
44. <http://aliceinfo.cern.ch/>
45. <http://atlas.ch/>
46. <http://cms.cern.ch/>
47. F. Karsch, proceedings for PANIC05, arXiv:hep-lat/0601013.
48. http://www.gsi.de/fair/experiments/CBM/index_e.html
49. <http://na49info.web.cern.ch/na49info/>

50. Physics News Update **757**, 1 (2005).
51. <http://www.bnl.gov/rhic>
52. <http://www.bnl.gov/bnlweb/facilities/TVdG.asp>
53. <http://www.bnl.gov/bnlweb/facilities/LINAC.asp>
54. <http://www.bnl.gov/bnlweb/facilities/booster.asp>
55. <http://www.bnl.gov/bnlweb/facilities/AGS.asp>
56. <http://www.star.bnl.gov/>
57. <http://www.phenix.bnl.gov/>
58. <http://www.phobos.bnl.gov/>
59. <http://www4.rcf.bnl.gov/brahms/WWW/brahms.html>
60. <http://www.rhic.bnl.gov/pp2pp/>
61. M. Adamczyk *et al.* (BRAHMS Collaboration), Nucl. Instr. Meth. **A499**, 437 (2003).
62. Z. Majka *et al.*, “Drift Chambers for the BRAHMS experiment at RHIC” (unpublished).
63. J.D. Bjorken, Phys. Rev. **179**, 1547 (1969).
64. R.P. Feynman, Phys. Rev. Lett. **23**, 1415 (1969).
65. R.P. Feynman, Photon-Hadron Interactions. Benjamin, New York (1972).
66. S. Chekanov *et al.* (ZEUS Collaboration), Phys. Rev. **D67**, 012007 (2003).
67. L. McLerran and R. Venugopalan, Phys. Rev. **D49**, 2233 (1994); **D49** 3352 (1994).
68. J.D. Bjorken, Phys. Rev. **D27**, 140 (1983).
69. I.G. Bearden *et al.* (BRAHMS Collaboration), Phys. Rev. Lett. **88**, 202301 (2002).
70. B.P. Stein, “Physics Update.”, Physics Today **48**, 9 (1995).
71. I.G. Bearden *et al.* (BRAHMS Collaboration), Phys. Rev. Lett. **93**, 102301 (2002).
72. B.B. Back *et al.* (E917 Collaboration), Phys. Rev. Lett. **86**, 1970 (2001); L. Ahle *et al.* (E802 Collaboration), Phys. Rev. **C60**, 064901 (1999); J. Barette *et al.* (E877 Collaboration), Phys. Rev. **C62**, 024901 (2000).
73. H. Appelshäuser *et al.* (NA49 Collaboration), Phys. Rev. Lett. **82**, 2471 (1999).
74. I.G. Bearden *et al.* (BRAHMS Collaboration), Phys. Rev. Lett. **90**, 102301

- (2003).
75. L. Ahle *et al.* (E866 Collaboration), Phys. Rev. Lett. **81**, 2650 (1998); Phys. Rev. **C60**, 044904 (1999).
 76. S.V. Afanasiev *et al.* (NA49 Collaboration), Phys.Rev. **C66**, 054902 (2002); M. Van Leeuwen (for NA49 Collaboration), Nucl.Phys. **A715**, 161 (2003); P. Seyboth (private communication); I.G. Bearden *et al.* (NA44 Collaboration), Phys. Rev. **C66**, 044907 (2002).
 77. P. Staszel (for BRAHMS Collaboration), proceedings for QM2005, arXiv:nucl-ex/0510061.
 78. F. Becattini *et al.*, Phys. Rev. **C64**, 024901 (2001); (private communication).
 79. P.J. Siemens and J.O. Rasmussen, Phys. Rev. Lett. **42**, 880 (1979).
 80. I. Arsene *et al.* (BRAHMS Collaboration), Phys. Rev. **C72**, 014908 (2005).
 81. I.G. Bearden *et al.* (NA44 Collaboration), Phys. Rev. Lett. **78**, 2080 (1997); M. Kaneta, Ph.D Thesis, (NA44 Collaboration), March (1999); E. Andersen *et al.* (WA97 Collaboration), Phys. Lett. **B433**, 209 (1998); C. Blume (for NA49 Collaboration), Nucl. Phys. **A698**, 104 (2002); H. Appelshäuser (for CERES Collaboration), Nucl. Phys. **A698**, 253 (2002); N. Xu and M. Kaneta, Nucl. Phys. **A698**, 306 (2002).
 82. H. Ito (for BRAHMS Collaboration), proceedings for QM2005.
 83. P. Huovinen, P.F. Kolb, U.W. Heinz, P.V. Ruuskanen and S.A. Voloshin, Phys. Lett. **B503**, 58 (2001).
 84. T. Hirano, Phys. Rev. **C65**, 011901 (2002).
 85. S.S. Adler, Phys. Rev. Lett. **91**, 182301 (2003).
 86. B.B. Back, Phys.Rev. **C72**, 051901 (2005).
 87. J. Adams, Phys. Rev. **C72**, 014904 (2005); Phys. Rev. Lett. **95**, 122301 (2005).
 88. K. Adcos *et al.* (PHENIX Collaboration), Phys. Rev. Lett. **88**, 242301 (2002); S.S. Adler *et al.* (PHENIX Collaboration), Phys. Rev. Lett. **91**, 172301 (2003).
 89. E.-J. Kim (for BRAHMS Collaboration), proceedings for QM2005, arXiv:nucl-ex/0510007.
 90. C. Adler *et al.* (STAR Collaboration), Phys. Rev. Lett. **90**, 032301 (2003); C. Adler *et al.* (STAR Collaboration), Phys. Rev. Lett. **90**, 082302 (2003); J. Adams *et al.* (STAR Collaboration), Phys. Rev. Lett. **91**, 072304 (2003); J.

- Adams *et al.* (STAR Collaboration), Phys. Rev. Lett. **93**, 252301 (2004); J. Adams *et al.* (STAR Collaboration), Phys. Rev. Lett. **95**, 152301 (2005).
91. J. Adams *et al.* (STAR Collaboration), arXiv:nucl-ex/0604018.
92. S.S. Adler *et al.* (PHENIX Collaboration), Phys. Rev. **C71**, 051902 (2005); S.S. Adler *et al.* (PHENIX Collaboration), Phys. Rev. Lett. **97**, 052301 (2006); S.S. Adler *et al.* (PHENIX Collaboration), Phys. Rev. **C73**, 054903 (2006).
93. A. Białas, M. Bleszyński and W. Czyż, Nucl. Phys. **B111**, 461 (1976).
94. B.B. Back *et al.* (PHOBOS Collaboration), arXiv:nucl-ex/0301017.
95. J.F. Owens, Rev. Mod. Phys. **59**, 465 (1987).
96. A.L.S. Angelis *et al.* (BCMOR Collaboration, CERN-ISR), Phys. Lett. **B185**, 213 (1987); M.M. Aggarwal *et al.* (WA98 Collaboration), Eur. Phys. J. **C23**, 225 (2002); J. Slivova, Ph.D Thesis (CERES Collaboration (2003); R. Albrecht *et al.* (WA80 Collaboration), Eur. Phys. J. **C5**, 255 (1998).
97. X.-N. Wang, Phys. Rev. **C61**, 064910 (2000); E. Wang, X.-N. Wang, Phys. Rev. **C64**, 034901 (2001).
98. J.W. Cronin *et al.*, Phys. Rev. **D11**, 3105 (1975); D. Antreasyan *et al.*, Phys. Rev. **D19**, 764 (1979).
99. C. Adler *et al.* (STAR Collaboration), Phys. Rev. Lett. **89**, 202301 (2002).
100. K. Adcox *et al.* (PHENIX Collaboration), Phys. Lett. **B561**, 82 (2003).
101. C.E. Jørgensen (for BRAHMS Collaboration), Nucl. Phys. **A715**, 741 (2003).
102. C. Albajar *et al.* (UA1 Collaboration), Nucl. Phys. **B335** 261 (1990).
103. S.S. Adler *et al.* (PHENIX Collaboration), Phys. Rev. Lett. **94**, 232301 (2005).
104. S.S. Adler *et al.* (PHENIX Collaboration), Phys. Rev. Lett. **96**, 202301 (2006).
105. T.M. Larsen (for BRAHMS Collaboration), proceedings for QM2005.
106. B. Alper *et al.*, Nucl. Phys. **B100**, 237 (1975).
107. H. Buesching (for PHENIX Collaboration), J.Phys. **G31**, 473 (2005); J. Dunlop (for STAR Collaboration), Plenary talk at the RHIC & AGS Annual Users Meeting, May 10-14, 2004, in: J.L. Klay, J.Phys. **G31**, 451 (2005).
108. S.S. Adler *et al.* (PHENIX Collaboration), Phys. Rev. **C69**, 034910 (2004); M. Shumomura (for PHENIX Collaboration), proceedings for QM2005, arXiv:nucl-ex/0510023.
109. I. Arsene *et al.* (BRAHMS Collaboration), Phys. Rev. Lett. **91**, 072305 (2003).

110. Camelia Mironov (for STAR Collaboration), *J. Phys.* **G31**, 1195 (2005).
111. I. Arsene *et al.* (BRAHMS Collaboration), *Phys. Rev. Lett.* **93**, 242303 (2004).
112. D. Kharzeev, Y. V. Kovchegov and K. Tuchin, *Phys. Lett.* **B599**, 23 (2004).
113. A. Capella *et al.*, *Eur. Phys. J.* **C40**, 129 (2005).
114. V.N. Gribov and L.N. Lipatov. *Sov. J. Nucl. Phys.* **15**, 438 (1972); Yu.L. Dokshitzer. *Sov. Phys. JETP* **46**, 641(1977); G. Altarelli and G. Parisi. *Nucl. Phys.* **B126**, 298 (1977).
115. J.D. Bjorken, FERMILAB-PUB-82-059-THY.
116. M. Gyulassy and M. Plümer, *Phys. Lett.* **B243**, 432 (1990); M. Gyulassy, M. Plümer, M. H. Thoma, and X.-N. Wang, *Nucl. Phys.* A538, 37 (1992); X.-N. Wang and M. Gyulassy, *Phys. Rev. Lett.* **68**, 1480 (1992); M. Gyulassy, X.-N. Wang, *Nucl. Phys.* **B420**, 583 (1994).
117. M. Gyulassy, P. Levai and I. Vitev, *Phys. Rev. Lett.* **85**, 5535 (2000); M. Gyulassy, P. Levai and I. Vitev, *Nucl. Phys.* **B594**, 371 (2001); I. Vitev, M. Gyulassy, *Phys. Rev. Lett.* **89**, 252301 (2002); M. Gyulassy, I. Vitev, X.-N. Wang, B.-W. Zhang, *nucl-th/0302077* (2003).
118. L.D. Landau and I.Ya. Pomeranchuk, *Dokl. Akad. Nauk SSSR* **92**, 535 (1953); L.D. Landau and I.Ya. Pomeranchuk, *Dokl. Akad. Nauk SSSR* **92**, 735 (1953); A.B. Migdal, *Phys. Rev.* **103**, 1811 (1956); E.L. Feinberg and I.Ya Pomeranchuk, *Suppl. Nuovo Cimento* **3**, 652 (1956); E.L. Feinberg and I.Ya Pomeranchuk, *Sov. Phys. Usp.* **30**, 132 (1966); X.-N. Wang, M. Gyulassy and M. Plümer, *Phys. Rev.* **D51**, 3436 (1995).
119. X. F. Guo and X.-N. Wang, *Phys. Rev. Lett.* **85**, 3591 (2000); X.-N. Wang and X. F. Guo, *Nucl. Phys.* **A696**, 788 (2001); J. Osborne, X.-N. Wang, *Nucl. Phys.* **A710**, 281 (2002); B.-W. Zhang, X.-N. Wang, *Nucl. Phys.* **A720**, 429 (2003).
120. E. Wang, X.-N. Wang, *Phys. Rev. Lett.* **89**, 162301 (2002).
121. X.-N. Wang, *Phys. Lett.* **B595**, 165 (2004);
122. X.-N. Wang, proceedings for QM2005, arXiv:nucl-th/0511001.
123. A. Dainese, C. Loizides and G. Paic, *Eur. Phys. J.* **C38**, 461 (2005); A. Dainese, C. Loizides and G. Paic, proceedings for QM2005, arXiv:hep-ph/0511045.
124. R. Baier, Yu. L. Dokshitzer, A.H. Mueller, S. Peigné and D. Schiff, *Nucl. Phys.* **B483**, 291 (1997); R. Baier, Yu. L. Dokshitzer, A.H. Mueller, S. Peigné and D.

- Schiff, Nucl. Phys. **B484**, 265 (1997); R. Baier, Yu. L. Dokshitzer, A.H. Mueller and D. Schiff, Nucl. Phys. **B531**, 403 (1998); R. Baier, Yu. L. Dokshitzer, A.H. Mueller and D. Schiff, Phys. Rev. **C60**, 064902 (1999).
125. B.G. Zakharov, JETP Lett. **63**, 952 (1996); B.G. Zakharov, JETP Lett. **65**, 615 (1997); B.G. Zakharov, JETP Lett. **73**, 49 (2001); B.G. Zakharov, JETP Lett. **76**, 201 (2002).
126. U.A. Wiedemann, Nucl. Phys. **B582**, 409 (2000); U.A. Wiedemann, Nucl. Phys. **B588**, 303 (2000); U.A. Wiedemann, Nucl. Phys. **A690**, 731 (2001); C.A. Salgado and U.A. Wiedemann, Phys. Rev. Lett. **89**, 092303 (2002).
- 127., K.J. Eskola, V.J. Kolhinen and P.V. Ruuskanen, Nucl. Phys. **B535**, 351 (1998); K.J. Eskola, V.J. Kolhinen and C.A. Salgado, Eur. Phys. J. **C9**, 61 (1999). K.J. Eskola, K. Kajantie, P.V. Ruuskanen and K. Tuominen, Nucl. Phys. **B570**, 379 (2000); K.J. Eskola and H. Honkanen, Nucl. Phys. **A713**, 167 (2003); K.J. Eskola, H. Honkanen, C.A. Salgado and U.A. Wiedemann, Nucl. Phys. **A747**, 511 (2005); K.J. Eskola, H. Niemi, P.V. Ruuskanen and S.S. Räsänen, Phys. Lett. **B566**, 187 (2003); K.J. Eskola, H. Honkanen, H. Niemi, P.V. Ruuskanen, S.S. Räsänen, proceedings for QM2005, arXiv:hep-ph/0510019.
128. T. Hirano and Y. Nara, Phys. Rev. **C66**, 041901 (2002); T. Hirano and Y. Nara, Phys. Rev. Lett. **91**, 082301 (2003); T. Hirano and Y. Nara, Nucl. Phys. **A721**, 277 (2003); T. Hirano and Y. Nara, Phys. Rev. **C69**, 034908 (2004).
129. T. Hirano and Y. Nara, Phys. Rev. **C68**, 064902 (2003).
130. T. Sjöstrand, P. Eden, C. Friberg, L. Lönnblad, G. Miu, S. Mrenna, and E. Norrbin, Comput. Phys. Commun. **135**, 238 (2001).
131. K.P. Das and R.C. Hwa, Phys. Lett. **B68**, 459 (1977); R.C. Hwa, Phys. Rev. **D22**, 1593 (1980); R. C. Hwa and C. B. Yang, Phys. Rev. **C65**, 034905 (2002), Phys. Rev. **C66**, 025204 (2002); Phys. Rev. **C66**, 025205 (2002); R. C. Hwa, C. B. Yang and R. J. Fries, Phys. Rev. **C71**, 024902 (2005); R. C. Hwa and C. B. Yang, Phys. Rev. **C73**, 044913 (2006).
132. I. Vitev, M. Gyulassy and P. Levai, arXiv:hep-ph/0109198; I. Vitev and M. Gyulassy, Phys. Rev. **C65**, 041902 (2002); I. Vitev and M. Gyulassy, Nucl. Phys. **A715**, 779 (2003).
133. G.C. Rossi and G. Veneziano, Nucl. Phys. **B123**, 507 (1977); L. Montanet, G.C.

- Rossi and G. Veneziano, Phys. Rept. **63**, 149 (1980); D. Kharzeev, Phys. Lett. **B378**, 238 (1996); S.E. Vance, M. Gyulassy and X.-N. Wang, Phys. Lett. **B442**, 45 (1998); S.E. Vance and M. Gyulassy, Phys. Rev. Lett. **83**, 1735 (1999).
- 134.Y.K. Lee, R. Debbe, J.H. Lee, H. Ito and S.J. Sanders, Nucl. Instr. Meth. **A516**, 281 (2004).
- 135.J.I. Jørdre, Master Thesis, University of Bergen.
- 136.DC studies - BRAHMS Analysis Notes 27, 29, 34 and 38.
- 137.R. Karabowicz, Master Thesis, Jagiellonian University.
- 138.P.H.L. Christiansen Ph.D. Dissertation, University of Copenhagen.
- 139.P.A. Cerenkov, Dokl. Akad. Nauk SSSR **2**, 451 (1934). I.E. Tamm and I.M. Frank, Dokl. Akad. Nauk SSSR **14**, 107 (1937).
- 140.<http://wwwasd.web.cern.ch/wwwasd/>.
- 141.R.J. Glauber, Phys. Rev. **100**, 242 (1955); C.Y. Wong and Z.D. Lu, Phys. Rev. **D39**, 2606 (1989).
- 142.D. Kharzeev and M. Nardi, Phys. Lett. **B507**, 121 (2001); C.-Y. Wong, "Introduction to High-Energy Heavy-Ion Collisions" (World Scientific, Singapore, 1994); A.J. Baltz, C. Chasman and S.N. White, Nucl. Instr. Meth. **A417**, 1 (1998); F. Antinori *et al.* (WA97 Collaboration), Nucl. Phys. **A661**, 357 (1999).
- 143.K. Adcox *et al.* (PHENIX Collaboration), Phys. Rev. Lett. **88**, 022301 (2002); J. Adams *et al.* (STAR Collaboration), arXiv:nucl-ex/0311017 (2003); B.B. Back *et al.* (PHOBOS Collaboration), Phys. Rev. **C70**, 021902 (2004).
- 144.S.S. Adler *et al.* (PHENIX Collaboration), Phys. Rev. Lett. **91**, 072301 (2003).
- 145.L.V. Gribov, E.M. Levin, M.G. Ryskin, Phys. Rep. **100**, 1 (1983); D. Kharzeev, E.M. Levin, L. McLerran, Phys. Lett. **B561**, 93 (2003).
- 146.R. Karabowicz (for BRAHMS Collaboration), proceedings for QM05, arXiv:nucl-ex/0510038.